

Modelling and Analysis of Atrial Epicardial Electrograms
An approach based on graph signal processing and confirmatory factor analysis

Sun, M.

Publication date

2022

Document Version

Final published version

Citation (APA)

Sun, M. (2022). *Modelling and Analysis of Atrial Epicardial Electrograms: An approach based on graph signal processing and confirmatory factor analysis*. [Dissertation (TU Delft), Delft University of Technology].

Important note

To cite this publication, please use the final published version (if applicable).
Please check the document version above.

Copyright

Other than for strictly personal use, it is not permitted to download, forward or distribute the text or part of it, without the consent of the author(s) and/or copyright holder(s), unless the work is under an open content license such as Creative Commons.

Takedown policy

Please contact us and provide details if you believe this document breaches copyrights.
We will remove access to the work immediately and investigate your claim.

MODELLING AND ANALYSIS OF ATRIAL EPICARDIAL ELECTROGRAMS

**AN APPROACH BASED ON GRAPH SIGNAL PROCESSING AND
CONFIRMATORY FACTOR ANALYSIS**

MODELLING AND ANALYSIS OF ATRIAL EPICARDIAL ELECTROGRAMS

**AN APPROACH BASED ON GRAPH SIGNAL PROCESSING AND
CONFIRMATORY FACTOR ANALYSIS**

Proefschrift

ter verkrijging van de graad van doctor
aan de Technische Universiteit Delft,
op gezag van de Rector Magnificus prof. dr. ir. T.H.J.J. van der Hagen,
voorzitter van het College voor Promoties,
in het openbaar te verdedigen op woensdag 15 juni 2022 om 15:00 uur

door

Miao SUN

Master of Natural Science in Computer Applied Technology,
Peking University, Beijing, China,
geboren te Guangdong, China.

Dit proefschrift is goedgekeurd door de promotoren.

Samenstelling promotiecommissie bestaat uit:

Rector Magnificus,	voorzitter
Dr. ir. R. C. Hendriks,	Technische Universiteit Delft, promotor
Prof. dr. ir. A. J. van der Veen,	Technische Universiteit Delft, promotor
Prof. dr. N. M. S. de Groot,	Erasmus University Medical Center, Technische Universiteit Delft, promotor

Onafhankelijke leden:

Prof. dr. ir. W.A. Serdijn	Technische Universiteit Delft
Prof. dr. ir. G.J.T. Leus,	Technische Universiteit Delft
Prof. dr. L.R.C. Dekker,	Technische Universiteit Eindhoven, Catharina Ziekenhuis Eindhoven
Prof. dr. ir. L. De Lathauwer,	Katholieke Universiteit Leuven, België
Dr. ir. R.F. Remis,	Technische Universiteit Delft, reservelid



Keywords: Atrial fibrillation, epicardial electrograms, spectral analysis, graph-time signal processing, electrophysiological model, cross-power spectral density matrix model, conductivity estimation, activation time estimation, anisotropy ratio estimation, confirmatory factor analysis.

Acknowledgement: This research was financially supported by the Guangzhou Elites Scholarship Council.

Copyright © 2022 by M. Sun

ISBN 978-94-6366-545-2

An electronic version of this dissertation is available at
<http://repository.tudelft.nl/>.

To my family

CONTENTS

Summary	xi
Samenvatting	xiii
1 Introduction	1
1.1 Research Motivation	1
1.2 Research Objectives	4
1.3 Outline of the Thesis	5
1.3.1 Chapter 2: Cardiology Fundamentals and Research Background	5
1.3.2 Chapter 3: Graph-Time Spectral Analysis on EGM	6
1.3.3 Chapter 4: Cardiac Tissue Conductivity Estimation Using Confirmatory Factor Analysis	6
1.3.4 Chapter 5: Joint Estimation of EGM Model Parameters Using Confirmatory Factor Analysis	7
1.3.5 Chapter 6: Conclusions and Future Work	7
1.4 List of Publications	7
References	8
2 Cardiology Fundamentals and Research Background	11
2.1 Anatomy and Physiology of Human Heart	11
2.1.1 Anatomy of human heart	11
2.1.2 The electrical conduction system of the heart	12
2.2 Electrical Activity of the Heart	13
2.2.1 Cardiac cell membrane action potential	13
2.2.2 Action potential propagation	15
2.2.3 Cardiac arrhythmia - abnormal action potential generation	15
2.3 Atrial Fibrillation	16
2.3.1 What is atrial fibrillation?	16
2.3.2 Mechanisms underlying AF	16
2.3.3 Classification of AF	17
2.3.4 Treatment of AF	18
2.4 Measuring the Cardiac Electrical Activity	18
2.4.1 Atrial mapping approach	18
2.4.2 ECG vs. EGM	20
2.5 Preprocessing and Analysis of the EGMs	21
2.5.1 Preprocessing	21
2.5.2 Spectral analysis and cardiac arrhythmia	22
2.5.3 Spectral analysis using graph signal processing	22

2.6	Mathematical Models of EGMs	25
2.6.1	Bidomain/Monodomain model of action potential propagation	26
2.6.2	Electrogram model.	31
2.6.3	Impulse response model.	32
2.6.4	Parameters and estimation.	33
2.6.5	Estimating parameters using confirmatory factor analysis	34
	References	35
3	Graph-Time Spectral Analysis for Atrial Fibrillation	41
3.1	Introduction	41
3.2	Database	44
3.3	Theory	45
3.3.1	Graph signal processing	45
3.3.2	Joint STFT and GFT	47
3.4	Graph-time Spectral Analysis	48
3.4.1	STFT analysis & GFT analysis	48
3.4.2	Joint STFT and GFT analysis	49
3.5	Graph-Based Atrial Activity Extraction	51
3.6	Evaluation of Atrial Activity Extraction	52
3.6.1	Synthetic data generation	52
3.6.2	Performance metrics.	54
3.6.3	Results.	55
3.6.4	Computational complexity & Implementation	56
3.7	Conclusions.	58
	References	58
4	Cardiac Tissue Conductivity Estimation Using Confirmatory Factor Analysis	63
4.1	Introduction	64
4.2	Electrogram Model	65
4.2.1	Notation	65
4.2.2	Electrical propagation & Electrogram model.	66
4.2.3	Impulse response model.	68
4.2.4	CPSDM model	69
4.2.5	Problem formulation.	71
4.3	Confirmatory Factor Analysis	71
4.3.1	The general CFA problem	71
4.3.2	CFA problem for conductivity estimation	73
4.3.3	Simultaneous CFA in multiple frequencies.	74
4.3.4	Practical considerations	75
4.4	Numerical Experiments on the Simulated Data	77
4.4.1	Data generation	77
4.4.2	Model testing	78
4.4.3	Evaluation	79
4.5	Experiments on Clinical Data	86
4.6	Conclusions and Discussions	87
	References	89

5	Joint Cardiac Tissue Conductivity and Activation Time Estimation Using Confirmatory Factor Analysis	93
5.1	Introduction	94
5.2	Preliminaries	95
5.2.1	Electrogram models	95
5.2.2	Problem formulation.	96
5.3	Simultaneous Confirmatory Factor Analysis for Joint Estimation of Tissue Properties.	97
5.3.1	Simultaneous CFA problem for joint estimation in multiple frequencies and multiple heart beats.	97
5.3.2	Identifiability conditions of the SCFA problem.	98
5.3.3	Practical consideration.	99
5.4	Experiments on Simulated Data	100
5.4.1	Generation of simulated data	100
5.4.2	Evaluation	102
5.5	Experiments on Clinical Data	107
5.6	Conclusions and Discussions	113
	References	114
6	Conclusions and Future Work	117
6.1	Concluding Remarks	117
6.1.1	Graph signal processing for AF studying	117
6.1.2	Electrophysiological EGM models and parameter estimation	119
6.2	Future Research Questions	121
6.2.1	Graph signal processing for AF research	121
6.2.2	Electrophysiological models of cardiac tissue and model parameter estimation	122
	References	124
	Acknowledgements	127
	Curriculum Vitae	129

SUMMARY

Atrial fibrillation (AF) is a frequently encountered cardiac arrhythmia characterized by rapid and irregular atrial activity, which increases the risk of strokes, heart failure and other heart-related complications. The mechanisms of AF are complicated. Although various mechanisms were proposed in previous research, the precise mechanisms of AF are not clear yet and the optimal therapy for AF patients are still under debated. A higher success rate of AF treatments requires a deeper understanding of the problem of AF and potentially a better screening of the patients.

In order to study AF, instead of using human body surface ECGs, we use the epicardial electrograms (EGMs) obtained directly from the epicardial sites of the human atria during open heart surgery. This data is measured using a high-resolution mapping array and exhibits irregular properties during AF. Although different studies have analyzed electrograms in time and frequency domain, there remain many open questions that require alternative and novel tools to investigate AF.

Experience in signal processing suggests that incorporating the spatial dimension into the time-frequency analysis on the multi-electrode electrograms may provide improved insights on the atrial activity. However, the electrophysiological models for describing spatial propagation are relatively complex and non-linear such that conventional signal processing methods are less suitable for a joint space, time, and frequency domain analysis. It is also difficult to use very detailed electrophysiological models to extract tissue parameters related to AF from the high-dimensional data.

In this dissertation, we wish to propose a radically different approach to study and analyze the EGMs from a higher abstraction level and from different perspectives to get more understanding of the characteristics of AF. We also aim to develop a simplified electrophysiological model that can capture the spatial structure of the data and propose an efficient method to estimate the tissue parameters, which are helpful to analyze the electropathology of the tissue, e.g., cell activation time or conductivity.

In the first part of this study, we put forward a graph-time spectral analysis framework to analyze EGMs during normal heart rhythm and AF with a higher-level model. To capture the frequency content along both time domain and graph domain, we propose the joint graph and short-time Fourier transform, which allows us to evaluate the temporal and spatial variation of EGMs and capture the interaction between space and time. The spectral analysis of the EGMs helps us to recognize atrial fibrillation impact on the atrial activity and identify the differences between the atrial activity and the ventricular activity. We find that the difference in graph smoothness between the atrial and ventricular activities enables us to better extract the atrial activity from the noisy measurements.

The second part of this study is to find a simplified but accurate enough electrophysiological model for the high dimensional EGMs and to make more efficient use of the data to detect the arrhythmogenic substrate that causes abnormalities in atrial tissue. In this

dissertation, we develop the cross power spectral density matrix (CPSDM) model of the multi-electrode EGMs and make use of an effective method called confirmatory factor analysis (CFA) to jointly estimate the model parameters. The conductivity, the activation time, and the anisotropy ratio are useful parameters to determine abnormalities in cardiac tissue and are therefore the target parameters to be estimated. With the reasonable assumptions that the conductivity parameters and the anisotropy parameters are constant across different frequencies and heart beats, and the activation time of cells are constant across different frequencies, we propose simultaneous CFA (SCFA) to jointly estimate these parameters using multiple frequencies and multiple heart beats. The identifiability conditions which need to be satisfied in the CFA problem are used to find the relationship between the desired resolution and the required amount of data. Evaluations on the simulated data and the clinical data demonstrate that the proposed method can localize the conduction blocks in the tissue and reconstruct the clinical EGMs well using the estimated parameters.

SAMENVATTING

Boezemfibrilleren is een vaak voorkomende hartritmestoornis die wordt gekenmerkt door snel en onregelmatig samentrekken van de boezems. Het vergroot de kans op beroertes, hartfalen en andere hart gerelateerde complicaties. De achterliggende mechanismes die boezemfibrilleren veroorzaken zijn gecompliceerd en ondanks verschillende theorieën is de exacte oorzaak en daarmee de beste therapie nog steeds onbekend. Om de slagingskans van de behandeling van boezemfibrillatie te vergroten is meer kennis van het achterliggende probleem en een betere screening van patiënten noodzakelijk.

Om boezemfibrilleren te bestuderen kunnen we epicardiale elektrogrammen gebruiken, welke direct gemeten worden op het epicardium tijdens een openhartoperatie, in plaats van elektrogrammen welke gemeten worden op het lichaamsoppervlak. De elektrogrammen worden gemeten met een hoge resolutie elektrode array tijdens zowel normaal sinusritme als gedurende boezemfibrillatie. Hoewel er al verschillende studies naar de tijd en frequentie eigenschappen van elektrogrammen zijn gedaan, zijn er nog steeds veel onduidelijkheden waardoor alternatieve technieken nodig zijn om boezemfibrilleren te bestuderen.

Verbeterde inzichten zouden verkregen kunnen worden door de spatiële dimensie van de elektrode array mee te nemen in de tijd-frequentie analyse. Echter, elektrofysiologische modellen om de spatiële propagatie van atriale signalen te beschrijven zijn complex en niet-lineair, waardoor conventionele signaalverwerkingstechnieken minder geschikt zijn voor de gezamenlijke spatiële, tijd en frequentie analyse. Ook zijn de elektrofysiologische modellen dermate complex en gedetailleerd, dat dit het schatten van modelparameters welke het onderliggende weefsel beschrijven bemoeilijkt.

In dit proefschrift willen we een radicaal andere benadering voorstellen, waarmee we de elektrogrammen bestuderen en analyseren vanuit een hoger abstractieniveau om zodoende meer inzicht te krijgen in de kenmerken van boezemfibrilleren. Daarnaast willen we een vereenvoudigd elektrofysiologisch model ontwikkelen waarmee de onderliggende weefselparameters, zoals de activatietijd van de cel en de cel-geleiding, geschat kunnen worden.

In het eerste deel van dit proefschrift stellen we een methode voor om de spatiële aspecten te modeleren met zogenaamde grafen. Hiermee zijn we in staat om de gecombineerde spatiële, tijd en frequentie eigenschappen van elektrogrammen tijdens zowel normaal hartritme en boezemfibrillatie op een hoger abstractieniveau te bestuderen. Om de spectrale analyse in zowel het tijdsdomein als het graaf-domein vast te leggen, stellen we een graaf Fouriertransformatie voor waarbij eerst per tijdsframe een conventionele Fouriertransformatie wordt toegepast, gevolgd door een graaf Fouriertransformatie. Hiermee kunnen zowel de temporele, de spatiële en spectrale eigenschappen van de elektrogrammen bestudeerd worden, evenals de interactie tussen het temporele en het spatiële domein.

Het tweede deel van deze studie richt zich op de ontwikkeling van een vereenvoudigd, maar nauwkeurig genoeg elektrofysiologisch model om op basis van de gemeten elektrogrammen de afwijkingen in het aritmogene substraat te detecteren. Hierbij wordt gebruik gemaakt van geschatte spatiële correlatie matrices per frequentieband, in combinatie met confirmatory factor analysis (CFA) om de onderliggende modelparameters van het weefsel te schatten. Deze modelparameters bestaan onder andere uit de elektrische celgeleiding, de activeringstijd van de cellen, en de anisotropie en kunnen uiteindelijk gebruikt worden om afwijkingen in het hartweefsel vast te stellen. Op basis van de redelijke aannames dat de elektrische geleiding en de anisotropie constant zijn over verschillende frequenties en hartslagen, en de activeringstijd van cellen constant is over frequentie, stellen we simultane CFA (SCFA) voor om deze parameters gezamenlijk te schatten met behulp van meerdere frequenties en meerdere hartslagen. De voorwaarden waaraan het CFA-probleem moet worden voldaan, worden gebruikt om de relatie te vinden tussen de gewenste resolutie en de benodigde hoeveelheid data. Evaluaties van de gesimuleerde gegevens en de klinische gegevens tonen aan dat de voorgestelde methode gebruikt kan worden om de blokkade van de elektrische geleiding in het weefsel te lokaliseren. Daarnaast kunnen op basis van de geschatte parameters de oorspronkelijke klinische elektrogrammen goed gereconstrueerd worden, waarmee de effectiviteit van het algoritme gevalideerd is.

1

INTRODUCTION

CARDIOVASCULAR diseases are the leading cause of death globally [1]. They are often complicated by the development of cardiac arrhythmias. Some arrhythmias are life threatening (e.g., ventricular fibrillation), while others like atrial fibrillation (AF) lead to serious complications. Among the different arrhythmias, AF is most common sustained arrhythmia. However, the mechanisms underlying AF are not yet fully understood and need to be further investigated to improve the treatment of AF. With the development of high resolution electrode mapping techniques, it is possible to measure the transmembrane potentials of the atrial tissue during open heart surgery at multiple locations in a parallel manner. With these high-resolution measurements, we wish to gain a deeper understanding on the characteristics of AF and the underlying structure of the diseased tissue using advanced signal processing techniques.

1.1. RESEARCH MOTIVATION

AF is the most common type of cardiac arrhythmia and frequently encountered in daily clinical practice. It is characterized by rapid and irregular beating of the atria. On average, about 1% - 2% of the population suffers from AF [2]. In Europe, over six million people suffer from this disease and the prevalence is predicted to at least double in the next 50 years [2]. AF is more common in older people. Approximately 1% of the patients with AF is below the age of 60 years, while up to 12% of the patients with AF is aged from 75 to 84 years and more than one third of the patients are older than 80 years [3]. Previous research showed that AF can lead to a 5-fold increased risk of stroke and the risk increases with age [4]. AF is also associated with a doubling of the risk to develop dementia [5] and an increase of mortality [4].

Patients with AF generally have significantly higher health care costs. Hence, the healthcare costs per year (estimated from 2004 to 2006) of a patient suffering from AF are about €7400 higher compared to a patient without AF [3]. However, the mechanisms of AF are complicated and not yet well understood. Good treatment strategies for AF patients are also still unknown. Pharmacological therapy is currently the preferred measure to control the disease at its early stage, but it is often followed by strong side effects

like an increased probability of heart failure, bradycardia or heart block [3]. The currently most accepted and effective treatment strategy for AF is radiofrequency catheter ablation, which is achieved by burning some small areas in the atrial tissue that cause rapid and irregular heart beats. Due to the lack of understanding of AF, it is hard to accurately point out the abnormal tissue areas that need to be ablated. For better efficacy and safety of the treatment, it is important to get a deeper understanding of AF.

One way to study the electrical behaviour of the heart is by means of the surface electrocardiogram (ECG). However, the conventional surface ECG is not so informative for studying AF, since the atrial signal is rather weak in the surface ECGs and gets easily corrupted by noise. Moreover, the spatial resolution is rather poor. To obtain a better understanding of atrial fibrillation, we use in this research epicardial electrograms (EGMs) obtained by measuring the electric activity directly on the heart, instead of surface ECGs measured from the outside of the human body. The data that we use are measured during normal sinus rhythm (SR) and AF using an intra-operative and high-resolution atrial mapping technique introduced in [6]. This technique uses a high-resolution mapping array equipped with many electrodes to record the transmembrane potentials at multiple locations of the epicardial sites of the atria in a parallel manner. With this high spatial-temporal resolution data, we can investigate the propagation of the electrical activity across the cardiac tissue to determine the characteristics of the wave propagation in the heart and identify the diseased areas in the atria.

To analyze the wave propagation pattern, first we need a proper computational model of the EGM data to describe the propagation of the electrical activity across the tissue. Physical models have been proposed to describe the propagation of the action potential in cardiac tissue [7–9]. These models contain many parameters related to tissue properties. When it comes to high-dimensional data, these models are rather complicated to use in combination with inversion techniques to estimate the underlying tissue parameters. Although deeper understanding can be achieved by incorporating the spatial dimension, it is difficult to use conventional signal processing approaches to analyze data in the joint space, time, and frequency domain based on such complicated models. It becomes even more challenging when analyzing the highly irregular electrical activity during AF with these non-linear models. In addition, estimating the parameters from these models by solving an inverse problem involves considerable computational difficulties. It is therefore important to find a proper model with lower complexity to efficiently study the high-resolution and irregular EGM data and extract useful information from the underlying tissue. In this thesis, we therefore study the use of graph signal processing and simplified electrophysiological models in combination with factor analysis to extract information on the underlying tissue.

Graphs are natural tools to model data living in high-dimensional and irregular domains [11] and graph signal processing (GSP) techniques that deal with signals residing on the graph vertices have raised more and more attention in recent years. A graph is a set of nodes which are interconnected by a set of edges. In a graph model, each data element corresponds to a node and a nonzero edge weight reflects the appropriate dependency or similarity relation between the data elements connected by the edge. Figure 1.1 illustrates a graph example that models the temperature measurements of the Island of Brehat. The temperature measurements indexed by the nodes forms a graph

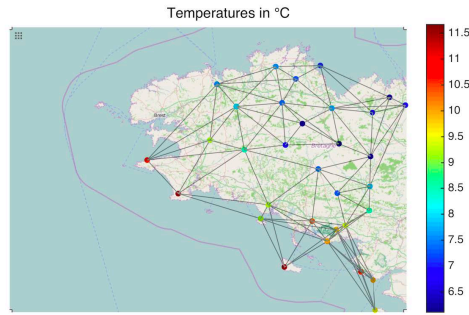


Figure 1.1: A graph example that models the temperature measurements of the Island of Brehat. The graph is built from the coordinates of the weather stations by connecting all the neighbours in a given radius [10]. The nodes represent the weather stations and the edges represent their neighborhood connections. The colored dots indicate the temperature values, which are known as the graph signal values in GSP.

signal. GSP has recently been applied to brain signal analysis, Alzheimer classification, and body motion analysis [12–19]. However, despite showing promise, graph signal processing is still unexplored for heart-related problems. The propagation of the electrical activity in atrial tissue is highly irregular during AF. Considering the high spatial dimension and high irregularity properties of the EGM data used in this study, we aim to propose a graph-based high-level model for the complicated atrial activity during AF and explore a novel approach based on graph signal processing techniques to analyze the EGMs; hence, taking a step further towards exploring AF.

Modelling the EGMs based on the electrophysiology of the heart is important to study the electropathology of diseased tissue. Generally, detailed models are required that involve parameters directly connected to tissue properties. Some of these parameters, such as the electrical conductivity or the activation time of cells, are useful parameters that can indicate the local damage of the atrial tissue, which probably contributes to the development and progression of AF [6, 20]. In this study, we are also interested in estimating such parameters. To make efficient use of the high-resolution data, a simpler but accurate enough forward model that can capture the spatial relation of the multi-electrode data is required in this study. To estimate the parameters from the electrophysiological model, we need to deal with an ill-posed inverse problem. Since there are many parameters in electrophysiological models, solving the problem is computationally challenging, especially when high-resolution data is taken into account. It is therefore important to propose an efficient algorithm that can jointly estimate the parameters from the electrophysiological model in this study. Factor analysis is a useful tool to test whether the data fits a hypothesized measurement model that captures the correlation of the measurements. It was first introduced by Spearman in 1904 to find a quantitative measure for intelligence [21] and later was developed as a multivariate technique [22–25]. Factor analysis has also been applied to array signal processing in radio astronomy research in the case where the noise powers are unknown and different for each element in the array [26, 27]. More recently, confirmatory factor analysis has been applied to efficiently estimate a set of parameters from the multi-microphone signal model

[28], which further inspires us to explore this technique for estimating the parameters of interest from the electrophysiological model.

1.2. RESEARCH OBJECTIVES

The accurate mechanisms of AF are still unclear and the debate on the best treatment for AF patients is ongoing. The general goal of this study is to get a better understanding of AF by modelling and analyzing the electrical activity propagation in cardiac tissue using advanced signal processing techniques.

An electrogram is measured at a specific position. We can analyze its temporal characteristics or analyze its spectral properties. With electrograms measured at different positions, we can further analyze the spatial characteristics of the electrograms. In this research, with the high-resolution EGMs obtained from AF and non-AF patients, we would like to characterize the differences of the EGMs in AF and non-AF from the temporal, spatial, and spectral aspects, and explore the relation between them. Since the conventional physical model of electrograms is rather complex, we first aim to propose a novel graph-based approach to study and analyze the EGM data from a higher abstraction level and from different perspectives to get more understanding of the characteristics of AF. To the best of our knowledge, graph signal processing has not been applied to analyze EGM data. There are many open questions to use this new technique to study AF. As a preliminary study on AF using graph signal processing, we focus on the following research questions:

Q1. Can we make use of graph signal processing tools to model the EGM data at a higher abstraction level and analyze the EGMs in the joint space, time, and frequency domain to identify the characteristics of AF? This leads to the following three more specific questions:

Q1.1. Since a good and representative graph structure will be important to the spectral analysis of graphs signals, how can we construct a graph to model the EGM data?

Q1.2. Can we use graph-time signal processing to analyze time-varying EGMs to find differences between normal sinus rhythm (SR) and atrial fibrillation (AF) in the joint space, time, and frequency domain?

Q1.3. Since EGMs consist of both atrial and ventricular components and for this study the atrial components are of interest, can we propose a graph-time signal processing technique to analyze the spectral differences between atrial activity and ventricular activity? If yes, can we further separate the two activities based on the findings to obtain more reliable atrial EGMs for AF research?

To get a better understanding of AF, we are in need of methods that can estimate parameters that describe the underlying tissue in terms of electrophysiology. As most electrophysiological models are rather complex to be used for inversion, we also look for a simplified electrophysiological model of electrograms to extract tissue parameters, which are related to the development and progression of AF. In this study we wish to propose an algorithm that can make efficient use of the data to estimate the parameters of interest. To achieve this objective, we propose the following research questions:

Q2. Can we use a simplified, but accurate electrophysiological model for the high dimensional EGM data and make more efficient use of the data to estimate tissue parameters to identify abnormalities in the tissue? This research question has led to the

following three more specific questions as:

Q2.1. Can we develop a simplified, but accurate electrophysiological model which can capture the spatial-temporal information of EGM data?

Q2.2. How can we efficiently estimate tissue parameters using multiple frequencies and multiple heart beats in SR or AF?

Q2.3. Given the spatial resolution of the measurements, can we determine the maximum resolution for which we can reliably estimate the parameters?

Note that the answers to these questions will not directly lead to a better understanding of AF, but will help to take a step further towards our goal of using advanced signal processing techniques to study AF.

1.3. OUTLINE OF THE THESIS

This dissertation is organized into four main parts, consisting of six chapters in total, as shown in Figure 1.2. The remainder of Part I consists of Chapter 2, in which the necessary background knowledge of this dissertation will be introduced. In Part II we review the basic concepts of graph signal processing (GSP) and introduce the graph-time spectral analysis techniques for modelling and analyzing the EGMs in SR and AF. In Part III we focus on electrophysiological modelling and parameter estimation using simultaneous confirmatory factor analysis (SCFA). In Part IV, we give an overview of each chapter and summarize the contributions.

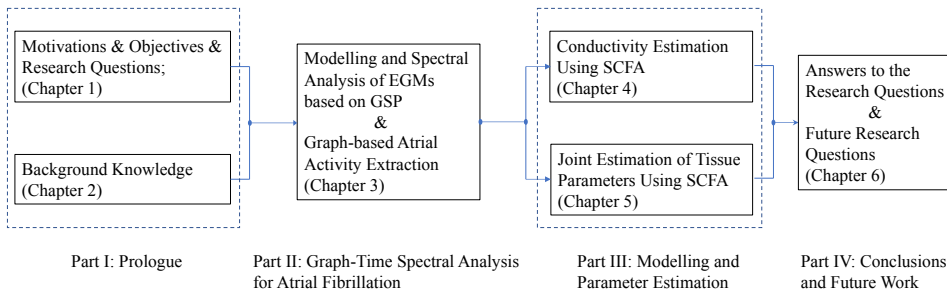


Figure 1.2: The structure of this dissertation.

1.3.1. CHAPTER 2: CARDIOLOGY FUNDAMENTALS AND RESEARCH BACKGROUND

In this chapter, we give an overview of the necessary background concepts of cardiology and the cardiac signal processing required for the readers to follow this dissertation. We first introduce the anatomy and physiology of human heart, including the important electrical conduction system. Then we introduce the electrical activity of the heart, starting from the action potential generation of a single cell to the action potential propagation across tissue. Next, normal and abnormal electrical activities of the heart are discussed and the specific cardiac arrhythmia that we are concerned with in this dissertation is introduced. After introducing the basic concepts about cardiology, we present

the mapping approach for EGM measurement that we use in this dissertation and compare the difference between the ECG and the EGM. Finally, we review the signal processing techniques to model and analyze the EGM data.

1.3.2. CHAPTER 3: GRAPH-TIME SPECTRAL ANALYSIS ON EGM

This chapter answers the research questions **Q1.1** and **Q1.2**. We start this chapter by explaining why graph signal processing techniques are considered in this study to model and analyze the EGM data. Then we summarize the background concepts in the research field of graph signal processing that provide the basics of the research in this chapter. To analyze the electrical activity in the heart at a higher-abstraction level using graph signal processing techniques, we first construct a graph to represent the spatial relations of multi-electrode data. Then we aim to use graph signal processing tools to analyze the temporal and spatial variation of the EGMs under normal and abnormal heart conditions to recognize the impact of AF on the atrial activity. Since the EGMs are time dependent and the atrial activation might vary from beat to beat, it is insufficient to use the graph Fourier transform - the predominant tool in graph signal processing-alone as it analyzes the spatial variability for a fixed time instant. To account for the temporal variability and capture the interaction between space and time, we propose the joint graph and short-time Fourier transform to capture the frequency content along both the time and the graph domain. With this technique, we are able to analyze the spatial variability of the electrogram temporal frequencies. Finally we found that the spatial variation of the atrial electrograms decreases during atrial fibrillation since the high temporal frequencies of the atrial waves reduce. The proposed analysis also confirms that the measured ventricular activities are smoother over the atrial area compared with the atrial activity.

Motivated by this finding from our graph-time spectral analysis of the ventricular activity, we further develop a more effective atrial activity extraction algorithm and finally answer research question **Q1.3**. Atrial signals in the electrograms taken from the atrial sites are naturally corrupted by the far-field ventricular activity. The capability of a method to extract the atrial activity is fundamental to promote it for atrial fibrillation studies. In this chapter, we present a novel atrial activity extraction algorithm based on the difference in graph smoothness between the atrial activity and the ventricular activity. The complexity of this algorithm is analyzed and the implementation is also explained. Experimental results on synthetic and real data show that the smoothness analysis of the EGMs over the atrial area enables us to better extract the atrial activity from the electrogram measurements. As a first exploration of graph signal processing applied to EGM data, this application helps to demonstrate the potential of graph signal processing techniques in the AF research area.

1.3.3. CHAPTER 4: CARDIAC TISSUE CONDUCTIVITY ESTIMATION USING CONFIRMATORY FACTOR ANALYSIS

In this chapter we shift our focus from the high-abstraction model to the more detailed electrophysiological model and extract useful tissue parameters that are related to the development of the cardiac arrhythmia. To utilize the spatial relationship of the data to estimate the target parameters, we propose the cross-power spectral density matrix

(CPSDM) model for the multi-electrode electrograms. This answers research question **Q2.1**. Subsequently, research questions **Q2.2** and **Q2.3** are concerned. We make use of an effective method called confirmatory factor analysis (CFA) to estimate the tissue conductivity and the anisotropy ratio parameters from the CPSDM model. The general CFA problem is reviewed for the convenience of the readers and is then extended to our specific problem. The identifiability conditions in the CFA problem can be used to find the relationship between the desired resolution and the required amount of data. To make more efficient use of the data, we propose simultaneous CFA to estimate the parameters simultaneously in multiple frequencies such that a smaller amount of data is required for the same target resolution. Numerical experiments on the simulated data demonstrate that the proposed method can localize the tissue areas of slow conduction and can also identify the smoother variation in the conductivities. An evaluation on the clinical data shows that the EGMs reconstructed based on the estimated parameters match well with the EGMs measured from patients.

1.3.4. CHAPTER 5: JOINT ESTIMATION OF EGM MODEL PARAMETERS USING CONFIRMATORY FACTOR ANALYSIS

In chapter 4 we have proposed to use CFA to estimate tissue parameters from the electrogram measurements. However, the method is limited to the use of a single heart beat and could only estimate the conductivity and the anisotropy ratio. In this chapter, we further extend this algorithm to jointly estimate the conductivity, anisotropy ratio, as well as the activation time per cell and thus further explore research question **Q2.2**. With the reasonable assumptions that the conductivity parameters and the anisotropy parameters are constant across different frequencies and heart beats, we estimate these parameters using multiple frequencies and multiple heart beats simultaneously to easier satisfy the identifiability conditions in the CFA problem. Results on the simulated data show that using multiple heart beats further improve the estimation accuracy of the parameters. The experimental results on clinical data show that using multiple heart beats for parameter estimation can reduce the reconstruction errors of the clinical electrograms, which further demonstrates the robustness of the proposed method.

1.3.5. CHAPTER 6: CONCLUSIONS AND FUTURE WORK

In this chapter, we summarize the contributions of this dissertation and draw the respective conclusions. We also discuss some open questions of this research and the future directions for solving these questions.

1.4. LIST OF PUBLICATIONS

All papers and abstracts submitted and published during the PhD period are listed in this section.

JOURNALS

1. **M. Sun**, E. Isufi, N. M.S. de Groot and R. C. Hendriks, *Graph-time spectral analysis for atrial fibrillation*, Biomedical Signal Processing and Control, vol. 59, 2020.

2. **M. Sun**, N. M.S. de Groot and R. C. Hendriks, *Cardiac Tissue Conductivity Estimation Using Confirmatory Factor Analysis*, Computers in Biology and Medicine, vol. 135, 2021.
3. **M. Sun**, N. M.S. de Groot and R. C. Hendriks, *Joint Cardiac Tissue Conductivity and Activation Time Estimation Using Confirmatory Factor Analysis*, Computers in Biology and Medicine, vol. 144, 2021.

CONFERENCES (FULL PAPERS)

1. **M. Sun**, E. Isufi, N. M.S. de Groot and R. C. Hendriks, *A Graph Signal Processing Framework for Atrial Activity Extraction*, European Signal Processing Conference (EUSIPCO), pp. 1-5, 2019.

CONFERENCES (ABSTRACTS)

1. **M. Sun**, N. M.S. de Groot and R. C. Hendriks, *Joint Estimation of Parameters in Cardiac Tissue Using Confirmatory Factor Analysis*, Dutch Bio-Medical Engineering Conference, 2022.
2. **M. Sun**, N. M.S. de Groot and R. C. Hendriks, *Estimation of Cardiac Tissue Conductivity Using Confirmatory Factor Analysis*, Dutch Bio-Medical Engineering Conference, 2021.
3. **M. Sun**, E. Isufi, N. M.S. de Groot and R. C. Hendriks, *Atrial Activity Extraction Based on Graph-Time Signal Processing*, the 40th WIC Symposium on Information Theory and Signal Processing, 2019.
4. **M. Sun**, E. Isufi, N. M.S. de Groot and R. C. Hendriks, *Atrial Activity Extraction Based on Graph-Time Signal Processing*, Graph Signal Processing, 2019.

REFERENCES

- [1] World Health Organization, *Global action plan for the prevention and control of noncommunicable diseases 2013-2020*, World Health Organization, 2013.
- [2] A. J. Camm, P. Kirchhof, G. Y. H. Lip, et al., "Guidelines for the management of atrial fibrillation: the task force for the management of atrial fibrillation of the european society of cardiology (ESC)," *European Heart Journal*, vol. 31, no. 19, pp. 2369–2429, 2010.
- [3] C. T. January, L. S. Wann, J. S. Alpert, et al., "2014 AHA/ACC/HRS guideline for the management of patients with atrial fibrillation: a report of the American College of Cardiology/American Heart Association Task Force on Practice Guidelines and the Heart Rhythm Society," *Journal of the American College of Cardiology*, vol. 64, no. 21, pp. e1–e76, 2014.
- [4] W. B. Kannel, P. A. Wolf, E. J. Benjamin, and D. Levy, "Prevalence, incidence, prognosis, and predisposing conditions for atrial fibrillation: population-based estimates," *The American Journal of Cardiology*, vol. 82, no. 7, pp. 2N–9N, 1998.

- [5] A. Ott, M. M. B. Breteler, M. C. de Bruyne, et al., “Atrial fibrillation and dementia in a population-based study: the rotterdam study,” *Stroke*, vol. 28, no. 2, pp. 316–321, 1997.
- [6] A. Yaksh, L. J. M. E. van der Does, et al., “A novel intra-operative, high-resolution atrial mapping approach,” *Journal of Interventional Cardiac Electrophysiology*, vol. 44, no. 3, pp. 221–225, 2015.
- [7] R. H. Clayton, O. Bernus, E. M. Cherry, et al., “Models of cardiac tissue electrophysiology: progress, challenges and open questions,” *Progress in Biophysics and Molecular Biology*, vol. 104, no. 1-3, pp. 22–48, 2011.
- [8] C. S. Henriquez, “A brief history of tissue models for cardiac electrophysiology,” *IEEE Transactions on Bio-medical Engineering*, vol. 61, no. 5, pp. 1457, 2014.
- [9] B. M. Johnston and P. R. Johnston, “Approaches for determining cardiac bidomain conductivity values: progress and challenges,” *Medical & Biological Engineering & Computing*, pp. 1–17, 2020.
- [10] N. Perraudin and P. Vandergheynst, “Stationary signal processing on graphs,” *IEEE Transactions on Signal Processing*, vol. 65, no. 13, pp. 3462–3477, 2017.
- [11] M. Newman, *Networks*, Oxford university press, 2018.
- [12] W. Huang, L. Goldsberry, N. F. Wymbs, et al., “Graph frequency analysis of brain signals,” *J. Sel. Topics Signal Processing*, vol. 10, no. 7, pp. 1189–1203, 2016.
- [13] J. D. Medaglia, W. Huang, E. A. Karuza, et al., “Functional alignment with anatomical networks is associated with cognitive flexibility,” *Nature Human Behaviour*, vol. 2, no. 2, pp. 156–164, 2018.
- [14] W. Huang, T. A. Bolton, J. D. Medaglia, et al., “A graph signal processing perspective on functional brain imaging,” *Proceedings of the IEEE*, vol. 106, no. 5, pp. 868–885, 2018.
- [15] C. Hu, J. Sepulcre, K. A. Johnson, et al., “Matched signal detection on graphs: theory and application to brain imaging data classification,” *NeuroImage*, vol. 125, pp. 587–600, 2016.
- [16] T. H. Everett, L. Kok, R. H. Vaughn, et al., “Frequency domain algorithm for quantifying atrial fibrillation organization to increase defibrillation efficacy,” *IEEE Transactions on Biomedical Engineering*, vol. 48, no. 9, pp. 969–978, 2001.
- [17] E. Isufi, A. S. Mahabir, and G. Leus, “Blind graph topology change detection,” *IEEE Signal Processing Letters*, vol. 25, no. 5, pp. 655–659, 2018.
- [18] H. Behjat, N. Leonardi, L. Sörnmo, and D. Van De Ville, “Anatomically-adapted graph wavelets for improved group-level fmri activation mapping,” *NeuroImage*, vol. 123, pp. 185–199, 2015.

- [19] Y. Guo, H. Nejati, and N. Cheung, “Deep neural networks on graph signals for brain imaging analysis,” in *IEEE International Conference on Image Processing (ICIP)*. IEEE, 2017, pp. 3295–3299.
- [20] E. J. Ciaccio, A. B. Biviano, W. Whang, et al., “Differences in repeating patterns of complex fractionated left atrial electrograms in longstanding persistent atrial fibrillation as compared with paroxysmal atrial fibrillation,” *Circulation: Arrhythmia and Electrophysiology*, vol. 4, no. 4, pp. 470–477, 2011.
- [21] C. Spearman, “The proof and measurement of association between two things,” *The American Journal of Psychology*, vol. 15, no. 1, pp. 72–101, 1904.
- [22] T. W. Anderson, H. Rubin, et al., “Statistical inference in factor analysis,” in *Proceedings of the third Berkeley symposium on mathematical statistics and probability*, 1956, vol. 5, pp. 111–150.
- [23] D. N. Lawley and A. E. Maxwell, “Factor analysis as a statistical method,” *Journal of the Royal Statistical Society. Series D (The Statistician)*, vol. 12, no. 3, pp. 209–229, 1962.
- [24] K. G. Jöreskog, “A general approach to confirmatory maximum likelihood factor analysis,” *Psychometrika*, vol. 34, no. 2, pp. 183–202, 1969.
- [25] K. G. Jöreskog and D. N. Lawley, “New methods in maximum likelihood factor analysis,” *British Journal of Mathematical and Statistical Psychology*, vol. 21, no. 1, pp. 85–96, 1968.
- [26] A.-J. Van der Veen, A. Leshem, and A.-J. Boonstra, “Signal processing for radio astronomical arrays,” in *Processing Workshop Proceedings, 2004 Sensor Array and Multichannel Signal*. IEEE, 2004, pp. 1–10.
- [27] A. Sardarabadi, *Covariance matching techniques for radio astronomy calibration and imaging*, Ph.D. thesis, TU Delft, Fac. EEMCS, Delft, The Netherlands, Jun. 2016, ISBN 978-94-6186-670-7.
- [28] A. I. Koutrouvelis, R. C. Hendriks, R. Heusdens, et al., “Robust joint estimation of multimicrophone signal model parameters,” *IEEE/ACM Transactions on Audio, Speech, and Language Processing*, vol. 27, no. 7, pp. 1136–1150, 2019.

2

CARDIOLOGY FUNDAMENTALS AND RESEARCH BACKGROUND

IN Chapter 1 we presented the motivation and the objectives of this dissertation. In this chapter, we provide an overview of the background information that is needed to read this dissertation. The cardiology fundamentals are given first, including the anatomy, the electrical conduction system, and the normal and the abnormal electrical activities of human heart. In Section 2.3, we introduce the specific cardiac arrhythmia called atrial fibrillation (AF), which we are concerned with in this dissertation. To investigate this arrhythmia we use epicardial electrograms (EGMs) measured from human atria during normal sinus rhythm (SR) and AF. The mapping approach to measure the data and the details of the EGM data are further explained in Section 2.4. Then in Sections 2.5 and 2.6 we present the signal processing techniques to model and analyze the EGM data.

2.1. ANATOMY AND PHYSIOLOGY OF HUMAN HEART

2.1.1. ANATOMY OF HUMAN HEART

The human cardiovascular system is to deliver oxygen and nutrients to the different organs and remove waste products. The heart plays an important role in the cardiovascular system as it pumps blood through a closed system of blood vessels. It is located between the lungs and slightly to the left sternum and rests on the superior surface of the diaphragm.

The human heart consists of four chambers, including the two upper chambers known as the left atrium (LA) and the right atrium (RA) and the two lower chambers known as the left ventricle (LV) and the right ventricle (RV). The atria receive blood returning from the lungs and the body and contract to push blood to the ventricles, while the ventricles act as the primary pumping chambers that propels blood from the heart to the lungs and the rest of the body. The atrio-ventricular (AV) valves located between the upper and the lower chambers prevent the back flow of the blood. Therefore, under normal circumstances, the blood flows in one direction from the atria to the ventricles. The right side of

the heart receives deoxygenated blood that is pumped to the lungs while the left side of the heart receives oxygenated blood that is pumped to the body. The heart wall is composed of three layers, including the epicardium, the myocardium, and the endocardium [1]. The atria have thinner walls (about 0.6-4.5 mm for the RA and 0.7-4.3 mm for the LA [2]) compared to the ventricles (about 3–5 mm for the RV and 12–15 mm for the LV [3]), as the atria receive the blood while the ventricles have to pump blood through the body. The outermost layer of the heart wall is the epicardium [1]. The data for our research is measured at the epicardial sites of the atria. Figure 2.1 shows the anatomy of the human heart.

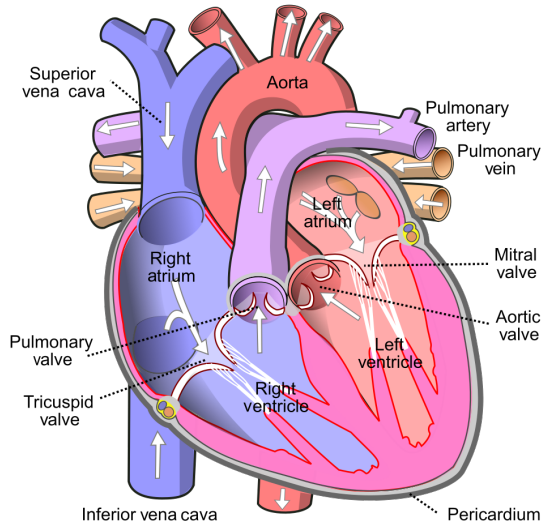


Figure 2.1: Anatomy of the human heart [4].

2.1.2. THE ELECTRICAL CONDUCTION SYSTEM OF THE HEART

The heart contains specialized fibres that can initiate electrical impulses and conduct them through the heart. These are known as the junctional tissues or the conduction system of the heart. This conduction system mainly consists of the sinoatrial (SA) node, the atrioventricular (AV) node, the bundle of His, the left and right bundle branches, and the Purkinje fibres, as shown in Figure 2.2.

The SA node is the natural pacemaker of the heart. Under normal conditions, the SA node automatically releases electric stimuli and initiates a the normal cardiac impulse at a regular rate. The impulse initiated from the SA node then spreads throughout the entire atria, causing the atria to contract. There is a specialized pathway called Bachmann's bundle that conducts the impulse directly from the right atrium to the left atrium. The impulse then reaches the AV node. The AV node delays the impulse before the impulse is transmitted to the AV bundle, which is about 0.09 s. This delay provides enough time for the atria to empty their blood into the ventricles. After this delay the impulse travels

through the AV bundle and its branches to the Purkinje fibers. The Purkinje fibers then conduct the impulse rapidly and almost synchronously to the myocardium of the ventricles, causing the ventricles to contract. As the ventricles contract, the right ventricle pumps blood to the lungs where carbon dioxide is released and oxygen is absorbed, and at the same time the left ventricle pumps blood into the aorta and from there it passes into the coronary and arterial circulation. Once the ventricles become empty, the atria are full and the valves between them are closed. Then the SA node will release another electric stimuli and the whole process will be repeated [1].

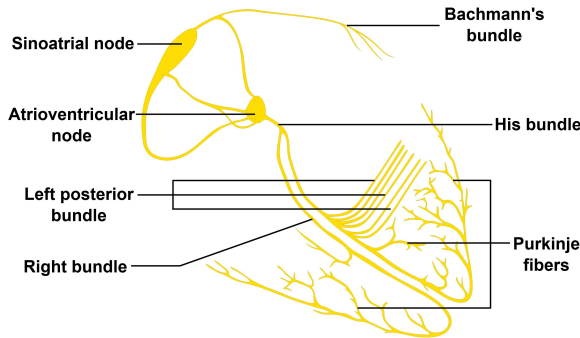


Figure 2.2: The conduction system of the human heart [4].

2.2. ELECTRICAL ACTIVITY OF THE HEART

2.2.1. CARDIAC CELL MEMBRANE ACTION POTENTIAL

Pacemaker cells in the SA node can initiate and conduct impulses to excite their neighbouring cells. These neighbouring cells further conduct the impulses, generating a spread of excitation. When a cardiac cell is at its resting state, its membrane potential is about -90 mV. The resting membrane potential results from the flux of ions (e.g., Na^+ and Ca^{2+}) flowing into the cell and the ions (e.g., K^+ and Cl^-) flowing out of the cell. The concentration difference of these ions between the intracellular and extracellular regions is maintained by the activity of pumps, which moves ions against the concentration gradient using energy in the form of adenosine triphosphate (ATP) [5].

Once a cell is excited by the stimulus, its transmembrane potential rapidly increases until a threshold is reached and an action potential pulse is generated. Figure 2.3(a) shows an example of the action potential of a cardiac cell. The action potential of a cardiac cell is nonlinear and can be divided into five phases [5]. Figure 2.3(b) shows the flow of the ions in different phases. Each phase is explained as follows:

- *Phase 0 (depolarization)*: When a cell is stimulated, the voltage-gated sodium channels of the cell rapidly open and the depolarization of the cell happens due to the influx of the Na^+ ions. This rapid influx of Na^+ ions raises the membrane potential to about $+20$ mV, at which point the Na^+ channels close.

- *Phase 1 (initial repolarization)*: The Na^+ channels close, the cell begins to repolarize

and the K^+ ions leave the cell through the K^+ channels. This early repolarization lasts only 3 - 5 ms.

- *Phase 2 (plateau)*: After the brief initial repolarization, the cell changes into Phase 2, the plateau phase, in which membrane potential decreases relatively slowly. In this phase, the opening of the Ca^{2+} channels allows Ca^{2+} to pass into the cell, while few K^+ channels also open so that K^+ can pass out the cell. The combination of the decreased K^+ ions efflux and the increased Ca^{2+} ions influx causes the action potential to plateau. This phase is relatively long and lasts about 175 ms.

- *Phase 3 (rapid repolarization)*: Once the membrane potential declines to about zero, the Ca^{2+} channels close and K^+ channels open that allows K^+ to rapidly pass out the cell. This is Phase 3, the late rapid repolarization, which lasts about 75 ms.

- *Phase 4 (resting membrane potential)*: In phase 4, the action potential decreases to a more negative value and starts to approach the resting potential. During this phase, the cell membrane is most permeable to K^+ and the resting membrane potential is mainly determined by K^+ equilibrium potential. Every time a K^+ flows from the inside to the outside of the cell, the intracellular region loses a positive charge. The intracellular region becomes more positive relative to the extracellular region, which establishes the electric field across the cell membrane that makes it harder for the K^+ ions to leave the cell and attracts the K^+ to flow to the inside of the cell membrane.

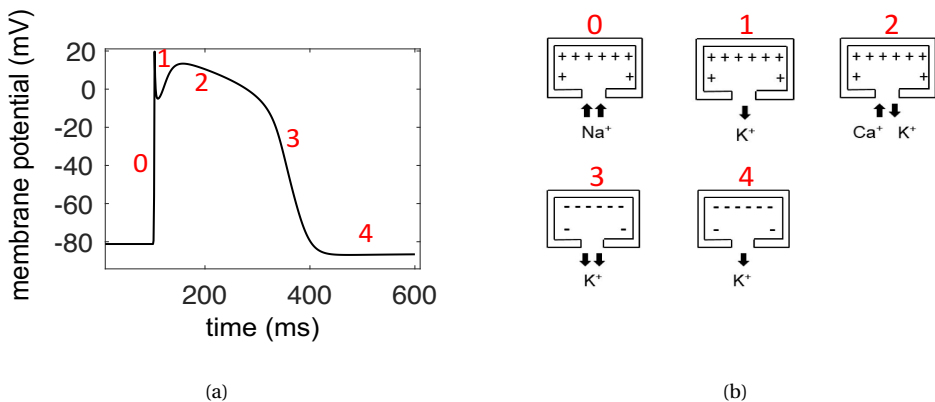


Figure 2.3: Action potential of a cardiac cell and the different phases of the cardiac action potential. (a) Action potential of a cardiac cell. The numbers represent the different phases. (b) The flow of the ions in the five phases.

Once the action potential is initiated, the cardiac cell cannot respond to other stimuli for some duration of time. This period is slightly shorter than the complete duration of the action potential and is called the *refractory period*. The *refractory period* lasts about 250 ms and helps to protect the heart. The refractory period can be further divided into the *absolute refractory period* and the *relative refractory period*. The *absolute refractory period* starts when the Na^+ channels close and enter an inactive state. The *relative refractory period* starts when the Na^+ channels slowly recover from the inactive state. A cell cannot be excited by any other stimuli during the *absolute refractory period*, while

it can be excited with stimuli that are stronger than the one normally needed to initiate the action potential during the *relative refractory period*.

2.2.2. ACTION POTENTIAL PROPAGATION

Action potentials propagate along the cell membranes via local currents. The speed and the pattern of action potential propagation depends on the micro-structure of cardiac tissue. Cardiac tissue consists mostly of cardiac muscle cells. The intracellular and extracellular spaces are filled with conducting fluid and act like volume conductors. The intracellular spaces of adjacent cells are connected by the low-resistance gap junctions, which enable the intercellular signalling and propagation of the action potentials. With this structure, the upstroke of the action potential in a cell membrane can trigger the opening of voltage-gated Na^+ channels in the neighboring cells, resulting in the propagation of the action potential through cardiac tissue [5, 6].

At the cellular scale, the action potential propagation is a discrete process, since there is a delay between the depolarization of a myocyte and its neighbouring cells due to the effect of the gap junctions that connect them [7]. To simplify the mathematical description of the tissue, it is common to neglect the discrete nature of the action potential propagation, since the depolarization propagates smoothly at larger spatial scales. The propagation of the action potentials can then be regarded as continuous. In this dissertation we also use this assumption to simplify the mathematical modelling of the action potential propagation.

2.2.3. CARDIAC ARRHYTHMIA - ABNORMAL ACTION POTENTIAL GENERATION

Cardiac arrhythmias are known as disturbances that occur in the electrical activity of the heart. During an arrhythmia, the heart rhythm can be too fast, too slow, or irregular. When the heart rate exceeds 100 beats per minute, it is called a tachycardia; when the heart rate is too slow (lower than 60 beats per minute), it is called a bradycardia. When the arrhythmias are initiated in the areas above the heart's lower chambers, such as the atria or the atrial conduction pathways, they are called supraventricular arrhythmias. If the arrhythmias are initiated in the ventricles, they are called ventricular arrhythmias.

Cardiac arrhythmias can be caused by severe disfunctions in the electrical conduction system of the heart. Due to the damage of the SA node, it may stop playing the role as the natural pacemaker of the heart, leading to the irregular beating of the heart. Arrhythmia can also arise due to a blockage of the conduction from the SA node [8]. The most common blockage is the AV blockage, which arises from a pathology at the AV node that may be caused by ischemia or fibrosis from myocardial infarction, myocarditis from a viral infection or other factors. In some cases, the abnormal propagation of the action potential is caused by scar tissue. Due to the scar, the action potential will change its normal pathway and travel around the scar area to depolarize the rest of the tissue. This can create a circuit as the action potential starts to propagate in a circular manner. Other health issues such as anxiety, fever, pregnancy or the use of drugs, can also affect both the anatomy and physiology of the heart. While most cardiac arrhythmias are not serious and do not cause complications, some, however, can increase the risk of stroke, heart failure, or even sudden death.

2.3. ATRIAL FIBRILLATION

2.3.1. WHAT IS ATRIAL FIBRILLATION?

Atrial fibrillation (AF) is the most common type of arrhythmia characterized by the rapid and irregular beating of the atria. It is classified as a supraventricular tachycardia. During AF, the SA node might lose its control on the heart and the electrical impulses originate from somewhere in the atria, causing the atria to contract in a disorganized fashion. The abnormal signals propagate through the atrial walls and stimulate the atria at a very fast rate of 300 to 600 beats per minute, causing the atria to quiver (fibrillate). The disorganized signals are then transmitted to the ventricles and cause them to contract irregularly. Under this condition, the atria do not coordinate with the ventricles as it does in a normal heart condition [9].

Due to the abnormal beating of the atria, the blood cannot be pumped efficiently from atria to ventricles and might pool in the atria. This pooling can cause the formation of blood clots inside the heart, mostly inside the left atrium, and in particular in the left atrial appendage. These clots can be pumped out of the heart, travel through the bloodstream and finally reach the brain, causing a stroke [10]. Hence, AF significantly increases the risk for stroke.

2.3.2. MECHANISMS UNDERLYING AF

The precise mechanisms underlying AF are still not well understood. The guidelines approved by the American College of Cardiology (ACC), the American Heart Association (AHA), and the Heart Rhythm Society (HRS) in 2014 discuss the mechanisms underlying AF from different angles including atrial structural abnormalities, electrophysiological mechanisms, and pathophysiological mechanisms [9].

Atrial structural abnormalities: The susceptibility to AF can be increased due to any disturbance of the atrial structure. Changes such as inflammation, fibrosis and hypertrophy are most commonly found in heart diseases associated with hypertension, coronary artery disease and valvular heart disease. These changes are likely to increase the left atrial pressure, leading to atrial dilation or altering the wall stress. Extracardiac factors, which have pathophysiological effects on the structure or function of cardiac cell structure can also increase the risk of AF, such as hypertension, sleep apnea, obesity, and hyperthyroidism [9].

Electrophysiological mechanisms: There are also studies trying to explain the electrophysiological mechanisms of AF, including the initiation and the maintenance of AF. Figure 2.4 illustrates several of the proposed mechanisms initiating and maintaining AF. Ectopic focal sources can often initiate AF. They are most commonly found in the pulmonary veins and are also identified in other sites like the posterior left atrium, coronary sinus, venae cavae, appendages, etc. Isolated pulmonary vein myocytes can also trigger activity that can promote rapid focal firing. The rapidly firing foci contribute to the maintenance of AF. In addition, single re-entry circuits and multiple independent re-entry wavelets also maintain a self-sustaining AF, where ‘re-entry’ is defined as the repetitive excitation of tissue by a recirculating wavefronts [11]. Conduction abnormalities in cardiac tissue can promote reentry of wave fronts. Concepts of stable rotors, unstable fibrosis-linked rotors and epicardial–endocardial dissociation are also proposed

to explain the electrophysiological mechanisms underlying AF [12]. Triggers for initiations and anatomic substrate for maintenance of AF are potential targets for the therapy methods on the patients [9].

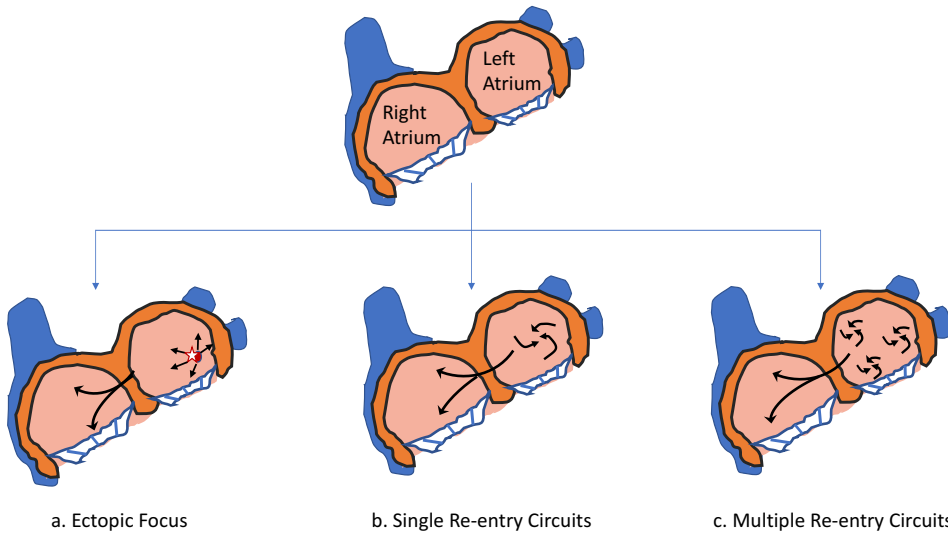


Figure 2.4: Illustration of the classical electrophysiological mechanisms underlying atrial fibrillation. The disorders in atria can be maintained through different mechanisms like (a) a rapidly firing ectopic focus, (b) single re-entry circuit, (c) multiple re-entry circuits (redrawn after [11]).

Pathophysiological mechanisms: The third group of mechanisms are the pathophysiological mechanisms of AF. It has been shown that AF can cause electrical and structural remodeling of the atria that further increases the severity of AF. The success rate of restoration to sinus rhythm (SR) from AF is higher for patients having AF for less than 6 months. Previous research also showed that inflammation or oxidative stress may be linked to AF. There are also other risk factors for AF such as obesity, cardiothoracic surgery, smoking, alcohol use, etc [9].

2.3.3. CLASSIFICATION OF AF

As AF progresses with time, patients with AF are more likely to have more severe mobility problems. It has been found that the duration of AF episodes has clinical relevance since the outcome of therapy methods such as cardiac ablation are better for paroxysmal AF than for persistent AF [13]. Therefore, early detection and diagnosis of AF is important to avoid later complications. In order to be able to properly address the problems, it is necessary to classify the various subsets of patients with AF. The American College of Cardiology (ACC), the American Heart Association (AHA), and the European Society of Cardiology (ESC) have recommended in their guidelines [14] to classify AF into five patterns based on the presentation, duration, and spontaneous termination of AF episode, as shown in Table 2.1.

Table 2.1: Classification of AF [14]

AF Pattern	Definition
First Diagnosed	AF that is not diagnosed previously, without consideration of its duration or the presence/severity of AF-related symptoms.
Paroxysmal	AF that stops spontaneously in less than seven days.
Persistent	AF that lasts more than seven days.
Longstanding Persistent	Continuous AF that lasts more than 12 months.
Permanent	AF that is accepted by the patient and the physician, and no further attempts will be undertaken to restore sinus rhythm.

2.3.4. TREATMENT OF AF

There are different therapy methods proposed to cure patients with AF according to the degree of the disease. Three goals are often concerned in the treatment of AF, including rate control, stroke prevention and maintenance of the sinus rhythm. Rate control mainly concentrates on reducing the heart rate, which decreases morbidity and reduces the potential of developing tachycardia-induced cardiomyopathy. Beta blockers, nondihydropyridine calcium channel blockers, digoxin, and certain antiarrhythmic drugs including amiodarone and sotalol have been recommended to control the heart rate [9]. Although an initial rate control is reasonable for many patients, rhythm control strategy is also considered to restore and maintain sinus rhythm for patients with long-term AF. The rhythm-control strategy combines different approaches, including cardioversion, antiarrhythmic drugs, and radiofrequency catheter ablation with appropriate setting of anticoagulation and rate control [9].

AF contributes to about one-third of hospitalizations for cardiac arrhythmias. Treatment of AF is expensive. The clinical care for patients with AF includes hospital costs, medication, follow-up, disability and emergency measures, which contribute to about 1% of the National Health Service budget in the United Kingdom and about 20 billion dollars per year in the United States [15]. Treatment still remains suboptimal since the precise mechanisms underlying AF are still not well understood. It is important to get a better understanding of AF in the individual patient to improve the efficiency and successful rate of the therapy methods. Cardiac mapping plays an important role to obtain the necessary measurements to investigate the arrhythmogenic substrate for the selection of optimal treatment.

2.4. MEASURING THE CARDIAC ELECTRICAL ACTIVITY

2.4.1. ATRIAL MAPPING APPROACH

During cardiac mapping, the electrical activity in cardiac tissue is recorded directly from the surface of the heart. AF patients have a large variety of disorders which may give rise to differences in individuals. The inter-individual differences in the mechanisms un-

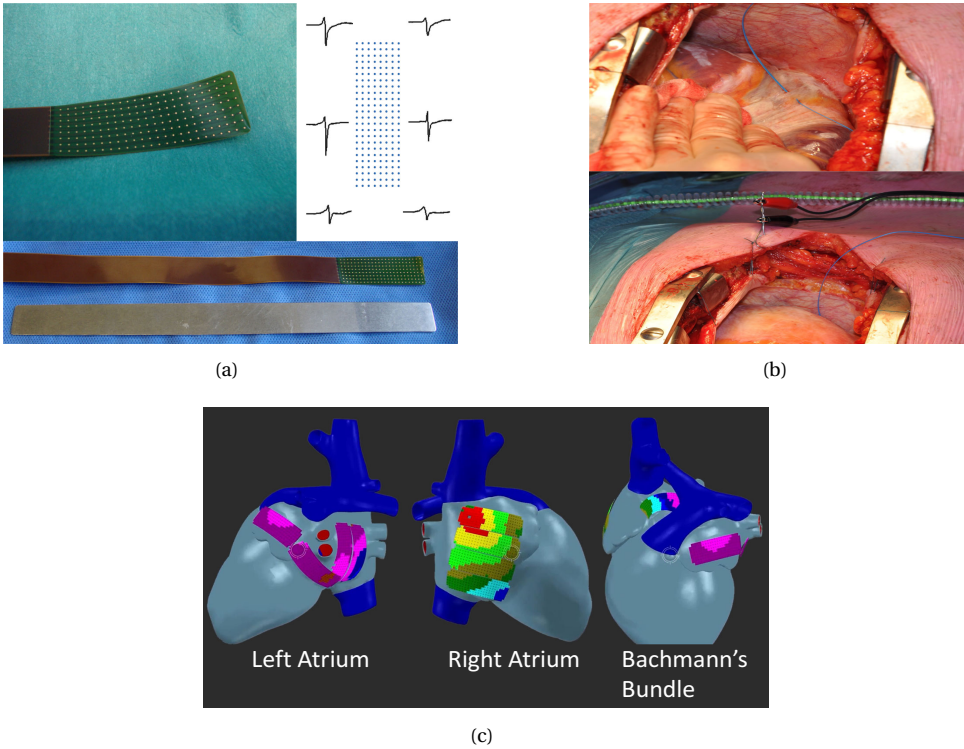


Figure 2.5: Illustration of the mapping technique and recordings. (a) Top left: mapping array with 192 unipolar electrodes; top right: Examples of the recorded EGMs at the proximal, the middle and the distal electrodes of the array; bottom: the mapping array and the identically shaped steel spatula. (b) Top: a pacemaker wire stitched to the right atrial free wall that is served as a temporal reference electrode; bottom: a steel wire fixed to (sub)cutaneous tissue that is served as the indifferent electrode. (c) Mapping scheme (showing the activation time maps on the 3D models) [16].

derlying AF need to be considered and multisite high-resolution mapping of the entire atria is necessary [16]. In the last two decades, much progress has been made in developing high-resolution microelectrode arrays, which allow to obtain the measurements from atrial tissue with high spatial-temporal resolution. With the high resolution mapping approach, it is now possible to directly and efficiently measure the transmembrane potential propagation from the parallel measurements of the atria at different sites.

In this dissertation, we use the epicardial electrogram data measured using a high resolution mapping approach presented in [16]. This approach uses a mapping array of 8×24 electrodes with an inter-electrode distance of 2 mm to collect data during open-heart surgery. During the measurement, 188 electrodes record the unipolar EGMs; three of the remaining electrodes record the body surface ECG signal, the reference signal, and the calibration signal, respectively; the last electrode is not used. The electrogram comprises five seconds of recording during sinus rhythm and ten seconds during AF with a sampling rate of 1 kHz. AF was induced manually by rapid pacing in the right atrial free

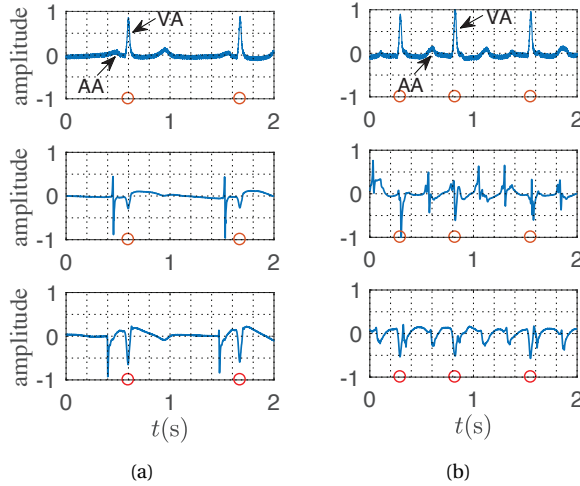


Figure 2.6: Examples of the body surface electrocardiogram (ECG) and epicardial electrogram (EGM) across time at one electrode during (a) sinus rhythm and (b) atrial fibrillation. AA: atrial activity; VA: ventricular activity. *Top*: ECG; *middle* and *bottom*: EGMs at different electrodes. The red circles mark the peak of the ventricular activity determined by the ECG measurements.

wall with the procedure detailed in the original publication [16]. Figure 2.5 illustrates the mapping technique. All measurements were taken in the Erasmus Medical Center, The Netherlands, during 2014–2016 with procedures approved by the Medical Ethical Committee (MEC 2010-054 & MEC 2014-393) [17, 18]. Further details about the data acquisition system are reported in [16].

2.4.2. ECG vs. EGM

Different types of data have been investigated to study AF and both the non-invasive body surface electrocardiograms (ECGs) and the invasive epicardial electrograms (EGMs) are widely used. Compared to ECGs, the EGMs are measured on the heart's surface using multiple electrodes and have a higher spatial resolution. This improved resolution makes EGMs appealing to analyze AF over both space (the heart surface) and time.

Figure 2.6 illustrates the ECGs and the EGMs during SR and AF for one patient. In the ECG (top plots in Figures 2.6(a) and 2.6(b)), the high peaks indicate the ventricular activity, while the lower peaks before them indicate the atrial activity. The atrial activity appears weak compared with the ventricular activity. In the EGM measurements (middle and bottom plots in Figures 2.6(a) and 2.6(b)), the atrial activity is more pronounced, albeit short in duration. This difference is due to spatial averaging occurring when measuring the atrial signal on the body surface, compared with when measuring it on the epicardium.

The EGMs measured by the different electrodes (middle and bottom plots in Figure 2.6(a)) show a time delay when measuring the atrial activity in different positions. However, they do not show any obvious time delay when measuring the ventricular activity.

This is because the mapping array is close to the atria and far from the ventricle. Also, the amplitudes of the ventricular activity are different at different electrodes due to the propagation attenuation.

The above discussion highlights the limitations of the body surface ECG—the atrial activity in there is weak and gets easily corrupted by noise; hence, rendering the time-frequency analysis unreliable. Although several proposed invasive methods measured a stronger atrial activity, they used low-resolution mapping arrays and analyzed the data only in time or temporal frequency domain [19–22]. Differently, we consider high-resolution epicardial measurements and analyze the data in the joint space, time, and frequency domain, which will be further discussed in Chapter 3.

2.5. PREPROCESSING AND ANALYSIS OF THE EGMs

2.5.1. PREPROCESSING

As introduced in Section 2.4, we use the atrial EGMs measured from patients using a microelectrode array. During the recording, the measurements are often corrupted by the strong far-field ventricular activities and other interferences. Some preprocessing approaches have been employed to the EGMs during recording, including amplification (gain 1000), band-pass filtering (bandwidth 0.5 Hz to 400 Hz), sampling (1 kHz), and analogue to digital conversion (16 bits). In this study we visually selected the relatively clean EGMs for further analysis.

Removing the far-field ventricular activities from the EGMs is more complicated. Although the atrial activity and the ventricular activity are well separated in time during SR due to the time-delay at the AV node of the heart, they may overlap during AF since the atria are beating rapidly and irregularly. As shown in Figure 2.6(b), we see that during AF, the atrial and the ventricular activities are difficult to distinguish since they appear irregular and they overlap. In other words, the ventricular activity affects the analysis of the atrial activity; hence, extracting the atrial activity from the measurement is critical for atrial fibrillation research.

One commonly applied technique to extract atrial activity is called template matching and subtraction [23–25], which generates a template of the ventricular activity and then subtracts it from the raw measurements. Average beat subtraction (ABS) [23] is a simple but effective implementation of this technique. However, it cannot adapt well to changes in the morphology of the electrogram. Another technique, called adaptive ventricular cancellation (AVC) [26], is proposed to solve this problem. However, its performance is not stable as it depends on a reference recording, usually obtained from another lead. For surface ECG recordings, signal separation algorithms such as principal component analysis (PCA) [27] and independent component analysis (ICA) [26, 28] are also explored for atrial activity extraction. However, the assumptions about the distribution and independence of the ECG components may not hold for the EGMs. In this dissertation, we make use of a natural tool for high-dimensional and irregular data, which is a graph, to represent this data. Then we analyze the spatial variation of the atrial activity and the ventricular activity and separate the two using tools from graph signal processing [29]. The details of this approach will be introduced in Chapter 3.

2.5.2. SPECTRAL ANALYSIS AND CARDIAC ARRHYTHMIA

Spectral analysis is an important tool to investigate the behaviour of normal and abnormal cardiac signals, since this technique can decompose a waveform into its frequency components and further detect the periodicities of the signals in the frequency domain. As a well-known tool in the signal processing area, the discrete Fourier transform has been widely applied to transform cardiac signals from the time domain to the frequency domain to perform spectral analysis on the cardiac signals.

The dominant frequency (DF) has been widely used to analyze the spectrum of cardiac electrograms during AF. It is defined as the frequency of the signal at which the power spectrum of the signal has the maximum value. Some studies of AF employing DF suggested that a high DF may help to characterize the fast periodic activation in atrial tissue areas triggered by ectopic foci sources or re-entry circuits, which can be further applied to guide AF therapy like catheter ablation [30–34]. Based on the DF analysis, the studies on the organization index (OI) [35] and the regularity index (RI) [36] were carried out to measure the AF organization. While the OI represents the ratio of the area under the DF peak and its harmonics to the total area of the magnitude spectrum, the RI represents the ratio of the area only under the DF peak to the total area of the magnitude spectrum.

Although sites of high DF have been suggested to indicate the location of drivers of AF, there are still doubts on it as other investigators also reported significant instability of DF during prolonged recordings [37, 38]. The findings in [38] demonstrated that focal areas of high DF are spatiotemporally unstable and are not the source of centrifugal activation which shows concentric activation of the atrium from a localized area, and therefore are not indicative of fixed drivers of AF. The authors also argued that lines of block or turning points in tissue can also cause an increase in the measured DF at these sites and locations of high-frequency activation are more likely to be sites of summated complex activation, resulting from complex incident activation and not due to source activity. Therefore, DF-guided ablation is still unreliable and may cause excessive atrial myocardial destruction.

Taken altogether, spectral analysis on EGMs needs to be further explored to obtain a better understanding of AF. Experience in signal processing suggests that incorporating the spatial dimension into the spectral analysis helps to achieve understanding on the signals. In this dissertation, we propose a novel framework to study the EGMs in the joint space, time, and frequency domain based on graph signal processing theory.

2.5.3. SPECTRAL ANALYSIS USING GRAPH SIGNAL PROCESSING

The EGMs considered in this work are measured at the epicardial sites of the atria by an electrode array. These data are spatially high dimensional and exhibit irregular properties during AF. The natural tools to represent such data are graphs, as graphs have proven their ability to capture the underlying structure of high-dimensional and irregular data. Graph signal processing for analyzing and processing signals that reside on top of graphs has attracted more and more attention in recent years due to its ability to analyze big data with complex underlying structure [29]. The variation of graph signals have been explored to formulate a spectral analysis for graph signals and to develop the concept of the graph Fourier transform to perform frequency analysis of temporal and

spatial signals. This new concept extends the Fourier analysis to non-Euclidean spaces and provides new possibilities to explore the signals from a different perspective taking into account the underlying structure of the data. In this dissertation we will introduce a novel spectral analysis framework for EGM analysis based on graph signal processing. The details of this framework are given in Chapter 3. In this section we briefly recall the background works and basic concepts on graph signal processing.

Graphs and graph signals: A graph can be denoted as $\mathcal{G} = (\mathcal{V}, \mathcal{E}, \mathbf{W})$, where $\mathcal{V} = (v_1, \dots, v_K)$ is the set of K vertices, \mathcal{E} is the edge set, and \mathbf{W} is the graph adjacency matrix with entries $\mathbf{W}(i, j) = W_{i,j}$. Here, $W_{i,j} \neq 0$ represents the edge weight connecting vertices v_i and v_j and $W_{i,j} = 0$ indicates no connection between two vertices. The neighbor set of vertex v_i is denoted as \mathcal{N}_i . A graph is directed if the edges represent a direction and is undirected if there is no orientation of all edges. A graph signal is a set of values over the vertices, i.e., it is a mapping from the vertex set to the set of real numbers, $y: \mathcal{V} \rightarrow \mathbb{R}$. In this dissertation, we only consider connected and undirected graphs without self-loops. In these graphs, the weight of the edge connecting vertices v_i and v_j always satisfies that $W_{i,j} = W_{j,i} \geq 0$. The graph Laplacian matrix is defined as $\mathbf{L} = \mathbf{D} - \mathbf{W}$, where \mathbf{D} is the diagonal degree matrix with $D_{i,i} = \sum_{j=1}^K W_{i,j}$. The Laplacian is a positive semidefinite matrix i.e. the eigenvalues of the Laplacian are non negative. Figure 2.7 shows an example of an undirected graph. The adjacency matrix \mathbf{W} and the degree matrix \mathbf{D} of this graph are,

$$\mathbf{W} = \begin{bmatrix} 0 & 1 & 0 & 0 & 1 \\ 1 & 0 & 1 & 0 & 1 \\ 0 & 1 & 0 & 1 & 0 \\ 0 & 0 & 1 & 0 & 1 \\ 1 & 1 & 0 & 1 & 0 \end{bmatrix} \quad \text{and} \quad \mathbf{D} = \begin{bmatrix} 2 & 0 & 0 & 0 & 0 \\ 0 & 3 & 0 & 0 & 0 \\ 0 & 0 & 2 & 0 & 0 \\ 0 & 0 & 0 & 2 & 0 \\ 0 & 0 & 0 & 0 & 3 \end{bmatrix}, \quad (2.1)$$

respectively, and the Laplacian matrix \mathbf{L} of this graph is then given by

$$\mathbf{L} = \begin{bmatrix} 2 & -1 & 0 & 0 & -1 \\ -1 & 3 & -1 & 0 & -1 \\ 0 & -1 & 2 & -1 & 0 \\ 0 & 0 & -1 & 2 & -1 \\ -1 & -1 & 0 & -1 & 3 \end{bmatrix}. \quad (2.2)$$

Graph construction: The graph structure will affect the results of spectral analysis of graph signals. To build a graph, we can either connect the vertices based on the physical distance between the vertices v_i and v_j or learn the topology of the graph from a data stream $\mathbf{y}_1, \dots, \mathbf{y}_t$. The former explains the node dependencies directly based on their physical structure, which is natural but ignores the hidden dependencies. Whereas the latter tries to capture the underlying structure of the data but sometimes may lack the sufficient training data and the meaningful interpretations of the connections between the vertices.

Signal variation over a graph: Given a graph $\mathcal{G} = (\mathcal{V}, \mathcal{E}, \mathbf{W})$, the variation of the signal \mathbf{y} over the graph with respect to the edge $e_{i,j} = (v_i, v_j)$ at the vertex v_i is defined as

$$\left. \frac{\mathbf{y}}{e_{i,j}} \right|_{v_i} = \sqrt{W_{i,j}}(y_i - y_j), \quad (2.3)$$

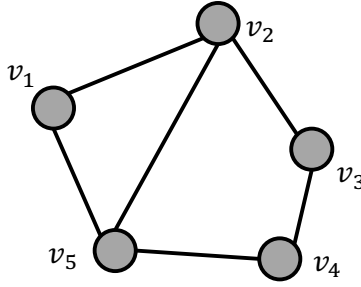


Figure 2.7: Undirected graph.

which calculates the weighted difference of the signals y_i and y_j at the connected vertices v_i and v_j , taking the square root of the edge weight, i.e., $\sqrt{W_{i,j}}$ as the weight. Then the graph gradient of the signal \mathbf{y} (stacking all partial derivatives of \mathbf{y}) at vertex v_i is given by

$$\nabla_{v_i} \mathbf{y} = \left\{ \frac{\mathbf{y}}{e_{i,j} |_{v_i}} \right\}_{e_{i,j} \in \mathcal{E}}. \quad (2.4)$$

The l_2 -norm of (2.4) is often used to measure the variation of a graph signal \mathbf{y} at vertex v_i as

$$\|\nabla_{v_i} \mathbf{y}\|_2 = \left(\sum_{v_j \in \mathcal{N}_i} W_{i,j} (y_i - y_j)^2 \right)^{\frac{1}{2}}. \quad (2.5)$$

If $\|\nabla_{v_i} \mathbf{y}\|_2$ is small, the graph signal is said to be smooth in the neighborhood of v_i . For a constant graph signal, it has $\|\nabla_{v_i} \mathbf{y}\|_2 = 0$ for all $v_i \in \mathcal{V}$. If $\|\nabla_{v_i} \mathbf{y}\|_2 > \|\nabla_{v_j} \mathbf{y}\|_2$, it is said that the signal has a higher variation at vertex v_i than at v_j . Figure 2.8 shows examples of graphs with different variation. The variation of the graphs increases from left to right in Figure 2.8 and the variation of the constant graph in Figure 2.8(a) is equal to zero. The concept of signal variation over a graph further leads to the concept of the graph Fourier transform and motivates the development of the harmonic analysis for graph signals.

Graph Fourier transform: While the classical Fourier transform expands the temporal signal onto the basis of complex exponentials, the graph Fourier transform expands the graph signal onto the basis spanned by the eigenvectors of the graph Laplacian. Since the graph Laplacian \mathbf{L} is symmetric and positive semidefinite, it accepts the eigenvalue decomposition

$$\mathbf{L} = \mathbf{U} \mathbf{\Lambda} \mathbf{U}^H \quad (2.6)$$

where $\mathbf{U} = [\mathbf{u}_0, \mathbf{u}_1, \dots, \mathbf{u}_{K-1}]$ is the set of orthonormal eigenvectors, $\mathbf{\Lambda}$ is the diagonal matrix of eigenvalues, and $(\cdot)^H$ is the Hermitian operator. The eigenvalues are sorted in increasing order $0 = \lambda_0 < \lambda_1 \leq \dots \leq \lambda_{K-1}$. The graph Fourier transform (GFT) of the graph signal \mathbf{y} with respect to Laplacian \mathbf{L} is

$$\tilde{\mathbf{y}} = \mathbf{U}^H \mathbf{y} \quad (2.7)$$

rameters, which brings difficulties to identify the parameters of interest in the model. Therefore, there is a trade-off between the accuracy of these models and the computational complexity of model parameter estimation. For readers who are interested in the progress of cardiac tissue electrophysiological models, we refer to the review in [39]. In the following we will introduce the electrophysiological models (that are most related to this dissertation) from the more complex to the more simplified, but accurate enough, versions. The derivation of the electrogram models in Section 2.6.2 and Section 2.6.3 follows the steps in the PhD thesis of B. Abdi [40].

2.6.1. BIDOMAIN/MONODOMAIN MODEL OF ACTION POTENTIAL PROPAGATION

The bidomain model is a mathematical representation of the action potential propagation in cardiac tissue. In this model, cardiac tissue is represented as a syncytium composed of the two domains separated by the cell membrane, including the intracellular domain and the extracellular domain. These two domains respectively represent the space inside the cells and the region between them. Although action potential propagation is a discrete process at the cellular scale due to the delay caused by the gap junctions between cells, it is assumed to be continuous in both domains.

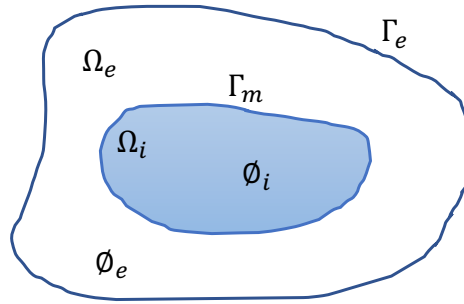


Figure 2.9: The bidomain model comprises an intracellular domain Ω_i , a cell membrane Γ_m , and an extracellular domain Ω_e . The domain boundary is denoted as Γ_e .

The bidomain model is built based on the current flow, the distribution of electrical potential and the conservation of charge and current [39]. The bidomain model at the cell scale and the associated notations are illustrated in Figure 2.9. The ions in the intracellular space and the extracellular space have a large difference in concentration, which causes diffusion of ions from high to low concentrations. The charged ions accumulate on the cell membrane due to its capacitance. These charged ions set up an electric field across and internal to the cell membrane, which in turn exerts forces on all charged ions lying within the membrane. Therefore the ion flow within or across the membrane are caused by both the forces of diffusion and the electric field space. Figure 2.10 gives an example that illustrates the ion flow due to the concentration differences and the electric field. For all excitable cells, the concentration of intracellular potassium greatly exceeds the concentration of extracellular potassium. In contrast to potassium, the extracellular sodium and chloride concentrations greatly exceed the intracellular concentrations

of sodium and chloride. Different concentrations of electric charge on the two sides of a cell membrane will produce an electric field across the membrane, which can be detected by measuring the voltage across the membrane. The potential difference between the inside surface and the outside surface of the membrane of an excitable cell is called the *transmembrane potential*. Let $\phi_i(\mathbf{x}, t)$ and $\phi_e(\mathbf{x}, t)$ represent the electrical potential in the intracellular and extracellular spaces at location \mathbf{x} at time t , respectively, then the transmembrane potential is defined as [6]

$$V_{tm}(\mathbf{x}, t) = \phi_i(\mathbf{x}, t) - \phi_e(\mathbf{x}, t). \tag{2.9}$$

In the following, we drop \mathbf{x} and t if it is clear from context. The -90 millivolts measured across the membrane may be referred to as the "resting potential" for the membrane. Since the cell membrane has a resistance, there will be a transmembrane current. Let I_{tm} be the transmembrane current. Based on the definition, this current is considered to have a positive sign when it flows across the cell membrane in the direction from the intracellular space to the extracellular space [6].

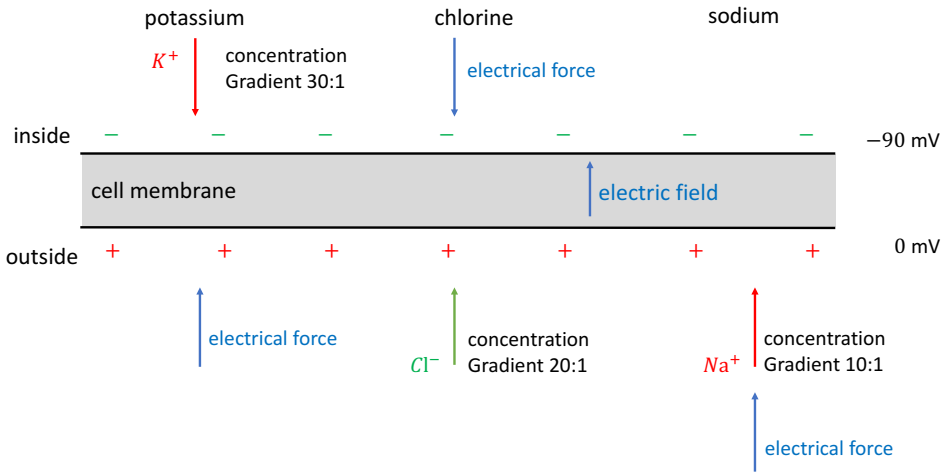


Figure 2.10: Example of ion flow due to concentration differences and electric field. Ions move across the cell membrane because of different concentration on either side of the membrane and the electrical force.

If the electric potential is known at every point in a region of space, the electric field can be derived from the potential. In the bidomain model, the electric field is assumed to be a static field at each instant of time even under normal time-varying conditions, which is known as the *quasi-static* assumption [6]. Based on this assumption, the electrical fields in the intracellular and extracellular spaces can be given by the negative of the gradient of the electric potentials as

$$\begin{cases} \mathbf{e}_i = -\nabla\phi_i \\ \mathbf{e}_e = -\nabla\phi_e, \end{cases} \tag{2.10}$$

where \mathbf{e}_i and \mathbf{e}_e are the electrical fields in the intracellular and extracellular spaces, respectively, and ∇ is the gradient. The gradient ∇ is an important operator in electrophys-

iology since the negative of the gradient of the electrical potential is normally proportional to the strength of the associated electrical current [6]. The direction of the electric field is defined as the direction that in which the potential decreases most rapidly and the magnitude is the change in potential across a small distance in the indicated direction divided by that distance.

2

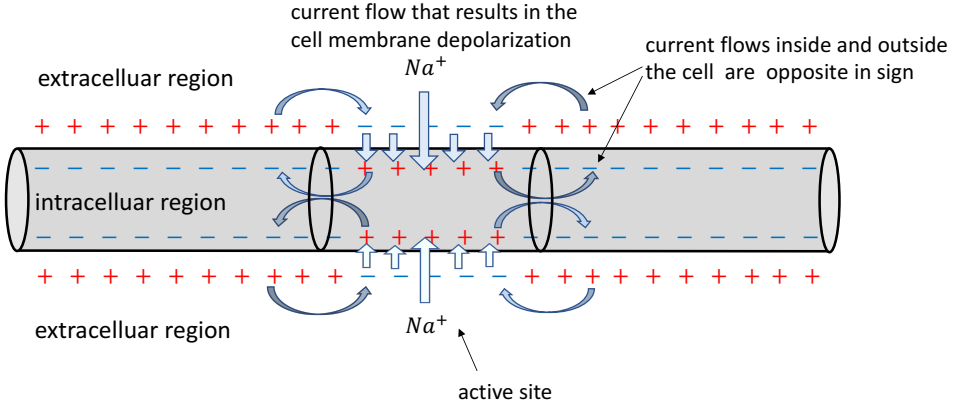


Figure 2.11: Example of current flow within and across the cell membrane.

The force exerted by the electric field results in the flow of charge, i.e. current. Figure 2.11 shows an example of current flow within and across the cell membrane. Current density is the amount of charge per unit time that flows through a unit area. The magnitude of a current density vector \mathbf{j} is the electric current density, and direction of \mathbf{j} is the same as the motion of the positive charges. Furthermore, biological materials have resistive properties. The *resistivity* property of an inhomogeneous biological material like the human heart is a function of position. In the analysis of many biological situations, it is more convenient to use *conductivity* instead of resistivity, which is simply the reciprocal of resistivity. Based on Ohm's law and Eq. (2.10), the current density for the intracellular space and the extracellular space can be obtained by [39]

$$\begin{cases} \mathbf{j}_i = \Sigma_i \mathbf{e}_i = -\Sigma_i \nabla \phi_i \\ \mathbf{j}_e = \Sigma_e \mathbf{e}_e = -\Sigma_e \nabla \phi_e, \end{cases} \quad (2.11)$$

where \mathbf{j}_i and \mathbf{j}_e are the current densities of the electrical field \mathbf{e}_i and \mathbf{e}_e in the intracellular and extracellular spaces, respectively, and Σ_i and Σ_e represents the intracellular and extracellular conductivity tensors, respectively. Figure 2.12(a) depicts a general tensor in 3D space. In matrix form, the relation $\mathbf{j} = \Sigma \mathbf{e}$ can be given by:

$$\begin{bmatrix} j_x \\ j_y \\ j_z \end{bmatrix} = \begin{bmatrix} \sigma_{xx} & \sigma_{xy} & \sigma_{xz} \\ \sigma_{yx} & \sigma_{yy} & \sigma_{yz} \\ \sigma_{zx} & \sigma_{zy} & \sigma_{zz} \end{bmatrix} \begin{bmatrix} e_x \\ e_y \\ e_z \end{bmatrix} \quad (2.12)$$

A diffusion tensor can be expressed as $\Sigma = A \text{Diag}(\lambda) A^T$, where $A = [\mathbf{a}_1, \mathbf{a}_2, \mathbf{a}_3]$ represents the eigenvectors, $\lambda = [\lambda_1, \lambda_2, \lambda_3]^T$ with its elements the eigenvalues of Σ and

$\text{Diag}(\cdot)$ represents an operator which produces a square matrix with the elements on the main diagonal from a given vector and all the other elements zero. The tensor can be represented as an ellipsoid, as shown in Figure 2.12(b). The radii of the ellipsoid (eigenvalues) represent the amount of diffusion in each of the main directions (eigenvectors) [41].

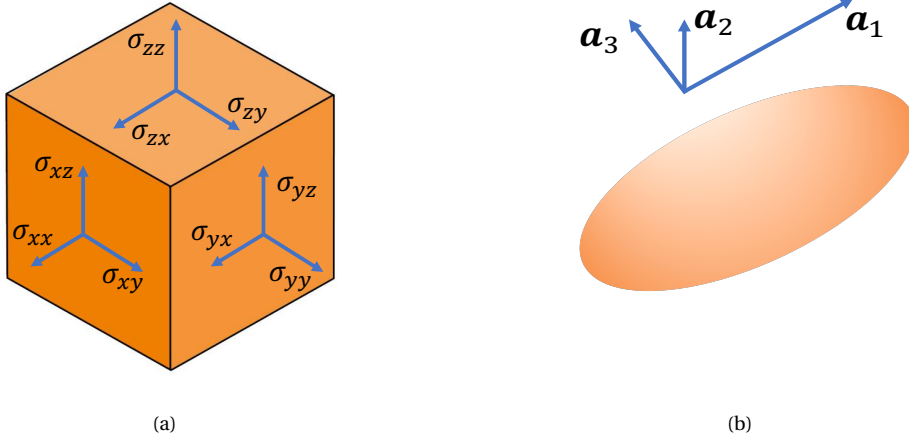


Figure 2.12: Illustration of a diffusion tensor [41]. (a) A general tensor in 3D space. (b) A tensor shown as an ellipsoid.

As the current density in the intracellular domain and the extracellular domain is equal in magnitude, but with opposite sign [6], we then have the following equations:

$$-\nabla \cdot \mathbf{j}_i = \nabla \cdot \mathbf{j}_e = S_\nu I_{\text{tm}} \quad (2.13)$$

where S_ν is the membrane surface area to volume ratio and I_{tm} is the transmembrane current per unit area that accounts for the spatial evolution (diffusion) of the transmembrane potential. Combining Eqs. (2.11) and (2.13), we obtain

$$\begin{cases} \nabla \cdot (\boldsymbol{\Sigma}_i \nabla \phi_i) = S_\nu I_{\text{tm}} \\ \nabla \cdot (\boldsymbol{\Sigma}_e \nabla \phi_e) = -S_\nu I_{\text{tm}}. \end{cases} \quad (2.14)$$

The transmembrane current I_{tm} can be modelled as a function of three currents, including the capacitive current through the membrane given by $I_C = C \frac{\partial V_{\text{tm}}}{\partial t}$ with C the total membrane capacitance, the total ionic current I_{ion} corresponding to the ions moving across the cell membrane, and also the external stimulus current I_{st} (if it exists) as [6]

$$I_{\text{tm}} = C \frac{\partial V_{\text{tm}}}{\partial t} + I_{\text{ion}} - I_{\text{st}}. \quad (2.15)$$

Combining Eqs. (2.14), (2.15), and (2.9), the bidomain model for describing the elec-

trical potential propagation is obtained as [39]

$$\begin{cases} \nabla \cdot \boldsymbol{\Sigma}_i (\nabla V_{tm} + \nabla \phi_e) = S_v (C \frac{\partial V_{tm}}{\partial t} + I_{ion} - I_{st}) \\ \nabla \cdot ((\boldsymbol{\Sigma}_i + \boldsymbol{\Sigma}_e) \nabla \phi_e) = -\nabla \cdot (\boldsymbol{\Sigma}_i \nabla V_{tm}). \end{cases} \quad (2.16)$$

From Eq. (2.16) we see that the bidomain model builds a bridge between the transmembrane potential V_{tm} (usually recorded by equipment) and the important physiological parameters such as $\boldsymbol{\Sigma}_i$ and $\boldsymbol{\Sigma}_e$ that are related to the propagation of the electrical wave in the tissue.

Boundary conditions are needed to solve the model. In the classical Neuman (no-flux) boundary conditions, the extracellular space is bounded and there is no electric current flowing from the extracellular space to adjacent spaces. For the bidomain model, the conditions are formulated as [39]

$$\begin{cases} \mathbf{n} \cdot (\boldsymbol{\Sigma}_i \nabla \phi_i) = \mathbf{n} \cdot (\boldsymbol{\Sigma}_i \nabla (V_{tm} \phi_e)) = 0 \\ \mathbf{n} \cdot (\boldsymbol{\Sigma}_e \nabla \phi_e) = 0, \end{cases} \quad (2.17)$$

where \mathbf{n} is a vector that represents the outward unit normal to the boundary.

If the anisotropy of the intracellular domain and the extracellular domain is assumed to be equal, then the bidomain model of the cardiac tissue can be simplified into the monodomain model. In this case, the conductivity in the extracellular domain is proportional to the conductivity in the intracellular domain. This can be expressed as:

$$\boldsymbol{\Sigma}_e = \beta \boldsymbol{\Sigma}_i. \quad (2.18)$$

where β represents the ratio between the intracellular conductivity and the extracellular conductivity.

Let $\boldsymbol{\Sigma} = \frac{\beta}{1+\beta} \boldsymbol{\Sigma}_i$. Combining it with Eqs. (2.16) and (2.18), the monodomain model is obtained as [39]

$$C \frac{\partial V_{tm}}{\partial t} = S_v^{-1} \nabla \cdot \boldsymbol{\Sigma} \nabla V_{tm} + I_{ion} - I_{st}. \quad (2.19)$$

In this model, the transmembrane current per unit area is given by

$$I_{tm} = S_v^{-1} \nabla \cdot \boldsymbol{\Sigma} \nabla V_{tm}. \quad (2.20)$$

For the monodomain model, the no-flux boundary condition becomes

$$\mathbf{n} \cdot (\boldsymbol{\Sigma} \nabla V_{tm}) = 0. \quad (2.21)$$

While the bidomain model contains two partial differential equations, the monodomain model is just a single partial differential equation and therefore it is easier to obtain the numerical solutions with the monodomain model. Although the bidomain model is more detailed, the monodomain model can still be a good approximation for its bidomain counterpart, even if the equal anisotropy assumption does not hold [42–44]. In the following, we are going to introduce the electrogram models based on the monodomain assumption.

2.6.2. ELECTROGRAM MODEL

In the high resolution mapping approach, a microelectrode array is used to measure the redextracellular potentials of atrial tissue. The measurements recorded from the epicardial sites of the atrial tissue are called atrial epicardial electrograms (EGMs). An EGM is the product of a highly complex network of many neighbouring cells under an electrode, representing the changes in the transmembrane potentials of the cells. By using a current source approximation for a large volume conductor, the atrial electrogram can be related to the transmembrane current I_{tm} through the model [45]

$$y_m(t) = \frac{1}{4\pi\sigma_e} \int \frac{I_{tm}(\mathbf{x}, t)}{\|\mathbf{p} - \mathbf{x}\|} d\mathbf{x}, \quad (2.22)$$

where $y_m(t)$ represents the electrogram recorded at the m th electrode at location \mathbf{p} , $I_{tm}(\mathbf{x}, t)$ represents the transmembrane current per unit area at location \mathbf{x} , and σ_e is the constant extracellular conductivity.

The atrial electrogram model in (2.22) can be further expressed in discrete form for computational purpose. We assume the tissue is two-dimensional and is discretized into N regular Δl -by- Δl elements to model N cell (groups). Let \mathbf{x}_n denote the position of the n th element with the area $a = (\Delta l)^2$. Considering M electrodes indexed by $m \in \{1, 2, \dots, M\}$ that are positioned on the atrial area and taking into account the distance between the electrode and the tissue denoted as z_0 , the space-discretized representation of the electrogram of the m th electrode, denoted as $\phi_m(t)$, is given by [46]

$$y_m(t) = \frac{1}{4\pi\sigma_e} \sum_{n=1}^N \frac{I_{tm}(\mathbf{x}_n, t)}{r_{m,n}} a, \quad (2.23)$$

with

$$r_{m,n} = \sqrt{\|\mathbf{p}_m - \mathbf{x}_n\|^2 + z_0^2} \quad (2.24)$$

representing the distance between the electrode with index m at location \mathbf{p}_m and the cell with index n . For the two-dimensional tissue, the conductivity tensor at the n th cell position is given by

$$\boldsymbol{\Sigma}_n = \begin{bmatrix} \sigma_{xx,n} & \sigma_{xy,n} \\ \sigma_{yx,n} & \sigma_{yy,n} \end{bmatrix}. \quad (2.25)$$

The computation of the transmembrane current per cell can be realized by using the space-discretized expression of Eq. (2.20), which is [46]

$$\begin{aligned} I_{tm}(\mathbf{x}_n, t) &= S_v^{-1} \nabla \cdot \boldsymbol{\Sigma}_n \nabla v_n \\ &= S_v^{-1} \left[\frac{\partial}{\partial x} \left(\sigma_{xx,n} \frac{\partial v_n}{\partial x} \right) + \frac{\partial}{\partial x} \left(\sigma_{xy,n} \frac{\partial v_n}{\partial y} \right) \right. \\ &\quad \left. + \frac{\partial}{\partial y} \left(\sigma_{yx,n} \frac{\partial v_n}{\partial x} \right) + \frac{\partial}{\partial y} \left(\sigma_{yy,n} \frac{\partial v_n}{\partial y} \right) \right], \end{aligned} \quad (2.26)$$

where v_n is the transmembrane potential of the n th cell, $\sigma_{xx,n}$, $\sigma_{yy,n}$, $\sigma_{xy,n}$ and $\sigma_{yx,n}$ are the conductivity of the cells in the x -direction, the y -direction, and the two diagonal directions, respectively.

let $\mathbf{r}_m = \left[\frac{1}{r_{m,0}}, \frac{1}{r_{m,1}}, \dots, \frac{1}{r_{m,N-1}} \right]^T$ collecting the reciprocals of the distances between the m th electrodes and all the cells, and stacking all the cell potentials in a vector $\mathbf{v}(t) = [v_0(t), v_1(t), \dots, v_{N-1}(t)]^T$, then the atrial EGM at the m th electrode can be modeled as [46]

$$y_m(t) = \frac{aS_v^{-1}}{4\pi\sigma_e} \mathbf{r}_m^T \mathbf{D}_\sigma \mathbf{v}(t), \quad (2.27)$$

with \mathbf{D}_σ a double differentiation operator defined by [46]

$$\begin{aligned} \mathbf{D}_\sigma = & \mathbf{D}_x \text{Diag}(\boldsymbol{\sigma}_{xx}) \mathbf{D}_x + \mathbf{D}_x \text{Diag}(\boldsymbol{\sigma}_{xy}) \mathbf{D}_y \\ & + \mathbf{D}_y \text{Diag}(\boldsymbol{\sigma}_{yx}) \mathbf{D}_x + \mathbf{D}_y \text{Diag}(\boldsymbol{\sigma}_{yy}) \mathbf{D}_y. \end{aligned} \quad (2.28)$$

Here, \mathbf{D}_x and \mathbf{D}_y are the first derivative operators. The conductivity vectors $\boldsymbol{\sigma}_{xx}$, $\boldsymbol{\sigma}_{yy}$, $\boldsymbol{\sigma}_{xy}$ and $\boldsymbol{\sigma}_{yx}$ stack the conductivity of all cells in the x -direction, the y -direction, and the two diagonal directions, respectively. For example, $\boldsymbol{\sigma}_{xx} = [\sigma_{xx,0}, \sigma_{xx,1}, \dots, \sigma_{xx,N-1}]^T$. If the tissue is homogeneous and isotropic, \mathbf{D}_σ is a scaled Laplacian operator.

Let $Q = \frac{aS_v^{-1}}{4\pi\sigma_e}$. Eq. (2.27) can then be simplified as

$$y_m(t) = Q \mathbf{r}_m^T \mathbf{D}_\sigma \mathbf{v}(t). \quad (2.29)$$

2.6.3. IMPULSE RESPONSE MODEL

The calculation of the transmembrane current is intensive when based on the models in Eqs. (2.20) and (2.26), which govern the electrical wave propagation in the tissue. It is difficult to use these models to solve inverse problems to estimate the tissue parameters of interest, which are essential in understanding the mechanisms underlying cardiac diseases like AF. Therefore, the work in [46] proposed a simplified impulse response model for the atrial electrograms such that signal processing approaches can easily be applied to estimate the model tissue parameters. It is based on the assumption that all cells produce almost the same stereotype action potential once activated. Then the action potential of the cell with index n , which is denoted as $v_n(t)$, can be regarded as a delayed version of the action potential of the reference cell.

Taking the cell with action potential $v_0(t)$ as reference, the action potential of the cell with index n is modelled as [46]

$$v_n(t) = v_0(t - \tau_n) = \delta(t - \tau_n) * v_0(t), \quad (2.30)$$

where $*$ is the convolution operator, $\delta(\cdot)$ is the Dirac delta function, and τ_n is the local activation time of the n th cell with respect to the reference cell. With τ_0 for the reference cell set to $\tau_0 = 0$, the action potential of all cells can then be calculated as

$$\mathbf{v}(t) = \boldsymbol{\delta}_\tau(t) * v_0(t), \quad (2.31)$$

where

$$\boldsymbol{\delta}_\tau(t) = [\delta(t - \tau_0), \delta(t - \tau_1), \dots, \delta(t - \tau_{N-1})]^T. \quad (2.32)$$

Therefore, the atrial EGM measured by the m th electrode [ref. (2.29)] denoted as $y_m(t)$ can be remodelled as an impulse response model as

$$y_m(t) = Q \mathbf{r}_m^T \mathbf{D}_\sigma \boldsymbol{\delta}_\tau(t) * v_0(t). \quad (2.33)$$

This can be further simplified as

$$y_m(t) = a_m(t) * v_0(t), \quad (2.34)$$

with $a_m(t) = Q\mathbf{r}_m^T\mathbf{D}_G\delta_\tau(t)$ the impulse response from all cells to the electrode of index m .

2.6.4. PARAMETERS AND ESTIMATION

It has been shown that the development and the progression of cardiac arrhythmias are related to impaired conduction in cardiac tissue [47–49]. As such, EGM model parameters such as the conductivity, the activation time, and the anisotropy ratio are useful to identify the arrhythmogenic substrate that causes abnormal propagation of the electrical waves in the atrial tissue. Estimating these parameters from the electrophysiological models is therefore important in the study of AF. In this dissertation, we are interested in the estimation of the following parameters:

1) Conductivity: Conductivity is the ability of the cells to propagate the stimuli to their neighbours. It is one of the important properties of cardiac cells, which allows the cardiac cells to conduct and generate electricity. Conduction velocity, which is defined as the distance traveled by the depolarization wavefront in a unit of time, is usually measured in medical studies by cardiologists. However, conduction velocity is determined by many factors, one of which is conductivity [39]. Both pathologic origin and non-pathologic origin can cause the change of this parameter; even the pathological causes might not be local and might originate from a different atrial area [46]. Local curvature can influence the conduction velocity and concave wavefronts propagate faster than convex wavefronts without having any pathological causes [46, 50]. Investigating the pathology of cardiac tissue using conductivity is more reliable since it is a direct tissue property, while conduction velocity only indirectly is an observation from (various) tissue properties. In this dissertation we therefore aim to estimate the conductivity parameter from the epicardial electrograms. Measuring conductivities experimentally in tissue is highly challenging, since conductivity properties depend on the volume, shape, and orientation of cardiac cells, blood flow in the vasculature, gap junctions, and the ionic composition of intracellular and extracellular spaces, which are difficult to measure and vary across tissue regions [51]. Estimating conductivities based on electrophysiological models from the computational point of view is also complicated. Firstly, the measurements must be made taking into account very small electrode spacings. This comes with considerable technical challenges, both in constructing the electrode array and in deploying it. Secondly, approaches for estimating the conductivities from the high resolution measurements must be designed. This requires a proper mathematical model for the measurements and an efficient algorithm to solve the inverse problem. This problem is ill-posed due to the large number of unknown parameters in the model. Different inversion techniques are then required to retrieve the parameters of interest from the electrophysiological models [52]. While the bidomain model requires both the intracellular and extracellular conductivity parameters to model the electrical activity in the tissue, the monodomain model simplifies the parameters by assuming that the extracellular conductivity is proportional to the intracellular conductivity, as introduced in Section 2.6.1. In this dissertation we extract the conductivity parameters from the atrial

electrograms based on the monodomain model.

2) Anisotropy ratio. Myocytes are highly aligned along their principal axis and organize into fibres. Longitudinal propagation along the principal axis of a fibre is faster than transverse propagation, which results in the anisotropic propagation of the action potential [39]. In general, both the intracellular and extracellular conductivities are anisotropic. Anisotropic propagation in the EGM model is characterised by two principal values of conductivity: a longitudinal conductivity parallel to fibres and a transverse conductivity orthogonal to fibres. In this study, the anisotropy ratio defined as the ratio of the longitudinal conductivity to the transverse conductivity is another important parameter to be estimated.

3) Local activation time. Analysis of cardiac conduction typically requires the identification of the cell activation time, which needs to be estimated from the electrograms recorded by electrodes placed closely or in direct contact with cardiac tissue. The widely accepted definition of the activation time of an action potential is the moment of maximum change in the transmembrane voltage of a cell [47]. This maximum change is related to the peak conductance of the sodium channel in the initialization of the depolarization of cardiac cells when they are activated. Since an electrogram is a summation of electrical activity of cell groups surrounding the electrode location, it may have a complex morphology due to asynchronous activation of myocardial cells or can be corrupted by noises. The accurate identification of local activation time can therefore sometimes be difficult. A number of algorithms has been proposed to overcome this challenges as reviewed in [47], including morphological approaches looking at areas under the modulus of the electrogram instead of a single data point in the signal; time-delay cross-correlation based approaches that are based on the activation time delays between nearby recordings [53]; deconvolution that regards the generation of an electrogram as a convolution of transmembrane potentials and estimates parameters of forward models to fit the observed electrograms by solving a constrained minimization problem [54] and other methods. In this dissertation we develop a deconvolution method to estimate the local activation time parameters, i.e., τ_n in Eq. (2.30).

2.6.5. ESTIMATING PARAMETERS USING CONFIRMATORY FACTOR ANALYSIS

Electrophysiological models are rather detailed and include a large number of free parameters that brings the difficulties to identify the parameters of interest. Although the simpler impulse response model has recently been proposed to reduce the computational complexity (as introduced in Section 2.6.3), it does not explicitly make use of the spatial structure of the multi-electrode data.

In [55], we further exploited the cross power spectral density matrix (CPSDM) model of the multi-electrode epicardial electrograms (EGMs), which enables us to utilize the spatial correlations among the measurements to estimate the conductivity and the anisotropy ratio parameters. An efficient method called confirmatory factor analysis (CFA) was applied to the CPSDM model to estimate the target parameters. Estimating parameters from the model is ill-posed due to the large number of unknown parameters in the model. To solve the problem, we need to verify whether the solution for estimating the target unknowns can be obtained with the given amount of data. This was achieved by analyzing the identifiability conditions in the CFA problem. Based on the fact that the

conductivity and the anisotropy ratio parameters are shared among multiple frequencies, we further proposed the simultaneous CFA across multiple temporal frequencies to estimate these parameters simultaneously, which can satisfy the identifiability conditions easier. We will introduce this work in Chapter 4.

Although the work in [55] can jointly estimate a subset of target parameters from electrogram measurements, it was limited to the use of a single heart beat and could only estimate the conductivity and the anisotropy ratio parameters. In Chapter 5, we further extend this method to jointly estimate the conductivity, the anisotropy ratio, as well as the activation time per cell using multiple heart beats and multiple frequencies from atrial EGMs. With the reasonable assumptions that the conductivity and the anisotropy parameters are constant across different frequencies and different heart beats, we estimate these parameters using multiple frequencies and multiple heart beats simultaneously to easier satisfy the identifiability conditions in the CFA problem.

REFERENCES

- [1] P. W. Macfarlane, A. van Oosterom, O. Pahlm, et al., *Comprehensive electrocardiology*, Springer Science & Business Media, 2010.
- [2] M. Varela, R. Morgan, A. Theron, et al., “Novel mri technique enables non-invasive measurement of atrial wall thickness,” *IEEE Transactions on Medical Imaging*, vol. 36, no. 8, pp. 1607–1614, 2017.
- [3] Perez A. E. A., D. G. Whittaker, A. P. Benson, and M. A. Colman, “Effects of heart rate and ventricular wall thickness on non-invasive mapping: an in silico study,” *Frontiers in Physiology*, vol. 10, pp. 308, 2019.
- [4] Wikipedia, “Heart — Wikipedia, the free encyclopedia,” <http://en.wikipedia.org/w/index.php?title=Heart&oldid=990279132>, 2021, [Online; accessed 22-October-2021].
- [5] J. E. Hall and M. E. Hall, *Guyton and Hall textbook of medical physiology e-Book*, Elsevier Health Sciences, 2020.
- [6] R. Plonsey and R. C. Barr, *Bioelectricity: a quantitative approach*, Springer Science & Business Media, 2007.
- [7] A. G. Kléber and Y. Rudy, “Basic mechanisms of cardiac impulse propagation and associated arrhythmias,” *Physiological Reviews*, 2004.
- [8] R. Klabunde, *Cardiovascular physiology concepts*, Lippincott Williams & Wilkins, 2011.
- [9] C. T. January, L. S. Wann, J. S. Alpert, et al., “2014 AHA/ACC/HRS guideline for the management of patients with atrial fibrillation: a report of the American College of Cardiology/American Heart Association Task Force on Practice Guidelines and the Heart Rhythm Society,” *Journal of the American College of Cardiology*, vol. 64, no. 21, pp. e1–e76, 2014.

- [10] R. G Hart and J. L. Halperin, "Atrial fibrillation and stroke: concepts and controversies," *Stroke*, vol. 32, no. 3, pp. 803–808, 2001.
- [11] C. H. Roney, A. L. Wit, and N. S. Peters, "Challenges associated with interpreting mechanisms of af," *Arrhythmia & Electrophysiology Review*, vol. 8, no. 4, pp. 273–284, 2019.
- [12] S. Nattel and D. Dobrev, "Controversies about atrial fibrillation mechanisms: aiming for order in chaos and whether it matters," *Circulation Research*, vol. 120, no. 9, pp. 1396–1398, 2017.
- [13] H. Calkins, K. H. Kuck, R. Cappato, et al., "2012 HR/EHRA/ECAS expert consensus statement on catheter and surgical ablation of atrial fibrillation: recommendations for patient selection, procedural techniques, patient management and follow-up, definitions, endpoints, and research trial design: a report of the Heart Rhythm Society (HRS) Task Force on Catheter and Surgical Ablation of Atrial Fibrillation," *Europace*, vol. 14, no. 4, pp. 528–606, 2012.
- [14] G. Hindricks, T. Potpara, N. Dagres, et al., "2020 ESC guidelines for the diagnosis and management of atrial fibrillation developed in collaboration with the european association of cardio-thoracic surgery (EACTS)," *European Heart Journal*, vol. 42, no. 5, pp. 373–498, 2020.
- [15] S. S. Chugh, R. Havmoeller, K. Narayanan, et al., "Worldwide epidemiology of atrial fibrillation: a global burden of disease 2010 study," *Circulation*, vol. 129, no. 8, pp. 837–847, 2014.
- [16] A. Yaksh, L. J. M. E. van der Does, et al., "A novel intra-operative, high-resolution atrial mapping approach," *Journal of Interventional Cardiac Electrophysiology*, vol. 44, no. 3, pp. 221–225, 2015.
- [17] L. J. M. E. van der Does, A. Yaksh, C. Kik, et al., "Quest for the arrhythmogenic substrate of atrial fibrillation in patients undergoing cardiac surgery (quasar study): rationale and design," *Journal of Cardiovascular Translational Research*, vol. 9, no. 3, pp. 194–201, 2016.
- [18] E. A. H. Lanfers, D. M. S. van Marion, C. Kik, et al., "HALT & REVERSE: Hsf1 activators lower cardiomyocyt damage; towards a novel approach to REVERSE atrial fibrillation," *Journal of Translational Medicine*, vol. 13, no. 347, 2015.
- [19] T. Nitta, Y. Ishii, Y. Miyagi, et al., "Concurrent multiple left atrial focal activations with fibrillatory conduction and right atrial focal or reentrant activation as the mechanism in atrial fibrillation," *The Journal of Thoracic and Cardiovascular Surgery*, vol. 127, no. 3, pp. 770–778, 2004.
- [20] V. Barbaro, P. Bartolini, G. Calcagnini, et al., "Mapping the organization of atrial fibrillation with basket catheters, part i: Validation of a real-time algorithm," *Pacing and Clinical Electrophysiology*, vol. 24, no. 7, pp. 1082–1088, 2001.

- [21] G. Calcagnini, F. Censi, A. Michelucci, and P. Bartolini, "Descriptors of wavefront propagation," *IEEE Engineering in Medicine and Biology Magazine*, vol. 25, no. 6, pp. 71–78, 2006.
- [22] V. Barbaro, P. Bartolini, G. Calcagnini, et al., "Measure of synchronisation of right atrial depolarisation wavefronts during atrial fibrillation," *Medical and Biological Engineering and Computing*, vol. 40, no. 1, pp. 56–62, 2002.
- [23] J. Slocum, E. Byrom, L. McCarthy, et al., "Computer detection of atrioventricular dissociation from surface electrocardiograms during wide QRS complex tachycardias," *Circulation*, vol. 72, no. 5, pp. 1028–1036, 1985.
- [24] S. Petrutiu, J. Ng, G. M. Nijm, et al., "Atrial fibrillation and waveform characterization," *IEEE Engineering in Medicine and Biology Magazine*, vol. 25, no. 6, pp. 24–30, 2006.
- [25] M. Lemay, J. Vesin, A. van Oosterom, et al., "Cancellation of ventricular activity in the ECG: evaluation of novel and existing methods," *IEEE Transactions on Biomedical Engineering*, vol. 54, no. 3, pp. 542–546, 2007.
- [26] J. J. Rieta and F. Hornero, "Comparative study of methods for ventricular activity cancellation in atrial electrograms of atrial fibrillation," *Physiological Measurement*, vol. 28, no. 8, pp. 925–936, 2007.
- [27] D. Raine, P. Langley, A. Murray, et al., "Surface atrial frequency analysis in patients with atrial fibrillation: a tool for evaluating the effects of intervention," *Journal of Cardiovascular Electrophysiology*, vol. 15, no. 9, pp. 1021–1026, 2004.
- [28] J. J. Rieta, F. Castells, C. Sánchez, et al., "Atrial activity extraction for atrial fibrillation analysis using blind source separation," *IEEE Transactions on Biomedical Engineering*, vol. 51, no. 7, pp. 1176–1186, 2004.
- [29] D. I. Shuman, S. K. Narang, P. Frossard, A. Ortega, et al., "The emerging field of signal processing on graphs: extending high-dimensional data analysis to networks and other irregular domains," *IEEE Signal Processing Magazine*, vol. 30, no. 3, pp. 83–98, 2013.
- [30] A. C. Skanes, R. Mandapati, O. Berenfeld, et al., "Spatiotemporal periodicity during atrial fibrillation in the isolated sheep heart," *Circulation*, vol. 98, no. 12, pp. 1236–1248, 1998.
- [31] J. Jalife, O. Berenfeld, and M. Mansour, "Mother rotors and fibrillatory conduction: a mechanism of atrial fibrillation," *Cardiovascular Research*, vol. 54, no. 2, pp. 204–216, 2002.
- [32] P. Sanders, O. Berenfeld, M. Hocini, et al., "Spectral analysis identifies sites of high-frequency activity maintaining atrial fibrillation in humans," *Circulation*, vol. 112, no. 6, pp. 789–797, 2005.

- [33] J. Salinet, F. S. Schlindwein, P. Stafford, et al., “Propagation of meandering rotors surrounded by areas of high dominant frequency in persistent atrial fibrillation,” *Heart Rhythm*, vol. 14, no. 9, pp. 1269–1278, 2017.
- [34] F. J. Vanheusden, G. S. Chu, X. Li, et al., “Systematic differences of non-invasive dominant frequency estimation compared to invasive dominant frequency estimation in atrial fibrillation,” *Computers in Biology and Medicine*, vol. 104, pp. 299–309, 2019.
- [35] T. H. Everett, L. Kok, R. H. Vaughn, et al., “Frequency domain algorithm for quantifying atrial fibrillation organization to increase defibrillation efficacy,” *IEEE Transactions on Biomedical Engineering*, vol. 48, no. 9, pp. 969–978, 2001.
- [36] D. S. Rosenbaum and R. J. Cohen, “Frequency based measures of atrial fibrillation in man,” in *[1990] Proceedings of the twelfth annual international conference of the IEEE engineering in medicine and biology society*. IEEE, 1990, pp. 582–583.
- [37] N. Habel, P. Znojkwicz, Na. Thompson, et al., “The temporal variability of dominant frequency and complex fractionated atrial electrograms constrains the validity of sequential mapping in human atrial fibrillation,” *Heart Rhythm*, vol. 7, no. 5, pp. 586–593, 2010.
- [38] J. W. E. Jarman, T. Wong, P. Kojodjojo, et al., “Spatiotemporal behavior of high dominant frequency during paroxysmal and persistent atrial fibrillation in the human left atrium,” *Circulation: Arrhythmia and Electrophysiology*, vol. 5, no. 4, pp. 650–658, 2012.
- [39] R. H. Clayton, O. Bernus, E. M. Cherry, et al., “Models of cardiac tissue electrophysiology: progress, challenges and open questions,” *Progress in Biophysics and Molecular Biology*, vol. 104, no. 1-3, pp. 22–48, 2011.
- [40] B. Abdi, *Atrial Fibrillation Fingerprinting*, Ph.D. thesis, TU Delft, Fac. EEMCS, Delft, The Netherlands, Oct. 2021, ISBN 978-94-6184-260-0.
- [41] E. Gilboa, P. S. La Rosa, and A. Nehorai, “Estimating electrical conductivity tensors of biological tissues using microelectrode arrays,” *Annals of Biomedical Engineering*, vol. 40, no. 10, pp. 2140–2155, 2012.
- [42] M. Potse, B. Dubé, J. Richer, et al., “A comparison of monodomain and bidomain reaction-diffusion models for action potential propagation in the human heart,” *IEEE Transactions in Biomedical Engineering*, vol. 53, no. 12, pp. 2425–2435, 2006.
- [43] B. F. Nielsen, T. S. Ruud, G. T. Lines, and A. Tveito, “Optimal monodomain approximations of the bidomain equations,” *Applied Mathematics and Computation*, vol. 184, pp. 276–290, 2007.
- [44] Y. Coudière, Y. Bourgault, and M. Rioux, “Optimal monodomain approximations of the bidomain equations used in cardiac electrophysiology,” *Mathematical Models and Methods in Applied Sciences*, vol. 24, pp. 1115–1140, 2014.

- [45] N. Virag, V. Jacquemet, C. S. Henriquez, et al., "Study of atrial arrhythmias in a computer model based on magnetic resonance images of human atria," *Chaos: An Interdisciplinary Journal of Nonlinear Science*, vol. 12, no. 3, pp. 754–763, 2002.
- [46] B. Abdi, R. C. Hendriks, A.-J. van der Veen, and N. M.S. de Groot, "A compact matrix model for atrial electrograms for tissue conductivity estimation," *Computers in Biology and Medicine*, vol. 107, pp. 284–291, 2019.
- [47] C. D. Cantwell, C. H. Roney, F. S. Ng, et al., "Techniques for automated local activation time annotation and conduction velocity estimation in cardiac mapping," *Computers in Biology and Medicine*, vol. 65, pp. 229–242, 2015.
- [48] M. S. van Schie, A. Heida, Y. J. H. J. Taverne, et al., "Identification of local atrial conduction heterogeneities using high-density conduction velocity estimation," *Europace*, p. euab088, 2021.
- [49] N. Mazeh, D. E Haines, M. W. Kay, and B. J. Roth, "A simplified approach for simultaneous measurements of wavefront velocity and curvature in the heart using activation times," *Cardiovascular Engineering and Technology*, vol. 4, no. 4, pp. 520–534, 2013.
- [50] V. G. Fast and A. G. Kleber, "Role of wavefront curvature in propagation of cardiac impulse," *Cardiovascular Research*, vol. 33, no. 2, pp. 258–271, 1997.
- [51] J. G. Stinstra, B. Hopfenfeld, and R. S MacLeod, "On the passive cardiac conductivity," *Annals of Biomedical Engineering*, vol. 33, no. 12, pp. 1743–1751, 2005.
- [52] M. J. Barbara and R. J. Peter, "Approaches for determining cardiac bidomain conductivity values: progress and challenges," *Medical & Biological Engineering & Computing*, vol. 58, pp. 2919–2935, 2020.
- [53] B. Kölling, B. Abdi, N. M.S. de Groot, and R. C. Hendriks, "Local activation time estimation in atrial electrograms using cross-correlation over higher-order neighbors," in *The 28th European Signal Processing Conference (EUSIPCO)*. IEEE, 2021, pp. 905–909.
- [54] B. Abdi, R. C. Hendriks, A.-J. van der Veen, and N. M.S. de Groot, "Local activation time annotation in atrial electrogram arrays using deconvolution," in *Computing in Cardiology*.
- [55] M. Sun, N. M.S. de Groot, and R. C. Hendriks, "Cardiac tissue conductivity estimation using confirmatory factor analysis," *Computers in Biology and Medicine*, vol. 135, 2021.

3

GRAPH-TIME SPECTRAL ANALYSIS FOR ATRIAL FIBRILLATION

ATRIAL fibrillation is a clinical arrhythmia with multifactorial mechanisms still unresolved. Time-frequency analysis of epicardial electrograms has been investigated to study atrial fibrillation. However, deeper understanding can be achieved by incorporating the spatial dimension. Unfortunately, the physical models describing the spatial relations of atrial fibrillation signals are complex and non-linear; hence, conventional signal processing techniques to study electrograms in the joint space, time, and frequency domain are less suitable. In this chapter, we wish to put forward a radically different approach to analyze atrial fibrillation with a higher-level model. This approach relies on graph signal processing to represent the spatial relations between epicardial electrograms. To capture the frequency content along both the time and graph domain, we propose the joint graph and short-time Fourier transform. The latter allows us to analyze the spatial variability of the electrogram temporal frequencies. With this technique, we found the spatial variation of the atrial electrograms decreases during atrial fibrillation since the high temporal frequencies of the atrial waves reduce. The proposed analysis further confirms that the ventricular activity is smoother over the atrial area compared with the atrial activity. Besides using the proposed graph-time analysis to conduct a first study on atrial fibrillation, we demonstrate its potential by applying it to the cancellation of ventricular activity from the atrial electrograms. Experimental results on simulated and real data further corroborate our findings in this atrial fibrillation study.

3.1. INTRODUCTION

Atrial fibrillation is a cardiac arrhythmia characterized by rapid and irregular atrial beating and it is correlated with stroke and sudden death [1–3]. Yet, the mechanisms underlying atrial fibrillation remain unresolved and challenging to model. To analyze the dis-

This chapter is based on the paper published as "Graph-Time Spectral Analysis for Atrial Fibrillation" by M. Sun, E. Isufi, N. M.S. de Groot, and R. C. Hendriks, *Biomedical Signal Processing and Control*, vol. 59, 2020.

ease, different signal processing methods have been applied to the non-invasive body surface electrocardiograms (ECGs), or to the invasive epicardial or endocardial electrograms [4–8]. The epicardial electrogram (EGM) is measured on the heart's surface through multiple electrodes and has a higher spatial resolution compared with ECGs. This improved resolution makes EGMs appealing to analyze atrial fibrillation over both space (heart surface) and time. The methods proposed in the current work concern EGM data.

Although different studies have analyzed electrogram data in time and frequency domain [9–13], there remain many open questions that require alternative and novel tools to investigate atrial fibrillation. Experience in signal processing suggests that incorporating the spatial dimension into the time-frequency analysis may yield improved insights on the atrial activity. However, physical models for spatial propagation are relatively complex and non-linear, rendering conventional signal processing methods less suitable for joint space, time, and frequency domain analysis [14, 15]. It is also difficult to use physical models to extract useful information, e.g., activation time or conductivity [16].

In this chapter, we suggest a novel approach to model epicardial electrograms at a higher abstraction level. This approach represents the spatial relation of different epicardial electrograms through a graph and relies on graph signal processing to investigate electrograms in the joint space, time, and frequency domain. We conduct a first study with the proposed framework to identify spectral differences between sinus rhythm (normal heart rhythm) and atrial fibrillation, and between atrial and ventricular activities. We also leveraged the proposed graph model to remove ventricular components from the raw EGM measurements.

Graph-time signal processing: Graphs are natural tools to model data living in high-dimensional and irregular domains [17]. Graph signal processing provides a harmonic analysis for signals residing on the graph vertices and has been applied to brain signal analysis, Alzheimer classification, and body motion [18–24]. However, despite showing promise, graph signal processing has not been explored for heart-related problems. The EGM signals considered in this work are (spatially) high-dimensional measurements taken from epicardial sites of the atria during open-heart surgery [25]. Graph signal processing poses itself as a valid candidate to account for the underlying mechanisms to analyze atrial fibrillation. The atrial activity during atrial fibrillation is a complicated process for which it is hard to find a good and tractable mathematical model. Graph signal processing can tackle this issue by formulating a high-level model for the atrial activity; hence, taking a step further towards exploring the atrial fibrillation behavior. The use of graphs to understand atrial fibrillation has also been considered in [26]. This work explored the association between different atrial regions through basic graph theory (e.g., graph topology, density, average degree), yet left unexplored the processing of signals on top of this graph. Instead, we here investigate EGMs through graph signal processing.

The predominant tool in graph signal processing is the graph Fourier transform; a generalization of the temporal Fourier transform that provides a frequency interpretation for graph data. Similar to the time domain, the graph frequency components characterize the signal variation, now, over the graph and have shown to be useful to study

biological activities [18–20]. However, since the EGM varies with time, it is insufficient to consider the graph Fourier transform alone as it analyzes the spatial variability for a fixed time instant. To account for the temporal variability and capture the interaction between space and time, we can consider the so-called product graphs [27]. A conceptual simpler alternative is to apply the graph Fourier transform on the data after applying the temporal Fourier transform (which tends to decorrelate the time-domain data). Since the electrogram is non-stationary, we use a joint graph and short-time Fourier transform to investigate the spatial properties of the temporal frequency content in a short-time period. Compared with the product graph method, working on the joint graph-time domain is simpler, and the analysis can be done independently per temporal frequency.

Spectral EGM analysis: We apply the graph-time spectral analysis to characterize the spectral properties of the EGMs in the graph and time domain. We first evaluate the spatial variation of the EGMs at different temporal frequencies during sinus rhythm and atrial fibrillation. During atrial fibrillation, we show the high temporal frequencies of the atrial activity reduce, leading to a decrease of the spatial variation. We also observed the spatial variation of the atrial activity is higher than the spatial variation of the ventricular activity. We used this difference in behavior to extract the atrial activity from the mixed EGM measurement.

Atrial activity extraction: Electrograms measured on the atrial sites are naturally corrupted by the ventricular activity. The capability of a method to extract the atrial activity is fundamental to promote it for atrial fibrillation studies. A common technique to extract the atrial activity is template matching such as average beat subtraction [28]. However, this simple method does not adapt to changes in the EGM morphology caused by the variations in the heart activities. To deal with this shortcoming, adaptive ventricular cancellation [29] has been proposed to extract the atrial activity. Nevertheless, its performance is unstable as it relies on a reference signal, often obtained with a reference lead. Another class of techniques using multi-lead information are the signal separation algorithms such as principal component analysis [30] and independent component analysis [31]. Results of these methods are compared in [32]. However, it is questionable whether the statistical assumptions made by these methods for ECGs (e.g. on the distribution and independence of components) still hold for epicardial data. More recently B. Adbi et al. proposed to remove the ventricular activity from the mixed electrograms based on the low-rank property of the ventricular component matrix and the sparsity of property of the ventricular component in the frequency domain [33]. Motivated by our spectral analysis of the ventricular activity, we proposed a more effective algorithm for atrial activity extraction based on graph signal smoothness. Our method captures the morphology in the heart activities and does not require the uncorrelated or independent assumption between leads. Our numerical results on both synthetic and real data confirm the potential of graph-based atrial extraction algorithm over comparative alternatives. The latter corroborate the graph-time spectral insights for atrial fibrillation.

Contribution and organization: Altogether, this chapter puts forward a radically different approach to analyze the epicardial electrograms from a higher abstraction level. This approach relies on graph signal processing and reveals features of biological and engineering interest. It also shows promise to remove interference from the atrial electrogram. More concretely, the contributions of this paper are: (i) To propose a high-level

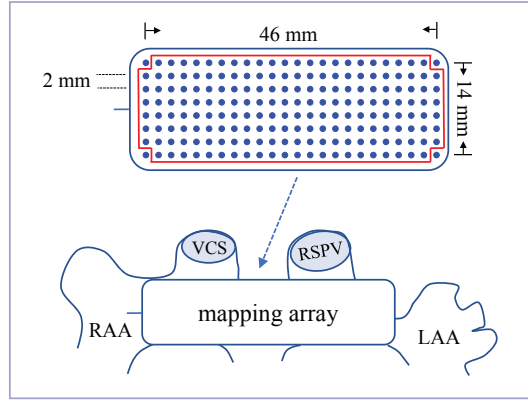


Figure 3.1: Mapping array and its placement on the Bachmann's bundle area of the atria [25]. RAA: right atrial appendage; LAA: left atrial appendage; VCS: vena cava superior; RSPV: right superior pulmonary vein.

graph signal processing model for analyzing the epicardial electrogram; (ii) To evaluate the temporal and spatial variation of epicardial electrograms with a graph-time spectral analysis framework. This helps to: (ii-a) recognize atrial fibrillation impact on the atrial activity; (ii-b) identify differences between the atrial and ventricular activities; (iii) To propose a novel and effective atrial activity extraction algorithm based on the graph-time variations of the atrial and ventricular activities.

The rest of this chapter is organized as follows. Section 3.2 describes the data used in this work. Section 3.3 introduces the basic notions of graph signal processing and the joint graph and short-time Fourier transform. Section 3.4 performs the graph-time spectral analysis under sinus rhythm and atrial fibrillation. Section 3.5 introduces the graph-based atrial activity extraction algorithm and Section 3.6 evaluates its performance on synthetic and real data. We draw the conclusions in Section 3.7.

3.2. DATABASE

As introduced in Section 2.4, we used the epicardial electrograms measured on human atria during open-heart surgery as reported in [25]. Ten patients (aged 64 ± 16 ; 20% female) are analyzed in this study. Three patients underwent surgery due to aorta ascendens dilatation and the remaining seven due to aortic valve and coronary artery disease; all patients did not have a reported history of atrial fibrillation. The atrial fibrillation was induced manually by rapid pacing in the right atrial free wall with the procedure detailed in the original publication [25]. We remark that induced atrial fibrillation has also been used to investigate the disease in [26] and [9]. For each patient, both sinus rhythm and atrial fibrillation data are recorded. Examples of the epicardial electrograms in sinus rhythm and atrial fibrillation have been shown in Section 2.4.2.

Previous research has suggested that the Bachmann's bundle area of the atria is related to the pathophysiology of atrial fibrillation [34]. However, this is still one of the less understood areas. Because of the connection with atrial fibrillation and the interesting

research aspects, we will hereinafter focus on the EGMs measured on the Bachmann's bundle. Figure 3.1 illustrates the mapping array and its placement on the Bachmann's bundle area.

3.3. THEORY

In this section, we recall the basic concepts on graph signal processing and introduce the joint graph and short-time Fourier transform.

3.3.1. GRAPH SIGNAL PROCESSING

Graphs and graph signals: Consider a network represented by an undirected graph $\mathcal{G} = (\mathcal{V}, \mathcal{E}, \mathbf{W})$, where $\mathcal{V} = (v_1, \dots, v_K)$ is the set of K vertices, \mathcal{E} is the set of edges, and \mathbf{W} is the graph adjacency matrix with entries $\mathbf{W}(i, j) = W_{i,j}$. Here, $W_{i,j} \geq 0$ represents the edge weight connecting vertices v_i and v_j and $W_{i,j} = 0$ indicates no connection between vertices. The neighbor set of vertex v_i is denoted as \mathcal{N}_i . The graph Laplacian matrix is $\mathbf{L} = \mathbf{D} - \mathbf{W}$, where \mathbf{D} is the diagonal degree matrix with $D_{i,i} = \sum_{j=1}^K W_{i,j}$.

A graph signal is a set of values over the vertices, i.e., it is a mapping from the vertex set to the set of real numbers, $y : \mathcal{V} \rightarrow \mathbb{R}$. The epicardial electrograms recorded by all electrodes in the mapping array is an example of a graph signal. Let $y_i(t)$ be the signal of vertex v_i at time t for $i = 1, \dots, K$ and $t = 0, \dots, T - 1$. The graph signal at time t is compactly represented by the $K \times 1$ vector $\mathbf{y}(t) = [y_1(t), y_2(t), \dots, y_K(t)]^T$.

The electrical activities recorded by the electrodes are related to each other and form an electrical network. We constructed a graph by considering each electrode as a vertex. There are two ways to build the edges in the graph: (i) based on the data structure, e.g., correlation; (ii) based on physical properties, e.g., distance.

To compare the sinus rhythm signal with the atrial fibrillation signal, we consider a fixed graph structure for both situations. With the illustration in Figure 3(a), the edges are determined by the electrodes position; each vertex is connected with its up to eight nearest neighbors. This expresses that an electrode (vertex) has strong similarities with the surrounding electrodes. In other words, this graph is built with the prior knowledge that under healthy conditions, neighboring vertices record a similar signal. The edge weights are based on the distance between two vertices. This is a common approach in graph signal processing when there is little prior knowledge about the signal. The weight of edge $W_{i,j}$ is

$$W_{i,j} = \left(\frac{d_{i,j}}{\alpha} \right)^{-1} \quad (3.1)$$

where $d_{i,j}$ is the distance between two connected vertices and α is a scaling parameter. We chose α as the smallest distance between two vertices to normalize the largest weight to one.

Graph Fourier transform and smoothness: The graph Laplacian matrix is symmetric, positive semidefinite, and accepts the eigenvalue decomposition

$$\mathbf{L} = \mathbf{U}\mathbf{\Lambda}\mathbf{U}^H \quad (3.2)$$

where $\mathbf{U} = [\mathbf{u}_0, \mathbf{u}_1, \dots, \mathbf{u}_{K-1}]$ is the set of orthonormal eigenvectors, $\mathbf{\Lambda}$ is the diagonal matrix of eigenvalues, and $(\cdot)^H$ is the Hermitian operator. The eigenvalues are sorted in

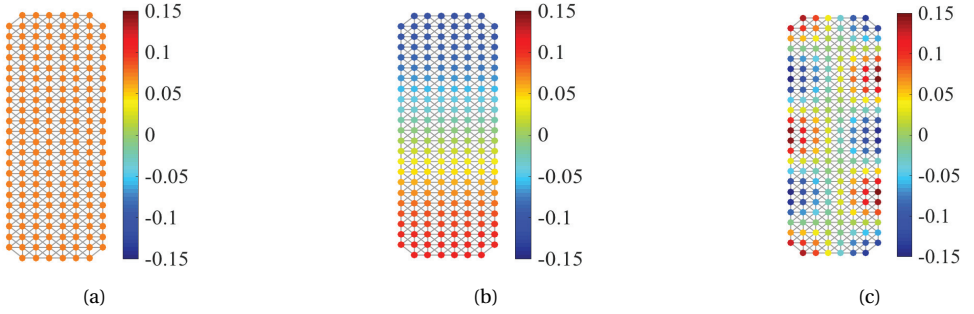


Figure 3.2: Different graph Laplacian eigenvectors of the graph. (a) $\mathbf{u}_0 = 1/\sqrt{K}\mathbf{1}$ is the constant eigenvector shown by the same color over all vertices; (b) \mathbf{u}_1 is a slow-varying eigenvector shown by a smooth color transition from the top vertices to the bottom ones; (c) \mathbf{u}_9 is a faster-varying eigenvector over the graph shown by the multiple color variations in adjacent vertices.

increasing order $0 = \lambda_0 < \lambda_1 \leq \dots \leq \lambda_{K-1}$.

The graph Fourier transform (GFT) of signal $\mathbf{y}(t)$ with respect to the Laplacian \mathbf{L} is

$$\tilde{\mathbf{y}}(t) = \mathbf{U}^H \mathbf{y}(t) \quad (3.3)$$

where $\tilde{\mathbf{y}}(t) = [\tilde{y}(0, t), \tilde{y}(1, t), \dots, \tilde{y}(K-1, t)]^H$ contains the GFT coefficients $\tilde{y}(k, t)$ for graph frequency index k of time t . The inverse GFT is

$$\mathbf{y}(t) = \mathbf{U} \tilde{\mathbf{y}}(t). \quad (3.4)$$

The GFT generalizes the temporal Fourier transform: for the graph being a cycle that represents the temporal axis of a periodic signal, the GFT matches the discrete Fourier transform [27]. The GFT analyzes the signal variation over the graph for a fixed time instant. Since the transform (eigenvector) matrix \mathbf{U} depends on the graph structure, it gives a harmonic decomposition for signals living in irregular domains where the traditional discrete Fourier transform cannot be applied. For readers familiar with spectral network theory, the GFT can also be seen as the signal projection onto the Laplacian eigenspace.

The GFT coefficients $\tilde{y}(k, t)$ for lower values of k indicate how much the slower varying eigenvectors over the graph contribute to $\mathbf{y}(t)$. For larger values of k , these coefficients indicate how much the faster varying eigenvectors over the graph contribute to $\mathbf{y}(t)$. The coefficient $\tilde{y}(0, t)$ indicates the contribution of the constant component (equal to $1/\sqrt{K}$ at each vertex) on $\mathbf{y}(t)$ [35]. Therefore, index k is called the graph frequency index. Figure 3.2 depicts three eigenvectors of the considered graph: the eigenvector \mathbf{u}_k changes more rapidly over adjacent vertices for larger k .

Just like temporal bandlimited signals, we can define bandlimited graph signals. In many practical cases, the coefficients $\tilde{y}(k, t)$ have only a few non-zero entries. A bandlimited graph signal $\mathbf{y}(t)$ is therefore defined as a graph signal with GFT coefficients [35]

$$\tilde{y}(k, t) = 0, \text{ for } k > K_0 \in \{0, \dots, K-1\} \quad (3.5)$$

implying the signal has no content outside the graph frequency band of $\{0, K_0\}$. In this study, we will often see that EGM signals exhibit a bandlimited behavior over the graph.

To measure the signal variation over the graph, the graph Laplacian quadratic form of $\mathbf{y}(t)$ is defined as [35]

$$\begin{aligned} V_{\mathcal{G}}(\mathbf{y}(t)) &= \mathbf{y}(t)^H \mathbf{L} \mathbf{y}(t) \\ &= \sum_{i \in \mathcal{V}} \sum_{j \in \mathcal{N}_i} W_{i,j} (y(i, t) - y(j, t))^2. \end{aligned} \quad (3.6)$$

This quadratic form shows that the variation of signal $\mathbf{y}(t)$ over the vertices for a fixed t is a weighted sum of the difference between any two connected vertices. The edge weight indicates the contribution of a connection to the overall variation. If $V_{\mathcal{G}}(\mathbf{y}(t))$ is small, the signal is smooth, i.e., it has similar values in adjacent vertices. If $V_{\mathcal{G}}$ is large, the signal changes faster over the graph, i.e., it has different values in adjacent vertices. For the three eigenvector signals in Figure 3, we have $0 = V_{\mathcal{G}}(\mathbf{u}_0) < V_{\mathcal{G}}(\mathbf{u}_1) < V_{\mathcal{G}}(\mathbf{u}_9)$.

3.3.2. JOINT STFT AND GFT

Graph signal processing considers only a single time instant and does not capture the correlation across time. Since the signals we study are time-varying and non-stationary, the joint graph and short-time Fourier transform is defined next to exploit signal dependencies across both graph and time. In simple words, the short-time Fourier transform (STFT) [36] is applied first to transform the signal per vertex to the temporal frequency domain; this approximately decorrelates the data per vertex. Subsequently, the GFT is applied to each temporal frequency to treat each frequency as an independent graph signal.

Let us split the signal into M temporal frames of length T_M and let $\mathbf{y}(\tau, t) \in \mathbb{R}^{K \times 1}$ be the graph signal in frame $\tau \in \{0, \dots, M-1\}$ at time instant t , i.e., the signal of all electrodes at one time instant. We here apply a 100-point Hanning window with an 50% overlap on the signal to obtain the temporal frames. We collect all signals recorded in frame τ in the matrix

$$\begin{aligned} \mathbf{Y}(\tau) &= [\mathbf{y}(\tau, \tau T_M), \mathbf{y}(\tau, \tau T_M + 1), \dots, \\ &\quad \mathbf{y}(\tau, (\tau + 1) T_M - 1)] \in \mathbb{R}^{K \times T_M} \end{aligned} \quad (3.7)$$

where the i th row of $\mathbf{Y}(\tau)$ corresponds to the time-varying signal measured by the i th electrode in frame τ .

For the STFT transform, we consider F temporal frequency bins by applying a discrete temporal Fourier transform to each row of $\mathbf{Y}(\tau)$ (and therefore $F = T_M$). The STFT coefficient matrix of (3.7) at frame τ over the F temporal frequencies is

$$\hat{\mathbf{Y}}(\tau) = [\hat{\mathbf{y}}(\tau, 0), \hat{\mathbf{y}}(\tau, 1), \dots, \hat{\mathbf{y}}(\tau, F-1)] \in \mathbb{C}^{K \times F} \quad (3.8)$$

The f th column of $\hat{\mathbf{Y}}(\tau)$ with $f \in \{0, \dots, F-1\}$ represents the temporal frequency components of all vertices in frame τ and frequency bin f and is given by

$$\hat{\mathbf{y}}(\tau, f) = [\hat{Y}_1(\tau, f), \hat{Y}_2(\tau, f), \dots, \hat{Y}_K(\tau, f)]^T \in \mathbb{C}^K. \quad (3.9)$$

The GFT is then applied to each column $\hat{\mathbf{y}}(\tau, f)$ of $\hat{\mathbf{Y}}(\tau)$ separately to achieve the joint STFT and GFT matrix

$$\tilde{\mathbf{Y}}(\tau) = \mathbf{U}^H \hat{\mathbf{Y}}(\tau) \quad (3.10)$$

with $\tilde{\mathbf{y}}(\tau, t)$ being the GFT of the temporal frequency signal $\hat{\mathbf{y}}(\tau, f)$; the k th element $\tilde{y}(k, \tau, f)$ corresponds to the graph frequency index k . For a low value of k , this coefficient indicates how much the slowly varying graph component contributes to the temporal frequency f in time frame τ . Therefore, the joint coefficient quantifies the variation over the graph of a temporal frequency in a short-time period. In other words, each coefficient indicates the EGM variation over space and time. These values will be different when analyzed, for instance, during sinus rhythm compared with atrial fibrillation and they will reveal patterns of space-time variability about the disease.

To obtain again the time-vertex signal $\mathbf{Y}(\tau)$ [cf. (3.7)] from the joint transform representations, we first apply the inverse GFT to $\tilde{\mathbf{Y}}(\tau)$ as

$$\hat{\mathbf{Y}}(\tau) = \mathbf{U} \tilde{\mathbf{Y}}(\tau) \quad (3.11)$$

to get the STFT matrix $\hat{\mathbf{Y}}(\tau)$. Then, we apply the inverse STFT with overlap-adding to reconstruct the entire time domain signal from the segmented frames.

Similar to (3.6), the variation of the temporal frequency components $\hat{\mathbf{y}}(\tau, f)$ over the graph can be quantified by the Laplacian quadratic form

$$\begin{aligned} V_{\mathcal{G}}(\hat{\mathbf{y}}(\tau, f)) &= \hat{\mathbf{y}}(\tau, f)^H \mathbf{L} \hat{\mathbf{y}}(\tau, f) \\ &= \sum_{i \in \mathcal{V}} \sum_{j \in \mathcal{N}_i} W_{i,j} (\hat{Y}_i(\tau, f) - \hat{Y}_j(\tau, f))^2. \end{aligned} \quad (3.12)$$

The measure in (3.12) quantifies the graph variation of each temporal frequency f in time frame τ . Since the variation differs in different temporal frequencies, we consider the normalized variation

$$V_{\mathcal{G},n}(\hat{\mathbf{y}}(\tau, f)) = \frac{\hat{\mathbf{y}}(\tau, f)^H \mathbf{L} \hat{\mathbf{y}}(\tau, f)}{\hat{\mathbf{y}}(\tau, f)^H \hat{\mathbf{y}}(\tau, f)}. \quad (3.13)$$

We will in the sequel use this joint transform to analyze the EGMs in three domains: the time domain, the temporal frequency domain, and the graph frequency domain.

3.4. GRAPH-TIME SPECTRAL ANALYSIS

In this section, we perform a spectral analysis on the EGMs during both sinus rhythm and atrial fibrillation. We first conduct a separate analysis on the short-time Fourier transform and a separate analysis on the graph Fourier transform. Next, in Section 3.4.2, we conduct a joint transform analysis. As the individual STFT analysis and GFT analysis are of less importance for the remainder of this paper, we only present the main results of the individual STFT and GFT analyses.

3.4.1. STFT ANALYSIS & GFT ANALYSIS

For the STFT analysis, we analyzed the distribution of the signal energy across both time and temporal frequencies. We observed that the atrial activity has a wider frequency

bandwidth than the ventricular activity. This implies that the atrial activity varies faster across time than the ventricular activity. We also found that the atrial activity during sinus rhythm has more energy in higher temporal frequencies than during atrial fibrillation. This suggests atrial fibrillation reduces the high temporal frequencies of the atrial waves.

In the GFT analysis, we found that the atrial activity varies faster over the graph than the ventricular activity. We also observed that the EGM has a larger graph bandwidth during sinus rhythm than during atrial fibrillation. That is, the signal changes faster across the graph (hence epicardium) during sinus rhythm than during atrial fibrillation.

However, we may expect a higher spatial variation of the atrial activity during atrial fibrillation than during sinus rhythm. This is because the signal changes more frequently across time during atrial fibrillation. To explain this counterintuitive result in the GFT analysis, we need to exploit the association between the temporal and spatial variations. Since the temporal frequencies provide additional insights on the EGMs and since the GFT alone does not capture them, we analyze next the EGMs with the joint STFT and GFT to address the latter.

3.4.2. JOINT STFT AND GFT ANALYSIS

In the joint analysis, we analyzed the normalized signal energy in the joint short-time Fourier transform and graph Fourier transform domain. Figures 3.3(a) and 3.3(b) depict the results during sinus rhythm and atrial fibrillation for one patient. To improve visualization, we focus on the temporal frequencies 20 Hz, 40 Hz, 60 Hz, and 80 Hz. Overall, the temporal frequency components change slowly over the graph; this is reflected by the energy concentration in the lower graph frequencies. However, we also observed that higher temporal frequencies change faster over the graph compared with the lower ones; this is reflected by the higher energy concentration in the high graph frequencies for $f = 60$ Hz, and 80 Hz.

To quantify the graph spatial variations of the low (0 Hz to 100 Hz) and high (100 Hz to 500 Hz) temporal frequencies, we calculated the average variation following (3.13). Due to space limitation, we show in Figure 3.4 the results for four representative patients. We can see the high temporal frequencies have a larger graph variation compared to the lower temporal frequencies. This explains the result in the GFT analysis, i.e., the atrial activity has a higher spatial variation during sinus rhythm than during atrial fibrillation. Because from the STFT analysis, the atrial activity has more energy in the high temporal frequencies during sinus rhythm than during atrial fibrillation. This also suggests that the spatial variation is correlated to the temporal variation. If a signal changes rapidly across time, it will have higher energy in the high temporal frequencies. This high variation across time translates then into a higher variation over the graph.

During sinus rhythm, the spatial variation decreases to a small value when the ventricular activity appears. That is, the temporal frequencies change slower over the atria during the ventricular activity than during the atrial activity. However, during atrial fibrillation, the spatial variation during the ventricular rhythm is higher because of the coupling between the atrial and ventricular activities.

The above analysis motivates us to estimate a smooth ventricular signal from the mixed signal in the joint domain and then extract the atrial signal from the mixed signal

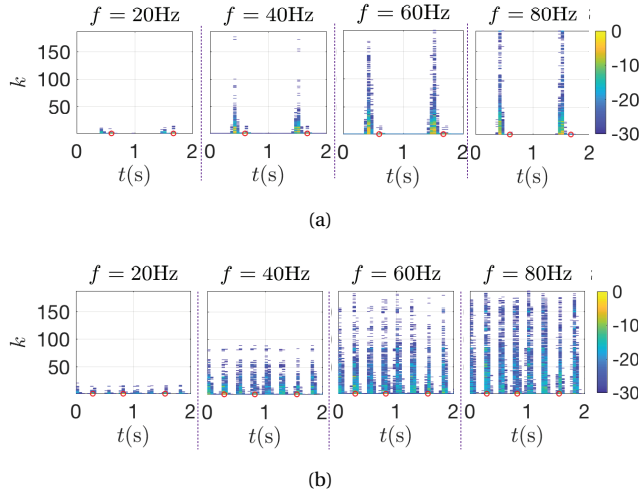


Figure 3.3: Normalized energy in dB in the joint graph and short-time Fourier transform domain. (a) sinus rhythm; (b) atrial fibrillation. The scalar k represents the graph frequency index, $t(s)$ the time in seconds, and f the temporal frequency. Each plot shows the spatial distribution of the signal energy as a function of time; different plots refer to different temporal frequencies. The red circles mark the peak of the ventricular activity.

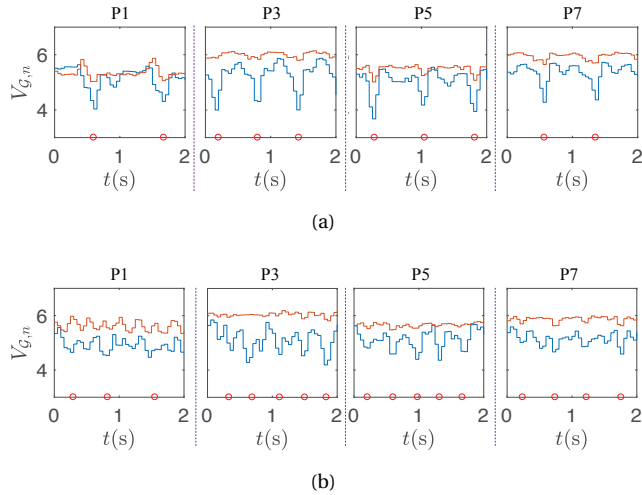


Figure 3.4: Smoothness measure over time of the low and high temporal frequencies in the joint graph and short-time Fourier transform domain for four patients labeled by 'P1', 'P3', 'P5', and 'P7'. (a) sinus rhythm; (b) atrial fibrillation. The red and blue lines indicate the mean smoothness of the low and high temporal frequencies, respectively. The red circles mark the peak of the ventricular activity.

by subtracting the ventricular signal from the mixed signal. The separation of the atrial signal and ventricular signal is infeasible by the STFT alone (which ignores correlation across space) or by the GFT alone (which ignores correlation across time). Since the joint transform analyzes the graph signal in short-time periods, it improves separation of the two activities in the joint domain. In the next section, we will leverage these observations to extract the atrial activity in the joint domain.

3.5. GRAPH-BASED ATRIAL ACTIVITY EXTRACTION

Recall that the atrial activity measurements are often corrupted by ventricular activity. In the sequel, we propose an algorithm to extract the atrial activity from the mixed measurements based on the joint graph-time variation.

The graph-time analysis in Section 3.4.2 showed the ventricular activity is smoother over the graph than the atrial activity. We, therefore, exploit the difference in smoothness to estimate the ventricular activity from the noisy epicardial measurement. The atrial activity can be then obtained by subtracting the estimated ventricular activity from the EGM.

By considering the EGM as a linear combination of the atrial and the ventricular activities [29], we can write the mixed signal $\mathbf{y}(t)$ over the K electrodes at time t as

$$\mathbf{y}(t) = \mathbf{a}(t) + \mathbf{v}(t) \quad (3.14)$$

where $\mathbf{a}(t)$ indicates the atrial signal and $\mathbf{v}(t)$ the ventricular signals. By segmenting the signal into overlapping frames, we represent the signal at frame τ in matrix form as

$$\mathbf{Y}(\tau) = \mathbf{A}(\tau) + \mathbf{V}(\tau) \quad (3.15)$$

where $\mathbf{Y}(\tau)$, $\mathbf{A}(\tau)$, and $\mathbf{V}(\tau)$ are $K \times T_M$ matrices following from (3.7). Then, from the joint STFT and GFT transform we get the joint spectral representation

$$\tilde{\mathbf{Y}}(\tau) = \tilde{\mathbf{A}}(\tau) + \tilde{\mathbf{V}}(\tau) \quad (3.16)$$

where $\tilde{\mathbf{Y}}(\tau)$, $\tilde{\mathbf{A}}(\tau)$, and $\tilde{\mathbf{V}}(\tau)$ are the joint transforms of the mixed EGM signal, atrial activity, and ventricular activity, respectively. The respective columns are $\tilde{\mathbf{y}}(\tau, f)$, $\tilde{\mathbf{a}}(\tau, f)$, and $\tilde{\mathbf{v}}(\tau, f)$.

Since the ventricular activity $\tilde{\mathbf{v}}(\tau, f)$ is smoother over the graph than the atrial activity $\tilde{\mathbf{a}}(\tau, f)$, we estimate $\tilde{\mathbf{v}}(\tau, f)$ as a smooth graph signal reconstruction with minimum distortion from the mixed EGM $\tilde{\mathbf{y}}(\tau, f)$. This consists of solving the problem

$$\begin{aligned} & \underset{\tilde{\mathbf{v}}(\tau, f)}{\text{minimize}} \quad \|\tilde{\mathbf{y}}(\tau, f) - \tilde{\mathbf{v}}(\tau, f)\|_2^2 \\ & \text{subject to} \quad \frac{\tilde{\mathbf{v}}^H(\tau, f) \Lambda \tilde{\mathbf{v}}(\tau, f)}{\tilde{\mathbf{v}}^H(\tau, f) \tilde{\mathbf{v}}(\tau, f)} \leq c, \end{aligned} \quad (3.17)$$

where the cost function seeks for finding a ventricular signal $\tilde{\mathbf{v}}(\tau, f)$ that is close to the EGM measurement $\tilde{\mathbf{y}}(\tau, f)$, while the constraint, with Λ the eigenvalues of the graph Laplacian, imposes the maximum normalized variation to be at most c for all frames τ and temporal frequencies f [cf. (3.13)].

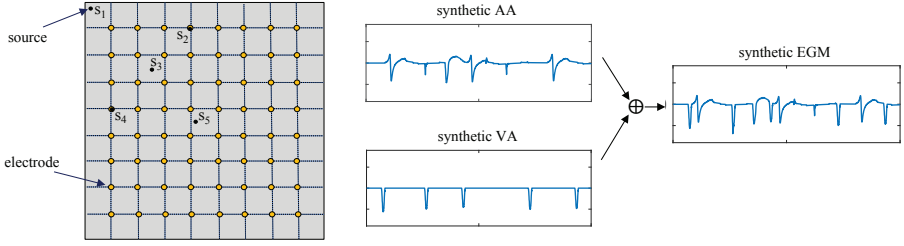


Figure 3.5: Simulation set up and synthetic signals during atrial fibrillation. *Left*: simulated two-dimensional tissue with 8×8 electrodes on top of it. Five foci sources s_1 to s_5 initiate the atrial fibrillation. *Right*: An example of synthetic atrial activity (AA), ventricular activity (VA), and mixed epicardial electrogram (EGM) with an atrial cycle length of 160 ms.

The ventricular activity estimated from (3.17) is given by the closed-form expression

$$\tilde{\mathbf{v}}(\tau, f) = [(1 - \mu c)\mathbf{I} + \mu\Lambda]^{-1}\tilde{\mathbf{y}}(\tau, f) \quad (3.18)$$

where μ is the so-called Lagrangian multiplier. After estimating the ventricular activity, we can recover the atrial activity by

$$\tilde{\mathbf{a}}_{\text{est}}(\tau, f) = \tilde{\mathbf{y}}(\tau, f) - \tilde{\mathbf{v}}(\tau, f). \quad (3.19)$$

Finally, we obtain the time domain signals through the inverse transforms.

The proposed algorithm relies on the presence of the ventricular activity. Since the ventricular activity has most of its energy in the zero graph frequency (see Figure 3.3), we can detect it by thresholding the signal energy in the joint STFT and GFT domain. If the energy in the zero graph frequency index ($k = 0$) exceeds this threshold, it indicates the presence of the ventricular activity. We can see that the graph-time spectral analysis provides us new insights into the atrial and the ventricular activities, which help to detect and cancel the ventricular activity from measurements.

3.6. EVALUATION OF ATRIAL ACTIVITY EXTRACTION

To evaluate the performance of the proposed graph-based atrial activity extraction (GAE) algorithm, we need the ground truth pure atrial activity. However, this is unknown for real measurements; hence, we first evaluate the GAE algorithm with synthetic signals and then perform additional experiments with real EGMs. We compared the GAE algorithm with three popular alternatives: average beat subtraction (ABS) [28]; adaptive ventricular cancellation (AVC) [29]; and independent component analysis (ICA) [29].

3.6.1. SYNTHETIC DATA GENERATION

There exists several methods to simulate the atrial activity, see e.g., [37–40]. These algorithms simulate well the electrogram during sinus rhythm, but face difficulties during atrial fibrillation. This is because of the overlap between the atrial and the ventricular activities. Also, these methods are more suitable to generate body surface ECGs rather than EGMs. The work in [41] generates atrial EGMs by simulating the activation of the

atrial fibers from the movement of a single dipole, which is less realistic. In this work, we focus on the atrial cell level to model the action potential during atrial fibrillation and extend it to the two-dimensional monodomain tissue. The atrial fibrillation is driven by the so-called ectopic foci sources that are located in various points of the tissue. This is one of the standard atrial fibrillation mechanisms in advanced research [42, 43].

The cell action potential follows the Courtemanche model of human atrial cells [44]. To simulate the atrial activity during atrial fibrillation, we reduced the ionic conductance of I_{to} to 50%, I_{Kur} to 50% and I_{CaL} to 30% [45]. This is based on the experimental study of chronic atrial fibrillation in [45]. After generating the signal at the cell level, we used the reaction-diffusion equation to simulate the propagation of the action potential along the tissue [46]. The diffusion equation is given by

$$C_m \frac{\partial V_m}{\partial t} = I_{tm} + I_{stim} - I_{ion}, \quad (3.20)$$

where V_m is the transmembrane potential, $C_m = 100$ pF is the transmembrane capacitance, I_{ion} is the total ionic current calculated from the Courtemanche model, I_{stim} is the stimulus current, and I_{tm} is the transmembrane current. The latter is calculated as

$$I_{tm} = \frac{1}{S_v} \nabla \cdot (\mathbf{D} \nabla V_m), \quad (3.21)$$

where S_v is the surface-to-volume ratio, $\nabla(\cdot)$ is the partial derivative operator, and \mathbf{D} is the conductivity tensor.

We considered a two-dimensional tissue of 200×200 cells with a cell radius of $5 \mu\text{m}$. The longitudinal conductivity is 1.1 mS cm^{-1} . The transversal to longitudinal conductivity ratio is one-to-two. We discretized the model through finite differences with 0.01 cm spatial resolution and solved the reaction-diffusion equation [cf. (3.20)] with the Euler method with a time step of 0.05 ms . Five ectopic foci sources drove the irregular atrial activity as illustrated in Figure 3.5. We applied stimuli of 50 ms in length on these positions. Two atrial cycle length of 160 ms and 180 ms were used to simulate different degrees of atrial fibrillation. For each type, we generated six segments of 10s each.

After generating the atrial activity, the next step was to generate the ventricular activity. The ventricular morphology was obtained by cutting out the ventricular segment in a heart beat during real sinus rhythm [40]. We inserted local variations in the amplitude and width of the different ventricular segments. Finally, we added the ventricular activity to the synthetic atrial activity to generate the mixed EGM.

Given the high computational complexity of these simulations, we considered an array of only 8×8 electrodes with the same inter-electrode spacing as the mapping array in Figure 3.1. The array is put on the tissue to measure the atrial EGM. The atrial EGM $\Phi(\mathbf{z}, t)$ measured by the electrode at location \mathbf{z} at time t is calculated by [47]

$$\Phi(\mathbf{z}, t) = \frac{1}{4\pi\sigma_e} \int \frac{I_{tm}}{|\mathbf{z} - \mathbf{x}|} d\mathbf{x} \quad (3.22)$$

where \mathbf{z} and \mathbf{x} represent the location vectors of the electrode and the cell, respectively, and σ_e is the extra-cellular conductivity.

3.6.2. PERFORMANCE METRICS

In the synthetic data scenario, we compared the estimated atrial activity with the pure atrial activity in terms of the normalized mean square error (NMSE) and the cross-correlation coefficient (CC). The NMSE is defined as

$$\text{NMSE} = \frac{1}{K} \sum_{i=1}^K \left(\frac{\sum_{t=0}^{T-1} (a_i(t) - a'_i(t))^2}{\sum_{t=0}^{T-1} (a_i(t))^2} \right) \quad (3.23)$$

where T is the length of the estimated atrial signal in the time domain, $a_i(t)$ and $a'_i(t)$ are the pure and the estimated atrial signals of the i th electrode at time t , respectively. The NMSE measures the normalized difference between the pure and the estimated atrial signals averaged over K electrodes: a lower value indicates a better estimation.

The cross-correlation coefficient is defined as

$$\text{CC} = \frac{1}{K} \sum_{i=1}^K \left(\frac{\sum_{t=0}^{T-1} (a_i(t) - \bar{a}_i) (a'_i(t) - \bar{a}'_i)}{\sqrt{\sum_{t=0}^{T-1} (a_i(t) - \bar{a}_i)^2} \sqrt{\sum_{t=0}^{T-1} (a'_i(t) - \bar{a}'_i)^2}} \right) \quad (3.24)$$

where \bar{a}_i and \bar{a}'_i are the mean of the true atrial signals and the mean of the estimated atrial signals of the i th electrode, respectively. The CC measures the similarity between the pure and the estimated atrial signals averaged over K electrodes: it is close to one if the pure and estimated atrial activities are correlated, and it is close to zero otherwise.

When using real data, it is impossible to use intrusive measures and quantify the performance through NMSE and CC since the ground truth is unknown. Hence, we use two non-intrusive metrics, namely: the ventricular depolarization reduction (VDR) [29], which measures the amplitude reduction of the R-peak; and the ventricular residue (VR) similar to [48], which considers both the area and the amplitude of the QRS¹ interval in the atrial activity.

For an EGM containing Q ventricular segments, the amplitude reduction of the R-peaks averaged over K electrodes is

$$\text{VDR} = \frac{1}{K} \sum_{i=1}^K \left(\frac{1}{Q} \sum_{q=1}^Q 10 \log \left(\frac{R_{i,q}^m}{R'_{i,q}} \right) \right) \quad (3.25)$$

where $R_{i,q}^m$ is the q th R-peak amplitude of the mixed EGM (in the time domain) of the i th electrode, and $R'_{i,q}$ is the amplitude of the respective residue. A higher value of VDR indicates more reduction of the ventricular activity.

For an EGM containing Q ventricular activity segments, the averaged VR is

$$\text{VR} = \frac{1}{K} \sum_{i=1}^K \left(\frac{1}{Q} \sum_{q=1}^Q \left(\frac{A_{i,q} \sqrt{\sum_{t=b_{i,q}}^{e_{i,q}} (a'_i(t))^2}}{\sqrt{\frac{1}{T} \sum_{t=0}^T (a_i(t))^2}} \right) \right) \quad (3.26)$$

¹QRS is the combination of three graphical deflections (Q wave, R wave, and S wave) on a typical electrocardiogram.

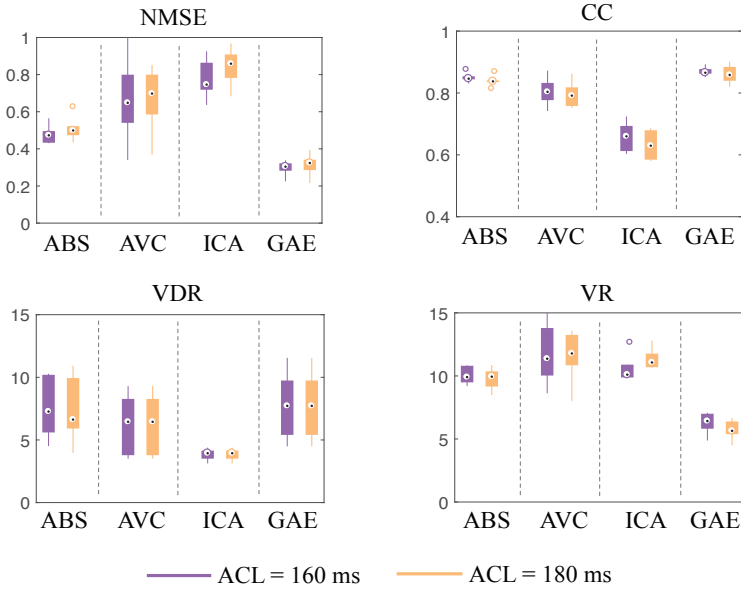


Figure 3.6: Boxplot performance on synthetic data of the average beat subtraction (ABS) [28], adaptive ventricular cancellation (AVC) [29], independent component analysis (ICA) [29], and the proposed graph-based atrial activity extraction (GAE) method. Two atrial cycle length (ACL) of 160 ms and 180 ms are considered. The proposed GAE method achieves the lowest normalized mean square error (NMSE) and ventricular residue (VR), and highest correlation coefficient (CC) and depolarization reduction (VDR) in both cases. The boxplots of NMSE, CC, and VR for the GAE method are comparatively short, which suggest that the GAE performance is more stable. Similar condensed boxplots are also observed for the ABS, but it presents outliers in the plots of NMSE and CC.

where $[b_{i,q}, e_{i,q}]$ is the q th QRS interval in the estimated atrial activity of the i th electrode, and $A_{i,q}$ is the maximum amplitude in this interval. A lower value of VR indicates a better extracted atrial activity.

3.6.3. RESULTS

Results on synthetic data: We evaluated the performance on the six segments for different degrees of atrial fibrillation. Figure 3.6 compares the proposed GAE algorithm with the reference methods. The performance of the GAE algorithm [cf. (3.18)] depends on the parameters c and μ . These parameters are chosen based on a grid search by minimizing the NMSE and are set to $c = 0.14$ and $\mu = 2$. We observe the proposed GAE method outperforms the other alternatives by achieving the smallest NMSE and VR, and the largest CC and VDR for both degrees of atrial fibrillation. The ABS performs worse since it cannot adapt to changes in the EGM morphology caused by the heart activity variations. The performance of the AVC is unstable because it relies on the reference signal. The ICA performs poorly on this data since the independence assumption between the atrial and ventricular activities might not always hold in the EGM data.

To further illustrate the differences of these methods, we show in Figure 3.7 an arbi-

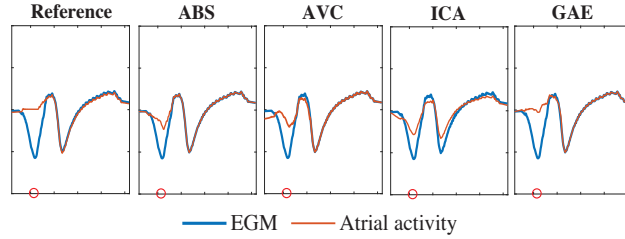


Figure 3.7: Illustrative example of the synthetic epicardial electrogram (EGM), synthetic pure atrial activity (AA) and the estimated atrial activity by the different algorithms. The left plot shows the synthetic EGM (blue) and the synthetic atrial activity (red). The other plots show the synthetic EGM (blue) and the estimated atrial activity (red) with different algorithms: average beat subtraction (ABS) [28]; adaptive ventricular cancellation (AVC) [29]; independent component analysis (ICA) [29]; proposed graph-based atrial activity extraction (GAE). The red circles mark the peak of the ventricular activity determined by the ECG measurements.

trary example of the synthetic EGM, the ground truth atrial activity, and the estimated atrial activity. We see the signal extracted by the GAE method approximates the ground truth better than the comparative algorithms. The ABS algorithm performs also well, but leaves more ventricular components compared to the GAE method. Also, the AVC and the ICA algorithms face difficulties in annihilating the ventricular component.

Results on real data: We move now on to the results on the clinical EGMs. We evaluated the performance only through the non-intrusive metrics VDR [cf. (3.25)] and VR [cf. (3.26)]. Table 3.1 groups the results for the ten patients. For each patient, it reports the averaged performance over all electrodes and the respective standard deviation (in brackets). We see an improved performance of the proposed GAE algorithm further corroborated with the real data.

Figure 3.8 shows a random example of the measured EGM and the extracted atrial activity by the different algorithms. The proposed GAE method extracts a smoother signal and has less ventricular component left. The extracted signal by ABS presents more fluctuations since ABS uses a fixed template to subtract the ventricular activity. The AVC shows a slightly better result than ABS, but it has more ventricular components left. The ICA can remove the ventricular activity well but fails in preserving the atrial activity.

3.6.4. COMPUTATIONAL COMPLEXITY & IMPLEMENTATION

The computational complexity of the GAE algorithm depends on the matrix inversion in (3.18). In each time frame and temporal frequency, the complexity is $\mathcal{O}(K^3)$, where K is the number of vertices (electrodes). For a signal with M time frames and T_M temporal frequencies, the computational complexity is $\mathcal{O}(M \times T_M \times K^3)$. This complexity is governed by the number of electrodes K in the array. For an array with large number of electrodes, the matrix inversion can be solved with the efficient conjugate gradient method to reduce the costs [49, 50].

For experiments, we implemented the GAE algorithm with MATLAB in an office laptop with 2.9 GHz Intel Core i5 processor and 8 GB RAM memory. The average run time for a segment of 10 s of data is around 1 s. The code for GAE algorithm is available at <https://github.com/MiaoSGit/GAE>. We remark that for the computation, improvements

Table 3.1: Comparison of different algorithms for different patients during atrial fibrillation

Patient No.	Metrics	ABS	AVC	ICA	GAE
P1	VDR	11.06 (3.31)	7.99 (4.87)	5.68 (5.39)	17.15 (6.31)
	VR	3.66 (2.08)	7.86 (2.89)	10.24 (1.84)	1.47 (0.50)
P2	VDR	10.09 (3.43)	7.96 (2.76)	6.37 (4.85)	16.98 (4.40)
	VR	2.93 (0.80)	8.16 (1.66)	6.60 (2.58)	1.19 (0.31)
P3	VDR	11.41 (4.26)	7.80 (3.67)	8.55 (4.42)	15.68 (4.34)
	VR	3.17 (0.74)	7.08 (1.42)	6.71 (1.65)	1.64 (0.58)
P4	VDR	15.02 (4.12)	9.55 (4.27)	7.42 (4.06)	16.85 (3.43)
	VR	4.20 (0.50)	9.40 (2.21)	6.69 (1.35)	1.80 (0.46)
P5	VDR	7.80 (3.26)	8.73 (4.76)	6.59 (4.26)	14.51 (3.57)
	VR	5.07 (0.67)	8.94 (3.28)	10.20 (1.98)	2.65 (0.46)
P6	VDR	9.84 (2.97)	8.39 (4.20)	5.84 (1.67)	16.57 (4.39)
	VR	6.74 (1.14)	12.37 (2.88)	7.30 (1.67)	2.43 (0.53)
P7	VDR	10.39 (4.21)	6.86 (5.33)	4.34 (1.63)	12.18 (4.64)
	VR	3.03 (0.79)	9.43 (1.99)	12.44 (2.16)	2.39 (0.68)
P8	VDR	5.72 (3.91)	5.27 (3.55)	5.94 (2.46)	11.95 (2.94)
	VR	4.36 (0.57)	8.59 (1.81)	12.40 (1.53)	2.60 (0.66)
P9	VDR	14.59 (4.62)	7.71 (4.35)	4.53 (3.79)	17.13 (5.54)
	VR	2.18 (0.74)	12.70 (1.76)	13.21 (4.53)	2.62 (0.76)
P10	VDR	9.52 (4.57)	8.69 (5.05)	8.45 (4.25)	14.93 (5.01)
	VR	5.49 (0.74)	8.83 (3.33)	6.18 (2.09)	2.14 (0.94)
Mean	VDR	10.55 (4.85)	7.90 (5.01)	6.30 (4.26)	15.39 (4.92)
	VR	4.08 (1.63)	9.34 (2.54)	9.20 (1.12)	2.09 (0.79)

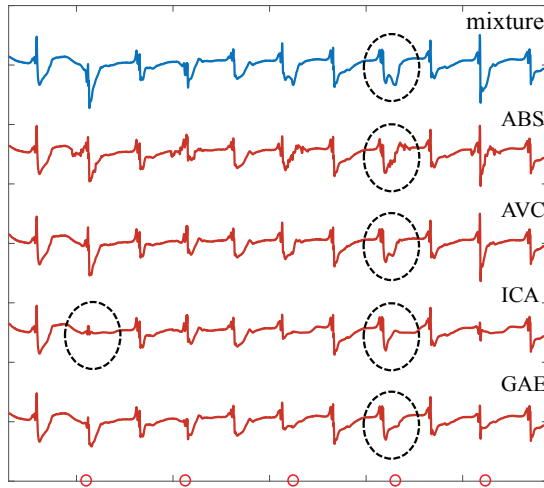


Figure 3.8: Illustrative example of the clinical epicardial electrogram (EGM) (blue) and the extracted atrial activity (red) by different algorithms: average beat subtraction (ABS) [28]; adaptive ventricular cancellation (AVC) [29]; independent component analysis (ICA) [29]; proposed graph-based atrial activity extraction (GAE). The proposed GAE method has less fluctuations and distortions and removes more ventricular activity.

can be achieved with a coding in C, but this goes beyond the scope of this work.

3.7. CONCLUSIONS

In this chapter, we suggested a new approach to study the epicardial electrograms for atrial fibrillation. This approach relies on graph signal processing—a recent research area in the signal processing community—to model electrograms during atrial fibrillation with a higher level model. We conducted a novel graph-time spectral analysis study to analyze the epicardial electrograms in the joint space, time, and frequency domains. We found the spatial variation is related to the high temporal variation; precisely, a faster temporal variation induces a high spatial variation. We also found that the atrial fibrillation reduces the high temporal frequencies of the atrial electrogram. Together, these observations suggest that atrial fibrillation decreases the spatial variation of the atrial activity. We also observed the ventricular activity is smoother over the graph compared with the atrial activity. In this respect, we designed a graph-based atrial activity extraction algorithm that leverages the smoothness prior to estimate the atrial activity. Our experimental results with synthetic data and real electrocardiograms showed the proposed method outperforms reference methods based on average beat subtraction, adaptive ventricular cancellation and independent component analysis.

In this chapter, we considered a physical graph model to capture the specific spatial connection of the nodes that represents the dependency of the data of different electrodes. Compared to a graph learning from data, the physical graph seems more limited when the data has hidden dependencies. However, not all of the data graphs have explicit meaningful interpretations, especially when there is little prior knowledge of the data or lack of sufficient training data. Since we don't have much prior knowledge of AF data, and the data varies from patient to patient, it is hard to provide the evidence to support the interpretation of a data graph. Therefore we start from the simple graph structure. However, it is quite regular, which is the limitation of the proposed method. More efforts are needed in future work to find a more meaningful graph structure through graph learning techniques.

REFERENCES

- [1] C. T. January, L. S. Wann, J. S. Alpert, *et al.*, *2014 AHA/ACC/HRS guideline for the management of patients with atrial fibrillation: a report of the American College of Cardiology/American Heart Association Task Force on Practice Guidelines and the Heart Rhythm Society*, *Journal of the American College of Cardiology* **64**, e1 (2014).
- [2] P. S. Miller, F. L. Andersson, and L. Kalra, *Are cost benefits of anticoagulation for stroke prevention in atrial fibrillation underestimated?* *Stroke* **36**, 360 (2005).
- [3] Y. Miyasaka, M. E. Barnes, K. R. Bailey, *et al.*, *Mortality trends in patients diagnosed with first atrial fibrillation: A 21-year community-based study*, *Journal of the American College of Cardiology* **49**, 986 (2007).
- [4] T. Nitta, Y. Ishii, Y. Miyagi, *et al.*, *Concurrent multiple left atrial focal activations with fibrillatory conduction and right atrial focal or reentrant activation as the mecha-*

- nism in atrial fibrillation*, The Journal of Thoracic and Cardiovascular Surgery **127**, 770 (2004).
- [5] V. Barbaro, P. Bartolini, G. Calcagnini, *et al.*, *Mapping the organization of atrial fibrillation with basket catheters, part i: Validation of a real-time algorithm*, Pacing and Clinical Electrophysiology **24**, 1082 (2001).
- [6] G. Calcagnini, F. Censi, A. Michelucci, and P. Bartolini, *Descriptors of wavefront propagation*, IEEE Engineering in Medicine and Biology Magazine **25**, 71 (2006).
- [7] V. Barbaro, P. Bartolini, G. Calcagnini, *et al.*, *Measure of synchronisation of right atrial depolarisation wavefronts during atrial fibrillation*, Medical and Biological Engineering and Computing **40**, 56 (2002).
- [8] C. P. Teuwen, C. Kik, L. J. M. E. van der Does, *et al.*, *Quantification of the arrhythmogenic effects of spontaneous atrial extrasystole using high-resolution epicardial mapping*, Circulation: Arrhythmia and Electrophysiology **11**, e005745 (2018).
- [9] T. H. Everett, L. Kok, R. H. Vaughn, *et al.*, *Frequency domain algorithm for quantifying atrial fibrillation organization to increase defibrillation efficacy*, IEEE Transactions on Biomedical Engineering **48**, 969 (2001).
- [10] V. Jacquemet, A. van Oosterom, and L. Vesin, J. and Kappenberger, *Analysis of electrocardiograms during atrial fibrillation*, IEEE Engineering in Medicine and Biology Magazine **25**, 79 (2006).
- [11] A. Bollmann, N. Kanuru, K. McTeague, *et al.*, *Frequency analysis of human atrial fibrillation using the surface electrocardiogram and its response to ibutilide*, The American Journal of Cardiology **81**, 1439 (1998).
- [12] Q. Xi, A. V. Sahakian, J. Ng, and S. Swiryn, *Atrial fibrillatory wave characteristics on surface electrogram: ECG to ECG repeatability over twenty-four hours in clinically stable patients*, Journal of Cardiovascular Electrophysiology **15**, 911 (2004).
- [13] R. P. Houben, N. M. S. de Groot, and M. A. Allesie, *Analysis of fractionated atrial fibrillation electrograms by wavelet decomposition*, IEEE Transactions on Biomedical Engineering **57**, 1388 (2010).
- [14] M. Brandstein and D. Ward, *Microphone arrays: signal processing techniques and applications* (Springer Science & Business Media, 2013).
- [15] B. D. van Veen and K. M. Buckley, *Beamforming: a versatile approach to filtering*, IEEE ASSP Magazine **5**, 4 (1988).
- [16] D. M. Lombardo, F. H. Fenton, S. M. Narayan, and W. Rappel, *Comparison of detailed and simplified models of human atrial myocytes to recapitulate patient specific properties*, PLoS Computational Biology **12** (2016).
- [17] M. Newman, *Networks* (Oxford university press, 2018).

- [18] W. Huang, L. Goldsberry, N. F. Wymbs, *et al.*, *Graph frequency analysis of brain signals*, *J. Sel. Topics Signal Processing* **10**, 1189 (2016).
- [19] J. D. Medaglia, W. Huang, E. A. Karuza, *et al.*, *Functional alignment with anatomical networks is associated with cognitive flexibility*, *Nature Human Behaviour* **2**, 156 (2018).
- [20] W. Huang, T. A. Bolton, J. D. Medaglia, *et al.*, *A graph signal processing perspective on functional brain imaging*, *Proceedings of the IEEE* **106**, 868 (2018).
- [21] C. Hu, J. Sepulcre, K. A. Johnson, *et al.*, *Matched signal detection on graphs: theory and application to brain imaging data classification*, *NeuroImage* **125**, 587 (2016).
- [22] E. Isufi, A. S. Mahabir, and G. Leus, *Blind graph topology change detection*, *IEEE Signal Processing Letters* **25**, 655 (2018).
- [23] H. Behjat, N. Leonardi, L. Sörnmo, and D. V. D. Ville, *Anatomically-adapted graph wavelets for improved group-level fmri activation mapping*, *NeuroImage* **123**, 185 (2015).
- [24] Y. Guo, H. Nejati, and N. Cheung, *Deep neural networks on graph signals for brain imaging analysis*, in *IEEE International Conference on Image Processing (ICIP)* (IEEE, 2017) pp. 3295–3299.
- [25] A. Yaksh, L. J. M. E. van der Does, *et al.*, *A novel intra-operative, high-resolution atrial mapping approach*, *Journal of Interventional Cardiac Electrophysiology* **44**, 221 (2015).
- [26] L. Sun, C. Yang, L. Zhang, *et al.*, *A preliminary study on atrial epicardial mapping signals based on graph theory*, *Medical Engineering & Physics* **36**, 875 (2014).
- [27] S. Aliaksei and M. F. M. José, *Big data analysis with signal processing on graphs: Representation and processing of massive data sets with irregular structure*, *IEEE Signal Processing Magazine* **31**, 80 (2014).
- [28] J. Slocum, E. Byrom, L. McCarthy, *et al.*, *Computer detection of atrioventricular dissociation from surface electrocardiograms during wide QRS complex tachycardias*, *Circulation* **72**, 1028 (1985).
- [29] J. J. Rieta and F. Hornero, *Comparative study of methods for ventricular activity cancellation in atrial electrograms of atrial fibrillation*, *Physiological Measurement* **28**, 925 (2007).
- [30] D. Raine, P. Langley, A. Murray, S. S. Furniss, and J. P. Bourke, *Surface atrial frequency analysis in patients with atrial fibrillation: assessing the effects of linear left atrial ablation*, *Journal of Cardiovascular Electrophysiology* **16**, 838 (2005).
- [31] J. J. Rieta, F. Castells, C. Sánchez, *et al.*, *Atrial activity extraction for atrial fibrillation analysis using blind source separation*, *IEEE Transactions on Biomedical Engineering* **51**, 1176 (2004).

- [32] P. Langley, J. J. Rieta, M. Stridh, *et al.*, *Comparison of atrial signal extraction algorithms in 12-lead ECGs with atrial fibrillation*, IEEE Transactions on Biomedical Engineering **53**, 343 (2006).
- [33] B. Abdi, R. C. Hendriks, A.-J. van der Veen, and N. M. De Groot, *Ventricular activity signal removal in atrial electrograms of atrial fibrillation*. in *Biosignals* (2019) pp. 179–184.
- [34] M. J. van Campenhout, A. Yaksh, C. Kik, and dothers, *Bachmann's bundle: A key player in the development of atrial fibrillation?* Circulation: Arrhythmia and Electrophysiology **6**, 1041 (2013).
- [35] D. I. Shuman, S. K. Narang, P. Frossard, A. Ortega, *et al.*, *The emerging field of signal processing on graphs: extending high-dimensional data analysis to networks and other irregular domains*, IEEE Signal Processing Magazine **30**, 83 (2013).
- [36] A. V. Oppenheim *et al.*, *Discrete-time signal processing (2nd Edition)* (1999).
- [37] J. J. Rieta *et al.*, *Atrial activity extraction based on blind source separation as an alternative to QRST cancellation for atrial fibrillation analysis*, in *Computers in Cardiology* (2000) pp. 69–72.
- [38] M. Stridh and L. Sornmo, *Spatiotemporal QRST cancellation techniques for analysis of atrial fibrillation*, IEEE Transactions on Biomedical Engineering **48**, 105 (2001).
- [39] F. Castells, J. J. Rieta, J. Millet, and V. Zarzoso, *Spatiotemporal blind source separation approach to atrial activity estimation in atrial tachyarrhythmias*, IEEE Transactions on Biomedical Engineering **52**, 258 (2005).
- [40] F. Castells, J. Igual, J. J. Rieta, *et al.*, *Atrial fibrillation analysis based on ICA including statistical and temporal source information*, in *IEEE International Conference on Acoustics, Speech, and Signal Processing* (2003) pp. V–94–96.
- [41] V. D. Corino, M. W. Rivolta, R. Sassi, *et al.*, *Ventricular activity cancellation in electrograms during atrial fibrillation with constraints on residuals' power*, Medical Engineering & Physics **35**, 1770 (2013).
- [42] M. Haissaguerre, P. Jaïs, D. C. Shah, *et al.*, *Spontaneous initiation of atrial fibrillation by ectopic beats originating in the pulmonary veins*, New England Journal of Medicine **339**, 659 (1998).
- [43] P. Ganesan, K. E. Shillieto, and B. Ghoraani, *Simulation of spiral waves and point sources in atrial fibrillation with application to rotor localization*, in *2017 IEEE 30th International Symposium on Computer-Based Medical Systems (CBMS)* (IEEE, 2017) pp. 379–384.
- [44] M. R. Courtemanche, R. J. Ramirez, and S. Nattel, *Ionic mechanisms underlying human atrial action potential properties: insights from a mathematical model*, American Journal of Physiology-Heart and Circulatory Physiology **275**, H301 (1998).

- [45] M. Courtemanche, R. J. Ramirez, and S. Nattel, *Ionic targets for drug therapy and atrial fibrillation-induced electrical remodeling: insights from a mathematical model*, Cardiovascular Research **42**, 477 (1999).
- [46] R. Plonsey and R. C. Barr, *Bioelectricity: a quantitative approach* (Springer Science & Business Media, 2007).
- [47] N. Virag, V. Jacquemet, C. S. Henriquez, *et al.*, *Study of atrial arrhythmias in a computer model based on magnetic resonance images of human atria*, Chaos: An Interdisciplinary Journal of Nonlinear Science **12**, 754 (2002).
- [48] R. Alcaraz and J. J. Rieta, *Adaptive singular value cancelation of ventricular activity in single-lead atrial fibrillation electrocardiograms*, Physiological Measurement **29**, 1351 (2008).
- [49] J. R. Shewchuk, *An introduction to the conjugate gradient method without the agonizing pain*, (1994).
- [50] J. Liu, E. Isufi, and G. Leus, *Filter design for autoregressive moving average graph filters*, IEEE Transactions on Signal and Information Processing over Networks **5**, 47 (2018).

4

CARDIAC TISSUE CONDUCTIVITY ESTIMATION USING CONFIRMATORY FACTOR ANALYSIS

IMPAIRED electrical conduction has been shown to play an important role in the development of heart rhythm disorders. Being able to determine the conductivity is important to localize the arrhythmogenic substrate that causes abnormalities in atrial tissue. In this work, we present an algorithm to estimate the conductivity from epicardial electrograms (EGMs) using a high-resolution electrode array. With these arrays, it is possible to measure the propagation of the extracellular potential of the cardiac tissue at multiple positions simultaneously. Given this data, it is in principle possible to estimate the tissue conductivity. However, this is an ill-posed problem due to the large number of unknown parameters in the electrophysiological data model. In this chapter, we make use of an effective method called confirmatory factor analysis (CFA), which we apply to the cross correlation matrix of the data to estimate the tissue conductivity. CFA comes with identifiability conditions that need to be satisfied to solve the problem, which is, in this case, estimation of the tissue conductivity. These identifiability conditions can be used to find the relationship between the desired resolution and the required amount of data. Numerical experiments on the simulated data demonstrate that the proposed method can localize the conduction blocks in the tissue and can also estimate the smoother variation in the conductivities. The conductivity values estimated from the clinical data are in line with the values reported in literature and the EGMs reconstructed based on the estimated parameters match well with the clinical EGMs.

This chapter is based on the paper published as "Cardiac Tissue Conductivity Estimation Using Confirmatory Factor Analysis" by M. Sun, N. M.S. de Groot, and R. C. Hendriks, *Computers in Biology and Medicine*, vol. 135, 2021.

4.1. INTRODUCTION

The electrical conductivity of cardiac tissue plays an important role in the origin of heart rhythm disorders. It has been shown that impaired electrical conduction and damage of atrial tissue are related to the development and progression of cardiac tachyarrhythmias [1–5]. For example, reduced conductivity facilitates development of atrial fibrillation, which comes with a high risk of strokes [4, 6]. Being able to infer the conductivity is important for localizing the arrhythmogenic substrate that causes atrial fibrillation. In this chapter we focus in particular on estimating the conductivity for atrial tissue based on epicardial electrograms (EGMs).

Tissue conductivity determines the ability of the tissue to transport electrical charge [7] and is related to the propagation of transmembrane current through the cardiac tissue. Previous research has proposed fully experimental methods or mathematical models to determine the conductivity from data, and the interested reader is referred to the reviews for more details [8–10]. One of the classic approaches is based on the cable theory, which relates the changes in the transmembrane potential to changes in the total ionic current and the conductivity of the tissue [7]. Based on this theory, bidomain models and monodomain models have been proposed to estimate tissue conductivity. The monodomain is a special case of the bidomain models which needs less model parameters and has been used extensively to simulate myocardial cells [11–13] and nerve cells [14].

With the development of high resolution electrode arrays, it is possible to measure the transmembrane potential of the tissue at multiple locations in a parallel manner [15–17]. With these high resolution spatial-temporal measurements, we can obtain a deeper understanding on the underlying structure of the tissue. In this work, we use the epicardial electrogram data measured using a high resolution mapping approach presented in [17]. However, inferring the conductivity parameters from such large amount of high dimensional data by inverse techniques is highly challenging. It is due to many unknown model parameters that need to be estimated first [18] and also due to the high dimensionality, nonlinearity, and stochasticity of the ill-posed inverse problems [13]. The work in [13] proposed a forward model using a monodomain approach and estimated tissue conductivity from measurements obtained by microelectrode arrays by solving a complex inverse problem. It is computationally intensive since ionic currents for all cells are needed to calculate the action potentials for conductivity estimation. To solve this problem, the authors in [19] proposed a compact model based on the work in [13, 20] to reduce the cost for computing the ionic currents of all cells and used the model to estimate the tissue conductivity from epicardial electrograms measured by high resolution mapping arrays. It is based on the assumption that all cells generate the same stereotype action potential once activated. This assumption was also used in [21] to reduce the computational intensity in the ECG forward model. However, the work in [19] assumes that the anisotropy ratio is fixed everywhere in the tissue and known before estimating the conductivity parameters. Also, it does not explicitly make use of the spatial structure of the data. In this work, we do not use the fixed and known anisotropy ratio assumption, but estimate the anisotropy ratio and conductivity parameters for all cell positions jointly, as opposed to [19]. We also make use of the spatial structure of the multi-electrode data to improve conductivity estimation. To do so, we exploit the cross

power spectral density matrix (CPSDM) of the EGMs and estimate the conductivity parameters using the CPSDM in combination with confirmatory factor analysis [22] (CFA).

CFA is a type of structural equation modelling that deals with the relationships between observed measurements and latent variables or factors [22]. With CFA, the observed measurements are intercorrelated and the variables or factors influence the correlations among the observations. In practice, CFA is usually confined to analyze variance-covariance structures and the parameters in the CFA model (such as factor loadings, factor variances and covariances), are estimated to reproduce the input variance-covariance matrix. Therefore, estimating the parameters from the CPSDM model (such as the power spectral densities of the sources) can be regarded as a CFA problem. For earlier works using CFA to estimate the parameters of a CPSDM model, one can refer to [23–26].

To estimate the parameters in the CPSDM model, the measurement model must first be identified. By analyzing the identifiability conditions in the CFA problem, we can verify whether the solution can be obtained with the given amount of data. In the current application this helps to analyze the relationship between the resolution that can be obtained for conductivity estimation and the required number of electrodes.

In order to easier satisfy the identifiability conditions in the CFA problem, we further propose simultaneous CFA across multiple temporal frequencies to estimate the tissue conductivity. This is based on the fact that the conductivity parameters are shared among multiple frequencies, which can increase the ratio between the number of equations and the number of unknown parameters. The proposed method also uses non-linear constraints to reduce the feasibility set of the parameter space with the prior knowledge of the parameters and thus increases the robustness of the estimation. The method also makes it possible to include constraints related to the mathematical properties of the problem at hand, e.g., to guarantee the positive semidefinite property of the CPSDMs.

The rest of the chapter is organized as follows. In Section 4.2, we introduce the notation used in this chapter and introduce the EGM models. In Section 4.3, we review the basic CFA theory and propose the simultaneous CFA for conductivity estimation and take some practical problems into account to increase the robustness of the proposed method. In Section 4.4, we conduct conductivity estimation experiments on the simulated data and discuss the results. In Section 4.5 we apply the estimation algorithm to the clinical data and evaluate its performance. We draw the conclusions in Section 4.6.

4.2. ELECTROGRAM MODEL

In this section, we first introduce the notation used in this chapter. Secondly, we introduce the background knowledge of electrical propagation in heart tissue and the EGM model that we use. After that, we introduce the time-domain impulse response model for the atrial EGM proposed in [19] and finally propose the CPSDM model, based on the impulse response model for conductivity estimation.

4.2.1. NOTATION

We use lower-case letters for scalars, bold-face lower-case letters for vectors, and bold-face upper-case letters for matrices. For example, a matrix \mathbf{A} can be written as $\mathbf{A} =$

$[\mathbf{a}_1, \dots, \mathbf{a}_m]$, where \mathbf{a}_i represents its i th column and a_{ij} represents an element of matrix \mathbf{A} at position (i, j) . The vector formed from the diagonal of the matrix $\mathbf{A} \in \mathbb{C}^{m \times m}$ is denoted as $\text{Diag}(\mathbf{A}) = [a_{11}, \dots, a_{mm}]^T$. A Hermitian positive semi-definite matrix is denoted as $\mathbf{A} \geq 0$. The Frobenius norm of a matrix is denoted as $\|\cdot\|_F$.

4.2.2. ELECTRICAL PROPAGATION & ELECTROGRAM MODEL

Pacemaker cells in heart tissue can initiate and conduct impulses to excite neighbouring cells. These atrial cells can conduct the impulses, generating a spread of excitation. When a cell is excited, its transmembrane potential increases until a threshold is reached and an action potential pulse is generated.

To describe the electrical propagation in a computational model, the tissue is discretized into a two-dimensional grid with N regular elements to model N cells, which is indexed by n ($n \in \{0, 1, \dots, N - 1\}$). Given a fixed Cartesian coordinate system, the conductivity tensor at the position of the n th cell can be written as [27]

$$\Sigma_n = \begin{bmatrix} \sigma_{xx,n} & \sigma_{xy,n} \\ \sigma_{yx,n} & \sigma_{yy,n} \end{bmatrix}, \tag{4.1}$$

which accepts the eigenvalue decomposition as

$$\Sigma_n = \mathbf{A}_c \Lambda_c \mathbf{A}_c^T \tag{4.2}$$

with

$$\mathbf{A}_c = \begin{bmatrix} \cos(\theta) & \sin(\theta) \\ \sin(\theta) & -\cos(\theta) \end{bmatrix} \quad \text{and} \quad \Lambda_c = \begin{bmatrix} \sigma_{L,n} & 0 \\ 0 & \sigma_{T,n} \end{bmatrix}, \tag{4.3}$$

where the columns of \mathbf{A}_c define the longitudinal and the transverse directions, $\theta(x, y)$ represents the fiber angle between the fiber and the x -axis at the position of the n th cell with coordinate (x, y) in the $x - y$ plane, and $\sigma_{L,n}$ and $\sigma_{T,n}$ represents the conductivity in the longitudinal direction and the transverse direction at the position of the n th cell, respectively. Figure 4.1 illustrates a 2D conductivity tensor as an example. The anisotropy ratio at the position of the n th cell is $\alpha_n = \sigma_{T,n} / \sigma_{L,n}$.

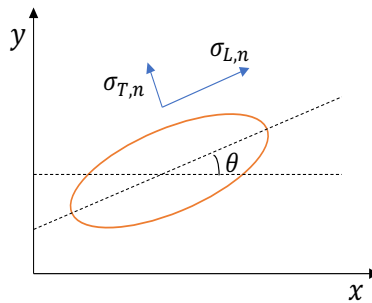


Figure 4.1: Example of a 2D conductivity tensor represented as an ellipse. The notation $\theta(x, y)$ represents the fiber angle between the fiber and the x - y plane.

We model the electrical propagation in heart tissue using the cable theory and the monodomain approach, which assumes that the intracellular and extracellular domains

have equal anisotropy ratios. Previous research has shown that the monodomain model can be a good approximation for its bidomain counterpart, even if the equal anisotropy assumption does not hold [28–30]. Electrical propagation in monodomain cardiac tissue at time t is governed by the reaction-diffusion equation [7]:

$$C \frac{\partial v_n(t)}{\partial t} = I_{\text{tm},n}(t) + I_{\text{st},n}(t) - I_{\text{ion},n}(t, v_n(t)) \quad (4.4)$$

where $v_n(t)$ is the transmembrane potential of the n th cell, C is the membrane capacitance, $I_{\text{st},n}(t)$ is the stimulus current, $I_{\text{ion},n}(t, v(t))$ is the ionic current, and $I_{\text{tm},n}(t)$ is the cell-to-cell transmembrane current per unit area that accounts for the spatial evolution of the action potential.

We consider M electrodes indexed by $m \in \{1, 2, \dots, M\}$ that are positioned on the atrial area. An atrial EGM measures the changes in the action potential of a group of cells close to the electrode. We use $r_{m,n}$ to denote the distance between the m th electrode and the n th cell and let $\mathbf{r}_m = \left[\frac{1}{r_{m,0}}, \frac{1}{r_{m,1}}, \dots, \frac{1}{r_{m,N-1}} \right]^T$. Stacking all cell potentials in a vector $\mathbf{v}(t) = [v_0(t), v_1(t), \dots, v_{N-1}(t)]^T$, the atrial EGM at the m th electrode can be modeled as [19, 20]

$$y_m(t) = \frac{aS_v^{-1}}{4\pi\sigma_e} \mathbf{r}_m^T \mathbf{D}_\sigma \mathbf{v}(t), \quad (4.5)$$

with a the area of each grid element, σ_e the constant extracellular conductivity, S_v the cellular surface to volume ratio, and \mathbf{D}_σ a double differentiation operator defined by [19],

$$\begin{aligned} \mathbf{D}_\sigma = & \mathbf{D}_{x,L} \text{Diag}(\boldsymbol{\sigma}_{xx}) \mathbf{D}_{x,R} + \mathbf{D}_{x,L} \text{Diag}(\boldsymbol{\sigma}_{xy}) \mathbf{D}_{y,R} \\ & + \mathbf{D}_{y,L} \text{Diag}(\boldsymbol{\sigma}_{yx}) \mathbf{D}_{x,R} + \mathbf{D}_{y,L} \text{Diag}(\boldsymbol{\sigma}_{yy}) \mathbf{D}_{y,R}, \end{aligned} \quad (4.6)$$

which is to realize the differentiation in the computation of the transmembrane current per cell [ref. Eq. (2.26) in Chapter 2]. Here, $\mathbf{D}_{x,L}$, $\mathbf{D}_{x,R}$, $\mathbf{D}_{y,L}$ and $\mathbf{D}_{y,R}$ are the first-order discretized spatial derivative operators. The conductivity vectors $\boldsymbol{\sigma}_{xx}$, $\boldsymbol{\sigma}_{yy}$, $\boldsymbol{\sigma}_{xy}$ and $\boldsymbol{\sigma}_{yx}$ stack the conductivity of all cells, i.e., $\sigma_{xx,n}$, $\sigma_{yy,n}$, $\sigma_{xy,n}$, $\sigma_{yx,n}$ (ref. Eq.(4.1)) for all $n \in \{0, 1, \dots, N-1\}$, respectively. For example, $\boldsymbol{\sigma}_{xx} = [\sigma_{xx,0}, \sigma_{xx,1}, \dots, \sigma_{xx,N-1}]^T$. In the calculation, the double differentiation operator is realized using the second-order central difference. Taking 4-by-4 cell (groups) as an example, Figure 4.2 illustrates the second-order difference applied on different cell positions (ignoring the conductivity). We now explain how the derivative operators act on the cell potentials \mathbf{v} in the x -direction. In this example, all cell potentials are stacked in the vector $\mathbf{v} = [v_0, v_1, \dots, v_{15}]^T$. Due to the boundary, the operator on the left side of $\text{Diag}(\boldsymbol{\sigma}_{xx})$, i.e., $\mathbf{D}_{x,L}$ is different from that on the right side, i.e., $\mathbf{D}_{x,R}$. The operator $\mathbf{D}_{x,R}$ is defined as

$$\mathbf{D}_{x,R} = \frac{1}{\Delta x} \begin{bmatrix} 0 & 0 & 0 & 0 & \cdots & 0 & 0 \\ -1 & 1 & 0 & 0 & \cdots & 0 & 0 \\ 0 & -1 & 1 & 0 & 0 & \cdots & 0 \\ 0 & 0 & -1 & 1 & 0 & \cdots & 0 \\ \vdots & \vdots & \vdots & \vdots & \vdots & \vdots & \vdots \\ 0 & 0 & 0 & \cdots & 0 & -1 & 1 \end{bmatrix}, \quad (4.7)$$

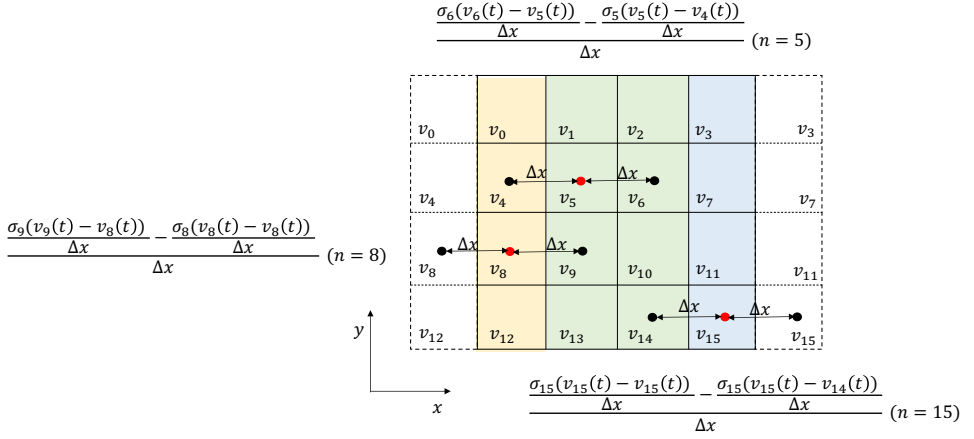


Figure 4.2: Illustration of second-order central difference applied on the positions of the cells on the central area (green area) and the left boundary (yellow area) and the right boundary (blue area), respectively. To realize the second-order central difference at the boundaries, we add virtual columns to the left and to the right, which has been incorporated in the first-order discretized spatial derivative operators $\mathbf{D}_{x,R}$ and $\mathbf{D}_{x,L}$.

while the operator $\mathbf{D}_{x,L}$ is defined as

$$\mathbf{D}_{x,L} = \frac{1}{\Delta x} \begin{bmatrix} -1 & 1 & 0 & 0 & \cdots & 0 & 0 \\ 0 & -1 & 1 & 0 & 0 & \cdots & 0 \\ 0 & 0 & -1 & 1 & 0 & \cdots & 0 \\ 0 & 0 & 0 & -1 & 1 & \cdots & 0 \\ \vdots & \vdots & \vdots & \vdots & \vdots & \vdots & \vdots \\ 0 & 0 & 0 & 0 & \cdots & 0 & -1 \end{bmatrix}. \quad (4.8)$$

with Δx the step size of the spatial derivative.

Let $Q = \frac{aS_v^{-1}}{4\pi\sigma_e}$. Eq. (4.5) can then be simplified as

$$y_m(t) = Q\mathbf{r}_m^T \mathbf{D}_\sigma \mathbf{v}(t). \quad (4.9)$$

To model the EGM with the model in (4.9), the action potentials of all cells are needed. The reaction-diffusion equation in (4.4) is often used to calculate the action potential of the cells, but it is complicated and time-consuming to solve. To solve this problem, it was proposed in [19] to assume that all cells generate the same stereotype action potential once activated and to use a simplified model - the impulse response model - to calculate the EGM. Next, we briefly introduce this model.

4.2.3. IMPULSE RESPONSE MODEL

Taking the cell with action potential $v_0(t)$ as reference, the action potential of the cell with index n is modelled as [19]

$$v_n(t) = v_0(t - \tau_n) = \delta(t - \tau_n) * v_0(t) \quad (4.10)$$

where $*$ is the convolution operator, $\delta(\cdot)$ is the Dirac delta function, and τ_n is the time delay of the n th cell with respect to the reference cell. This implies that the action potential at cell n is modelled by a stereotype action potential that is only delayed compared to the reference cell. With τ_0 for the reference cell set to $\tau_0 = 0$, the action potential of all cells can then be calculated as

$$\mathbf{v}(t) = \boldsymbol{\delta}_\tau(t) * v_0(t), \quad (4.11)$$

where

$$\boldsymbol{\delta}_\tau(t) = [\delta(t - \tau_0), \delta(t - \tau_1), \dots, \delta(t - \tau_{N-1})]^T. \quad (4.12)$$

Therefore, the atrial EGM measured by the m th electrode [ref. Eq. (4.9)] can be remodelled as

$$y_m(t) = \mathbf{Q}\mathbf{r}_m^T \mathbf{D}_{\sigma, \alpha} \boldsymbol{\delta}_\tau(t) * v_0(t). \quad (4.13)$$

This can be further simplified as

$$y_m(t) = a_m(t) * v_0(t), \quad (4.14)$$

with $a_m(t) = \mathbf{Q}\mathbf{r}_m^T \mathbf{D}_{\sigma} \boldsymbol{\delta}_\tau(t)$ the impulse response from all cells to the sensor at position m . We can see that the parameters of interest, i.e., the conductivities, are included in $a_m(t)$.

In addition to the atrial activity, the electrodes at the atrial area also measure the action potential of the ventricular cells and some noises. In this chapter, we are only interested in the parameters of the atrial tissue and aim to estimate the parameters when atrial activity is present. To simplify the problem, the ventricular activity is not taken into account in the model. Uncorrelated sensor noise is always present and reflects the limited accuracy of a sensor. The sensor self noise of the m th electrode is denoted by $u_m(t)$. Finally, the atrial EGM measured by the m th electrode is modelled as

$$y_m(t) = a_m(t) * v_0(t) + u_m(t). \quad (4.15)$$

In (4.15), $a_m(t)$ is deterministic, $v_0(t)$, $u_m(t)$, and $y_m(t)$ are stochastic. In particular, $v_0(t)$ represents a stereotype action potential (pulse), and it can vary from beat to beat. We also assume that $u_m(t)$ is zero-mean and uncorrelated across sensors and across time and is independent of $v_0(t)$. Due to the convolution operator in (4.15), it would be more convenient to estimate the parameters in the frequency domain.

4.2.4. CPSDM MODEL

Since the atrial waves might change across heart beats and the wavefronts can thus come from different directions for consecutive heart beats, the whole process is time variant and is not ergodic and non-stationary. To transform the time domain EGMs into frequency domain, we assume that the EGMs are stationary in a single heart beat and consider to use the short-time Fourier transform (STFT), which provides the time-localized frequency information when frequency components of a signal vary over time [31]. More concretely, we first sample the EGMs with a sampling interval of 1 ms (sample rate 1 kHz) and then divide a longer EGM signal into shorter heart beat segments of equal length by applying a rectangular window and finally compute the Fourier transform separately on each shorter segment, i.e., each time frame. A time frame is a heart beat segment that

includes most of the information in one heart cycle. A K-point FFT is then applied to the time frame to obtain the STFT coefficients in the frequency domain.

With proper zero padding, the convolutional EGM model (4.15) becomes a multiplication in frequency domain:

$$\tilde{y}_m(l, k) = \tilde{a}_m(l, k) \tilde{v}_0(l, k) + \tilde{u}_m(l, k) \quad (4.16)$$

where l is the time frame index, k is the frequency bin index, and $\tilde{y}_m(l, k)$, $\tilde{a}_m(l, k)$, $\tilde{v}_0(l, k)$, and $\tilde{u}_m(l, k)$ are the STFT coefficients of $y_m(t)$, $a_m(t)$, $v_0(t)$, and $u_m(t)$, respectively.

Stacking all electrodes in a vector, the EGM model in the STFT domain using vector notation is given by

$$\tilde{\mathbf{y}}(l, k) = \tilde{\mathbf{a}}(l, k) \tilde{v}_0(l, k) + \tilde{\mathbf{u}}(l, k), \quad (4.17)$$

where

$$\tilde{\mathbf{y}}(l, k) = [\tilde{y}_1(l, k), \dots, \tilde{y}_M(l, k)]^T, \quad (4.18)$$

$$\tilde{\mathbf{u}}(l, k) = [\tilde{u}_1(l, k), \dots, \tilde{u}_M(l, k)]^T, \quad (4.19)$$

and

$$\tilde{\mathbf{a}}(l, k) = [Q\mathbf{r}_1^T \mathbf{D}_\sigma \tilde{\boldsymbol{\delta}}_\tau(l, k), \dots, Q\mathbf{r}_M^T \mathbf{D}_\sigma \tilde{\boldsymbol{\delta}}_\tau(l, k)]^T \quad (4.20)$$

with

$$\tilde{\boldsymbol{\delta}}_\tau(l, k) = [\exp(-j \frac{2\pi f_s k}{K} \tau_0(l)), \dots, \exp(-j \frac{2\pi f_s k}{K} \tau_{N-1}(l))]^T, \quad (4.21)$$

where K is the FFT length, f_s is the sampling frequency, $\tau_n(l)$ represents the time delay of the n th cell with respect to the reference cell in the l th frame. Since the time delays $\tau_n(l)$ of the cells vary across heart beats, $\tau_n(l)$ for the l th time frame is relative to $\tau_0(l)$.

The CPSDM of the EGM in the l th frame and the k th frequency is then given by

$$\begin{aligned} \Phi_{\mathbf{y}}(l, k) &= E[\tilde{\mathbf{y}}(l, k) \tilde{\mathbf{y}}(l, k)^H] \\ &= \phi(l, k) \tilde{\mathbf{a}}(l, k) \tilde{\mathbf{a}}(l, k)^H + \Phi_{\mathbf{u}}(l, k), \end{aligned} \quad (4.22)$$

where $E(\cdot)$ represents the mathematical expectation, $\phi(l, k) = E[|\tilde{v}_0(l, k)|^2]$ is the power spectral density (PSD) of the reference cell that represents the power distribution of $v_0(t)$ in the frequency domain, and $\Phi_{\mathbf{u}}(l, k) = \text{Diag}([q_1, \dots, q_M]^T)$ with the m th diagonal element $q_m = E[|\tilde{u}_m(l, k)|^2]$ the PSD of the sensor self noise of the m th sensor. We estimate $\Phi_{\mathbf{y}}(l, k)$ by an instantaneous one sample estimate, i.e., $\hat{\Phi}_{\mathbf{y}}(l, k) = \tilde{\mathbf{y}}(l, k) \tilde{\mathbf{y}}(l, k)^H$, then $E(\hat{\Phi}_{\mathbf{y}}(l, k)) = \Phi_{\mathbf{y}}(l, k)$. Since the noise level in the EGMs is relatively small, the noisy EGM per frequency per time frame is approximately having rank one¹.

¹We generated the noisy EGMs by simulating clean atrial EGMs and adding white Gaussian noise on them and then we tested the rank of the noisy EGMs per frequency per time frame, i.e., $\Phi_{\mathbf{y}}(l, k)$, given a SNR equal to 0 dB, 10 dB, \dots , 50 dB. SNR is defined as $SNR_{dB} = 10 \log_{10} \frac{P_s}{P_n}$ where P_s is the power of the clean atrial EGM samples and P_n is the power of the noise samples. The results showed that the rank is approximately one in most of frequencies. In the model (4.22) for $\Phi_{\mathbf{y}}(l, k)$, this is only happens if $\Phi_{\mathbf{u}}(l, k) = \sigma_n^2 \mathbf{I}$ (so a multiple of the identity), and actually $\Phi_{\mathbf{y}}(l, k)$ is not rank one but has one large eigenvalue and others equal to σ_n^2 .

The unknown parameters of interest, i.e., conductivity vectors, are included in the spatial operator \mathbf{D}_σ in $\tilde{\mathbf{a}}(l, k)$ [ref. (4.6)]. To simplify the problem, we do not consider the fiber orientation in this work and assume that the conductivity tensor is aligned along the axes and the propagation direction of the action potential is decomposed in the x -direction and y -direction, i.e., we assume $\theta = 0$ in Eq. (4.1). (These assumptions are not realistic in practice but reduce the complexity of the problem.) Therefore, σ_{xy} and σ_{yx} in (4.6) are zero vectors and \mathbf{D}_σ is given by

$$\mathbf{D}_\sigma = \mathbf{D}_{x,L} \text{Diag}(\sigma_{xx}) \mathbf{D}_{x,R} + \mathbf{D}_{y,L} \text{Diag}(\sigma_{yy}) \mathbf{D}_{y,R}. \quad (4.23)$$

The ratio of the conductivity in the y -direction and the conductivity in the x -direction is called the anisotropy ratio. We denote the anisotropy ratio at the n th cell position as α_n and stack the anisotropy ratios at all cell positions as a vector $\boldsymbol{\alpha} = [\alpha_0, \alpha_1, \dots, \alpha_{n-1}]^T$. Let $\sigma_{xx} = \boldsymbol{\sigma}$, then the spatial operator now can be calculated as

$$\mathbf{D}_{\sigma,\alpha} = \mathbf{D}_{x,L} \text{Diag}(\boldsymbol{\sigma}) \mathbf{D}_{x,R} + \mathbf{D}_{y,L} \text{Diag}(\boldsymbol{\alpha}) \text{Diag}(\boldsymbol{\sigma}) \mathbf{D}_{y,R}. \quad (4.24)$$

where $\mathbf{D}_{\sigma,\alpha} \equiv \mathbf{D}_\sigma$ For isotropic tissue, the anisotropy ratio is fixed to $\boldsymbol{\alpha} = \mathbf{1}$.

4.2.5. PROBLEM FORMULATION

The goal of this chapter is to estimate the parameters $\boldsymbol{\sigma}$ and $\boldsymbol{\alpha}$, using only the noisy CPSDMs $\Phi_y(l, k)$ estimated from the EGMs and possibly having an initial estimate of $\phi(l, k)$, the activation time τ_n , and/or $\Phi_u(l, k)$.

To solve the problem, the number of knowns should be larger than the number of unknowns. The number of knowns depends on the number of electrodes. Given a certain number of electrodes, the number of unknowns depends on the chosen spatial resolution. In addition to estimating the conductivity, we also like to analyze the relation between the number of electrodes and the resolution that we can obtain. This can be achieved with the help of CFA, which we will introduce in the next section. To simplify the notation, we will neglect the indices of time samples, frequency bins and time-frames in the notation wherever possible.

4.3. CONFIRMATORY FACTOR ANALYSIS

In this section, we first review the CFA problem for parameter estimation and the identifiability conditions. Then, we adapt the CFA formulation to our problem and introduce the parameter estimation problem in the CPSDM model. To easier satisfy the identifiability conditions, we further propose simultaneous CFA, which estimates the parameters across multiple temporal frequencies. Practical considerations are also discussed at the end of this section.

4.3.1. THE GENERAL CFA PROBLEM

CFA methods have been proposed to estimate the parameters of the following model [22–25]:

$$\Phi_y = \mathbf{A} \Phi \mathbf{A}^H + \Phi_u \in \mathbb{C}^{M \times M} \quad (4.25)$$

where $\Phi_{\mathbf{y}}$ is an $M \times M$ variance-covariance matrix of the measurements, \mathbf{A} is an $M \times r$ matrix of unknown factor loadings, Φ is an $r \times r$ variance-covariance matrix of the r common factors, and $\Phi_{\mathbf{u}}$ is an $M \times M$ variance-covariance matrix of the residuals. The factors and the residues are assumed to be uncorrelated. The residues are also assumed to be mutually uncorrelated, i.e., $\Phi_{\mathbf{u}} = \text{Diag}([q_1, \dots, q_M]^T)$. As an example, in [26], CFA is used to jointly estimate the parameters in the multi-microphone signal model, and the matrices $\Phi_{\mathbf{y}}$, Φ , and $\Phi_{\mathbf{u}}$ are interpreted as the CPSDMs of the noisy signals of M microphones, the r sources, and the noises, respectively, while \mathbf{A} was used in [26] to model the early relative acoustic transfer functions of the sources with respect to the microphones. In the current work, we assume a single source, i.e., the action potential v_0 of the reference cell as introduced in (5), and therefore, $r = 1$ and $\Phi = \phi$ [ref. (4.22)]. The matrices $\Phi_{\mathbf{y}}$ and $\Phi_{\mathbf{u}}$ are the CPSDMs of the EGMs and the sensor self noises, respectively, and \mathbf{A} models the transfer function of the source, which describes the propagation from a source (reference) cell to the electrode. Since for any arbitrary non-singular matrix \mathbf{T} , we have $\mathbf{A}\Phi\mathbf{A}^H = \mathbf{A}'\Phi'\mathbf{A}'^H$, where $\mathbf{A}' = \mathbf{A}\mathbf{T}^{-1}$ and $\Phi' = \mathbf{T}\Phi\mathbf{T}^H$. This implies there is no unique solution. To guarantee a unique solution, we need to add some constraints on \mathbf{A} and Φ in the estimation.

CFA can be used to calculate the parameters in (4.25) using the following constrained optimization problem

$$\begin{aligned} \hat{\mathbf{A}}, \hat{\Phi}, \hat{\Phi}_{\mathbf{u}} &= \arg \min_{\mathbf{A}, \Phi, \Phi_{\mathbf{u}}} F(\hat{\Phi}_{\mathbf{y}}, \Phi_{\mathbf{y}}) \\ \text{s.t. } \Phi_{\mathbf{y}} &= \mathbf{A}\Phi\mathbf{A}^H + \Phi_{\mathbf{u}} \in \mathbb{C}^{M \times M}, \\ \Phi_{\mathbf{u}} &= \text{Diag}([q_1, \dots, q_M]^T), \\ q_m &\geq 0, m = 1, \dots, M, \\ \Phi &\geq 0, \\ a_{ij} &= \hat{a}_{ij} \in \mathbb{C}, \forall (i, j) \in \mathcal{T}, \\ \phi_{i'j'} &= \hat{\phi}_{i'j'} \in \mathbb{C}, \forall (i', j') \in \mathcal{K}. \end{aligned} \tag{4.26}$$

where $\hat{\Phi}_{\mathbf{y}}$ is the estimate of $\Phi_{\mathbf{y}}$ from the given data, $F(\hat{\Phi}_{\mathbf{y}}, \Phi_{\mathbf{y}})$ is a cost function such as the maximum likelihood, least square, or generalized least square, and where the constraints are used to incorporate model knowledge, for example the a priori knowledge from (4.25) and incorporating the knowledge that Φ is positive definite, and $\Phi_{\mathbf{u}}$ is diagonal and positive definite. In addition, constraints can be put on the elements of \mathbf{A} and Φ . This is expressed by the last two constraints in (4.26). In these constraints \mathcal{T} and \mathcal{K} are the sets of the selected row-column index-pairs of the matrices \mathbf{A} and Φ , respectively, with their elements a_{ij} and $\phi_{i'j'}$ fixed to some known constants $\hat{a}_{ij} \in \mathbb{C}$ and $\hat{\phi}_{i'j'} \in \mathbb{C}$ based on their priori knowledge. Note that the problem in (4.26) is not convex and may have multiple local minima.

There are two necessary conditions for the parameters of the CPSDM model to be uniquely identifiable. The *first identifiability condition* is that the number of equations should be larger than the number of unknowns. Therefore, some of the elements in \mathbf{A} and Φ are often fixed to make the remaining variables uniquely identifiable.

For guaranteeing unique identifiability, the *first identifiability condition* is not enough and the *second identifiability condition* is needed. For any arbitrary non-singular matrix

$\mathbf{T} \in \mathbb{C}^{r \times r}$, we have $\mathbf{A}\Phi\mathbf{A}^H = \mathbf{A}'\Phi'\mathbf{A}'^H$, where $\mathbf{A}' = \mathbf{A}\mathbf{T}^{-1}$ and $\Phi' = \mathbf{T}\Phi\mathbf{T}^H$ so that

$$F(\hat{\Phi}_{\mathbf{y}}, \mathbf{A}\Phi\mathbf{A}^H + \Phi_{\mathbf{u}}) = F(\hat{\Phi}_{\mathbf{y}}, \mathbf{A}'\Phi'\mathbf{A}'^H + \Phi_{\mathbf{u}}). \quad (4.27)$$

Therefore, there are infinite optimal solutions to the CFA problem in (4.26). Because there are r^2 variables in \mathbf{T} , the *second identifiability condition* of the CPSDM model in (4.25) is that we need to fix at least r^2 parameters in \mathbf{A} and Φ , i.e.

$$|\mathcal{T}| + |\mathcal{K}| \geq r^2. \quad (4.28)$$

This condition is necessary but not sufficient. Because we need to fix the proper parameters and not just any r^2 parameters such that the only possible matrix \mathbf{T} is $\mathbf{T} = \mathbf{I}$.

By analyzing the identifiability conditions in the CFA problem, we can determine the resolution that we can obtain with a given number of electrodes. In the following we will formulate the CFA problem for conductivity estimation and propose the simultaneous CFA for the robust estimation of the conductivity with some practical considerations.

4.3.2. CFA PROBLEM FOR CONDUCTIVITY ESTIMATION

Estimating parameters from the EGM CPSDM model in (4.22) from Section 4.2.4 can be regarded as a special case of the general CFA problem. To simplify the problem, we fix the PSD of the reference cell ϕ by a known constant $\hat{\phi}$, based on the action potential model of a cell. The Courtemanche model proposed in [32] is considered here to simulate multiple realizations of the action potential of an atrial cell and to estimate $\hat{\phi}$. The activation time of the cells under the electrodes are determined using the steepest descent method [33] followed by interpolation of the activation time for other cells. (In the next chapter we will further introduce how to estimate the activation time parameters using CFA.) For the reference cell with index zero, the activation time $\tau_0(l) = 0$ for all heart beats, i.e., $\forall l$. Based on this, the time delay τ_n with respect to the reference cell can be obtained. We also assume the constant parameter Q in the EGM model [ref. Eq.(4.13)] is known. With this prior knowledge, we propose the following CFA problem formulation for estimating the unknown parameters, i.e., the conductivities σ , the anisotropy ratios α , and the noise CPSDMs $\Phi_{\mathbf{u}}$ [ref. Eqs.(4.22) and (4.24)] at a particular frequency band with constraints (For ease of notation the time-frame index and the frequency index are left out):

$$\begin{aligned} \min_{\sigma, \alpha, \Phi_{\mathbf{u}}} \quad & F(\hat{\Phi}_{\mathbf{y}}, \Phi_{\mathbf{y}}) \\ \text{s.t.} \quad & \Phi_{\mathbf{y}} = \tilde{\mathbf{a}}\phi\tilde{\mathbf{a}}^H + \Phi_{\mathbf{u}} \in \mathbb{C}^{M \times M}, \\ & \tilde{\mathbf{a}} = [Q\mathbf{r}_1^T \mathbf{D}_{\sigma, \alpha} \tilde{\delta}_{\tau}, \dots, Q\mathbf{r}_M^T \mathbf{D}_{\sigma, \alpha} \tilde{\delta}_{\tau}]^T \in \mathbb{C}^{M \times 1}, \\ & \mathbf{D}_{\sigma, \alpha} = \mathbf{D}_{x, L} \text{Diag}(\sigma) \mathbf{D}_{x, R} + \mathbf{D}_{y, L} \text{Diag}(\alpha) \text{Diag}(\sigma) \mathbf{D}_{y, R} \in \mathbb{R}^{N \times N}, \\ & \tilde{\delta}_{\tau} = [\exp(-\frac{j2\pi f_s k}{K} \tau_0), \dots, \exp(-\frac{j2\pi f_s k}{K} \tau_{N-1})]^T, \in \mathbb{C}^{N \times 1} \\ & \Phi_{\mathbf{u}} = \text{Diag}[q_1, q_2, \dots, q_M] \in \mathbb{R}^{M \times M}, \\ & q_m \geq 0, m = 1, 2, \dots, M, \\ & \phi = \hat{\phi}, \\ & \tau_0(1) = 0. \end{aligned} \quad (4.29)$$

The loss function in (4.29) is defined using the least squares cost function as

$$F(\hat{\Phi}_{\mathbf{y}}, \Phi_{\mathbf{y}}) = \frac{1}{2} \|\hat{\Phi}_{\mathbf{y}} - \Phi_{\mathbf{y}}\|_F^2. \quad (4.30)$$

where $\|\cdot\|_F$ represents the Frobenius norm. The constraints in (4.29) incorporate the CPSDM model knowledge introduced in Section 4.2.4 and the prior knowledge of the parameters.

Prior to solving the problem in (4.29), we need to analyze the number of knowns and unknowns in (4.29). We start the analysis by taking one frequency bin into account. Since the estimated noisy CPSDM $\hat{\Phi}_{\mathbf{y}}$ is Hermitian symmetric, there are M^2 known real values, while there are $2N$ unknowns due to σ and α in \mathbf{D}_{σ} and M unknowns due to $\Phi_{\mathbf{u}}$. Therefore, the *first identifiability condition* is given by

$$M^2 \geq M + 2N. \quad (4.31)$$

This means that the number of cells N for which we can determine the conductivity is constrained by M as $N \leq \frac{M^2 - M}{2}$.

In our problem, the number of sources $r = 1$. According to the *second identifiability condition*, we need to impose $r^2 = 1$ independent restrictions on $\tilde{\mathbf{a}}$ and ϕ . Since we already assumed ϕ is known, the *second identifiability condition* is satisfied.

4.3.3. SIMULTANEOUS CFA IN MULTIPLE FREQUENCIES

In the previous section we considered estimation of the conductivity parameters σ and the anisotropy ratio parameters α observing the EGMs in only a single frequency band. However, note that we can assume that σ and α are constant across different frequencies within a certain range. Although [34] showed that for the human heart in general conductivity is frequency dependent, it follows from [34] that the conductivity is nearly constant within the frequency range from 0 to 100 Hz that we consider. By using multiple frequency bands, we can increase the ratio of known-to-unknown variables, when estimating the conductivity using the CPSDM. This allows to estimate the conductivity of more cells using the same number of electrodes. This can be done by solving the following simultaneous CFA (SCFA) problem:

$$\begin{aligned} \min_{\sigma, \alpha, \{\Phi_{\mathbf{u}}(k)\}} \quad & \sum_{\forall k \in S_f} F(\hat{\Phi}_{\mathbf{y}}(k), \Phi_{\mathbf{y}}(k)) \\ \text{s.t.} \quad & \Phi_{\mathbf{y}}(k) = \tilde{\mathbf{a}}(k)\phi(k)\tilde{\mathbf{a}}(k)^H + \Phi_{\mathbf{u}}(k), \forall k \in S_f, \\ & \tilde{\mathbf{a}}(k) = [\mathbf{Q}\mathbf{r}_1^T \mathbf{D}_{\sigma, \alpha} \tilde{\delta}_{\tau}(k), \dots, \mathbf{Q}\mathbf{r}_M^T \mathbf{D}_{\sigma, \alpha} \tilde{\delta}_{\tau}(k)]^T, \forall k \in S_f, \\ & \mathbf{D}_{\sigma, \alpha} = \mathbf{D}_{x, L} \text{Diag}(\sigma) \mathbf{D}_{x, R} + \mathbf{D}_{y, L} \text{Diag}(\alpha) \text{Diag}(\sigma_{\tau}) \mathbf{D}_{y, R}, \\ & \tilde{\delta}_{\tau}(k) = [\exp(-\frac{j2\pi f_s k}{K} \tau_0), \dots, \exp(-\frac{j2\pi f_s k}{K} \tau_{N-1})]^T, \forall k \in S_f, \\ & \Phi_{\mathbf{u}}(k) = \text{Diag}[q_1(k), q_2(k), \dots, q_M(k)], \forall k \in S_f, \\ & q_m(k) \geq 0, m = 1, 2, \dots, M, \forall k \in S_f, \\ & \phi(k) = \tilde{\phi}(k), \forall k \in S_f, \\ & \tau_0 = 0, \end{aligned} \quad (4.32)$$

where $S_f = \{k_1, \dots, k_N\}$ is the set of the frequency indices for conductivity estimation. Using the noisy CPSDM in $|S_f|$ frequency bands, the total number of knowns is $|S_f|M^2$ and the total number of unknowns is $2N - 1 + |S_f|M$ (Note that the time delay of the reference cell, i.e., τ_0 is known). The *first identifiability condition* is thus given by

$$|S_f|M^2 \geq 2N - 1 + |S_f|M. \quad (4.33)$$

Comparing (4.33) to (4.31), we can see that the SCFA problem needs less sensors than the CFA problem to satisfy the *first identifiability condition* when $|S_f| > 1$. The *second identifiability condition* in the SCFA problem is also always satisfied since $r = 1$ and we have fixed $\phi(k)$ for all k .

4.3.4. PRACTICAL CONSIDERATIONS

OVER-DETERMINED & MODEL-MISMATCH PROBLEM

Increasing the ratio of the number of equations over the number of unknowns makes the model fit better to the measurements when assuming the CPSDM model is accurate enough. The number of knowns are determined by the number of measurement positions, i.e., the sensors, while the number of unknowns is determined by the resolution at which we would like to estimate the conductivity. At the highest resolution this means the number of unknowns is determined by the number of cells. One way to increase this ratio is by reducing the resolution at which we estimate the conductivity.

Since the number of cells is large, estimating the conductivity at the finest resolution results in an unsolvable problem, i.e., the first identifiability condition in Eqs. (26) or (28) is unsatisfied. Therefore, instead of considering individual cells, we consider groups of cells and use the position of the center cell of the group to denote the position of the group. From now on we use the symbol N to denote the number of cell groups. The array that is used to measure the EGMs has electrode dimensions $M_x \times M_y$. The inter-electrode distance is constant and is denoted by d . The total number of electrodes is $M = M_x \times M_y$. The tissue is first discretized into $M_x \times M_y$ equal square areas and each electrode is assumed to be at the center of the square area. Then each area is discretized into $Z_x \times Z_y$ regular grid points. One grid point models one cell group. Let $N_x = Z_x \times M_x$ and $N_y = Z_y \times M_y$, which means the total number of cell groups is $N = N_x \times N_y = Z_x \times M_x \times Z_y \times M_y$. We define the spatial resolution of the cells as the number of cell groups in a given tissue area. Then the spatial resolution of the cells for which the conductivity is to be obtained, i.e., the number of unknowns to be estimated, is equal to $N_x \times N_y$. Let R denote the resolution scale compared to the number of electrodes, then $R = Z_x \times Z_y$. Figure 4.3 shows an example. Denote R the ratio of the spatial resolution to be obtained to the number of electrodes, then $R = Z_x \times Z_y$.

Rewriting the first identifiability criterion now in terms of R , the first identifiability condition in (4.33) becomes

$$|S_f|M^2 \geq 2RM - 1 + |S_f|M. \quad (4.34)$$

Decreasing R decreases the resolution N (increases the number of cells per group) and reduces the number of unknowns. However, it also reduces the model accuracy and increases the model-mismatch error compared to the conductivity of the actual cells.

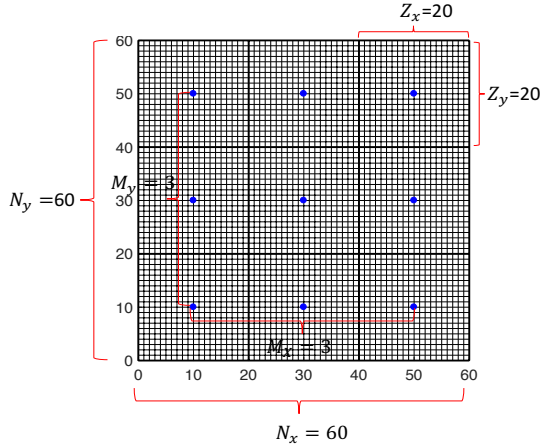


Figure 4.3: Discretization of tissue. There are $M_x \times M_y$ electrodes placed on the tissue. The tissue is divided into $M_x \times M_y$ areas with $Z_x \times Z_y$ cell groups for each area.

Each electrode is assumed to be at the center of the area.

We can also increase the ratio of knowns-to-unknowns by exploiting the fact that the conductivity is constant over frequency and estimate the conductivity simultaneously over multiple frequencies as proposed in Section 4.3.3. As the impact of model-mismatch problem can be different at different frequencies, we propose to use the frequencies that are less influenced by the decrease of the resolution. The measurements of the EGM can be regarded as the output of a low-pass filter on the heart tissue. Therefore, the high-frequency components of the EGM are less accurate than the low-frequency components and it is better to use low frequency components to estimate the parameters. This will be further investigated in Section 4.4.2.

BOX CONSTRAINTS ON THE PARAMETERS

To overcome CPSDM estimation errors and model-mismatch errors, we propose additional constraints on the parameters. Extra robustness can be achieved if the conductivities and the anisotropy ratios are box-constrained as $\sigma_{low} \leq \sigma \leq \sigma_{upper}$ and $0 < \alpha \leq 1$, where σ_{low} and σ_{upper} are the real valued upper and lower bounds of conductivity, respectively. Since the conductivity is non-negative, we can simply set $\sigma_{low} = 0$. For σ_{upper} , we select proper values based on the previous research on the conductivity of atrial tissue, respectively.

SOLVER

The CFA problem that we propose is a non-convex optimization problem, which can be solved with various solvers. We used the MATLAB optimization toolbox and the 'interior-point' algorithm to solve the problem, which is based on a combination of the methods in [35–37].

4.4. NUMERICAL EXPERIMENTS ON THE SIMULATED DATA

To verify the performance of the proposed method, we need the ground truth on the conductivity. As for clinical data, the true values of the physiological parameters are unknown, we perform numerical experiments on simulated data in this section, after which we perform experiments with clinical data in Section 4.5.

4.4.1. DATA GENERATION

In order to generate simulation data, we need to model individual cells, as well as cells integrated in larger tissue. In this work, we use the Courtemanche model proposed in [32] to model the atrial cells and calculate the total ionic current. Once the cell model is implemented, we can couple the cells together to form the tissue. We define the tissue to be two-dimensional and discretized into 90×90 regular grid points to model cells with 0.02 cm cell-to-cell distance. Notice that these cells are actually larger than real cells, which is done to reduce the computational complexity and memory requirements. To demonstrate the proposed algorithm under various conditions, we generate several isotropic and anisotropic tissues with different settings for conduction blocks, including:

- (i) homogeneous and isotropic tissue without areas of conduction block (conductivity is $\sigma_n = 1.1$ mS/cm for all n and $\alpha = 1$);
- (ii) inhomogeneous tissue with one area of conduction block and the area outside the conduction block is homogeneous and isotropic as in (i);
- (iii) inhomogeneous tissue with two areas of conduction block and the area outside the conduction block is homogeneous and isotropic as in (i);
- (iv) inhomogeneous tissue with one area of conduction block and the area outside the conduction block has a smooth variation in conductivity, varying from 0.77 mS/cm to 1.1 mS/cm and has a constant anisotropic ratio $\alpha_n = 0.4$;
- (v) inhomogeneous tissue with two areas of conduction block and the area outside the conduction block has a higher variation than (iv) in conductivity which varies from 0.75 mS/cm to 1.3 mS/cm and its anisotropic ratio α_n changes from 0.7 to 0.5 from left to right.

Before the tissue is activated by a stimulus, all the cells are at the initial conditions specified by the Courtemanche model. Then, we apply an external stimulus current $I_{st} = 200 \mu\text{A}$ to some source cells at the upper left corner of the tissue with duration of 0.5 ms, which triggers the propagation of the action potential through the tissue. By solving the reaction-diffusion equation in (4.4) using the forward Euler's method with a time step of 0.05 ms, we can calculate the action potential at every point of the tissue. The moment when a cell's potential reaches the threshold of -40 mV is considered as the cell's activation time. Since the electrical wave should not propagate further than the tissue boundaries, we take here into account the no-flux boundary conditions. The values of the other parameters that we used for the experiments are summarized in Table 5.1.

Figure 4.4(a) plots the central area of 45×45 cells and a 5×5 electrode array with inner-electrode distance 0.18 cm on top of this area. The EGMs are generated using (4.5).

Table 4.1: Summary of parameters used in the experiments

Parameters	Definition	Value
T	time-frame length	1000 samples
K	FFT length	1000
f_s	sampling frequency	1 kHz
C	membrane capacity	$1 \mu\text{F}/\text{cm}^2$
S_v	cellular surface to volume ratio	$0.24 \mu\text{m}^{-1}$
σ_{upper}	maximum conductivity of a cell	2 mS/cm
σ_e	extracellular conductivity	1.1 mS/cm

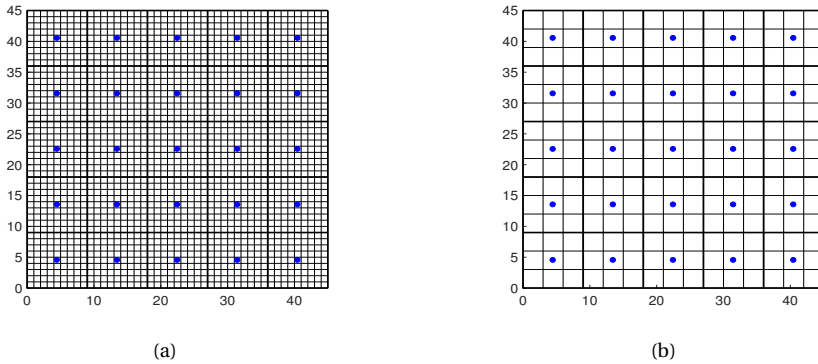


Figure 4.4: (a) Tissue with original resolution ($N_x \times N_y = 45 \times 45$); (b) Tissue with lower resolution ($N_x \times N_y = 15 \times 15$).

In the simulation experiments, we start with the case without noise added to the atrial EGM. Then, we generate noisy EGMs by adding Gaussian noise at 50 dB signal-to-noise ratio (SNR) to simulate sensor self noise. We also estimate the conductivity at different resolutions. As a reference, the proposed method is compared to the conductivity estimation method from [19].

4.4.2. MODEL TESTING

To reduce the number of unknowns in the estimation problem, we consider groups of cells as we introduced in Section III-D. For example, we take a block of 3×3 initial cells as a cell (group) in our model, as shown in Figure 4.4(b). Then we use the conductivity of the central cell of the block to replace the conductivity of the cell group in the low-resolution model. The spatial resolution of the cells to be estimated reduces from $N_x \times N_y = 45 \times 45$ to $N_x \times N_y = 15 \times 15$.

As we discussed in Section III-D, a reduced spatial resolution will increase the model-mismatch error. For comparison, we further generate the atrial EGMs using the impulse response model with different spatial resolutions and compare the generated EGMs. Figure 4.5(a) shows the conductivity map of the tissue, Figure 4.5(b) shows the activation

time map of the tissue, and Figure 4.5(c) gives examples of the cell action potential $v(t)$ and Figure 4.5(d) plots the spectral amplitude of the reference cell, respectively. The spectral amplitude of the reference cell is used to calculate parameter ϕ in the CPSDM model. Figure 4.5(e) shows the EGMs generated using different models and different resolutions, including 'E1': the EGM generated based on the reaction diffusion model in (4.5) using the original resolution (45×45), 'E2': the EGM generated based on the impulse response model in (4.13) using the original resolution (45×45), and 'E3': the EGM generated based on the impulse response model in (4.13) using the lower resolution (15×15), respectively. Figure 4.5(f) shows the spectral amplitudes of the EGMs in Figure 4.5(e). We observed that the generated EGMs have small differences in the morphology and decreasing the resolution increases the difference, as shown in Figure 4.5(e). From Figure 4.5(f) we also see that the model-mismatch error increases when the spatial resolution decreases, and the high frequency components are more affected than the low frequency components. Motivated by this, we use the lower frequency components rather than the higher frequency components as long as the identifiability conditions are satisfied. This can reduce the negative effect of the model-mismatch problem, which is unavoidable in practice. Some experiments are done as a function of the number of frequency components involved in the estimation algorithm. In that case, the number of frequency bands involved is increased by adding frequency bands towards the higher frequencies.

From Figure 4.5(f), we observe that the model-mismatch error is relatively large at 0 Hz. In the experiments, we do not use the 0 Hz frequency component when estimating the parameters.

4.4.3. EVALUATION

We estimate the conductivity at a lower resolution than what was used for data generation. In this way we can study the effect of the model-mismatch as well. We consider the resolution is R times the number of electrodes and set $R = 3.24$, $R = 4.84$, $R = 9$, and $R = 19.36$ by taking 5×5 cells, 4×4 cells, 3×3 cells, and 2×2 cells per block, respectively. The larger R represents the higher resolution, which implies a smaller model-mismatch. However, having a higher resolution also makes it harder to satisfy the identifiability conditions. Table 4.2 shows the number of knowns and unknowns for different resolutions when using one and ten frequency bands for parameter estimation, respectively. When $R = 19.36$, one frequency band is not enough and at least two frequency bands are needed for estimation.

We calculate the normalized mean square error (NMSE) to quantify the estimation performance. When the tissue is isotropic, that is, the longitudinal conductivity is equal to the transverse conductivity, the estimation error is equal in the two directions. In this case, the NMSE is calculated as

$$\text{Err} = \frac{\|\boldsymbol{\sigma} - \hat{\boldsymbol{\sigma}}\|^2}{N}, \quad (4.35)$$

where N represents the number of unknowns, $\boldsymbol{\sigma}$ represents the real conductivity and $\hat{\boldsymbol{\sigma}}$ represents its estimation. When the tissue is anisotropic, the longitudinal conductivity is unequal to the transverse conductivity. In this case, we first calculate the errors in the two different directions using (4.35) and then calculate the averaged error to evaluate the performance.

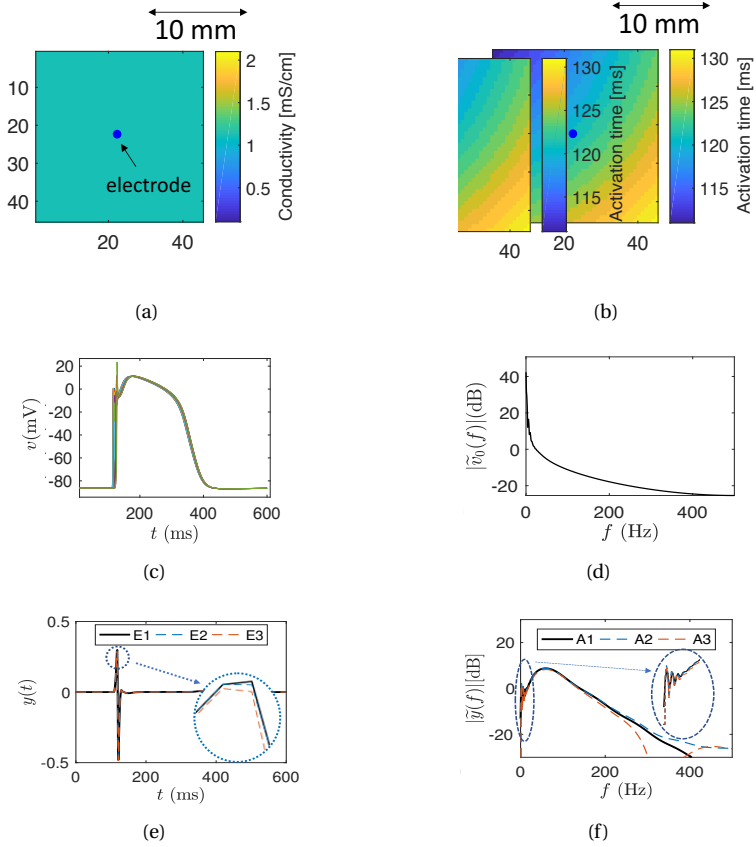


Figure 4.5: (a) Conductivity map; (b) Activation time map; (c) Examples of cell action potential; (d) Spectral amplitude of the reference cell; (e) Generated EGMs; (f) Spectral amplitudes of the EGMs. In (e), E1 represents the EGM generated based on the reaction-diffusion model. E2 and E3 represent the EGM generated based on the impulse response model using the original resolution (45×45) and the low resolution (15×15), respectively. In (f), A1, A2 and A3 represent the spectral amplitude of E1, E2, and E3, respectively.

Table 4.2: Number of Knowns and Unknowns in the Estimation Process.

Resolution scale	$ S_f $	Number of knowns	Number of unknowns
$R = 3.24$ ($N_x \times N_y = 9 \times 9$)	1	25×25 due to $\hat{\Phi}_y$	9×9 due to σ 9×9 due to α 25 due to $\hat{\Phi}_u$
	10	$25 \times 25 \times 10$ due to $\hat{\Phi}_y$	9×9 due to σ 9×9 due to α 25×10 due to $\hat{\Phi}_u$
$R = 4.84$ ($N_x \times N_y = 11 \times 11$)	1	25×25 due to $\hat{\Phi}_y$	11×11 due to σ 11×11 due to α 25 due to $\hat{\Phi}_u$
	10	$25 \times 25 \times 10$ due to $\hat{\Phi}_y$	11×11 due to σ 11×11 due to α 25×10 due to $\hat{\Phi}_u$
$R = 9$ ($N_x \times N_y = 15 \times 15$)	1	25×25 due to $\hat{\Phi}_y$	15×15 due to σ 15×15 due to α 25 due to $\hat{\Phi}_u$
	10	$25 \times 25 \times 10$ due to $\hat{\Phi}_y$	15×15 due to σ 15×15 due to α 25×10 due to $\hat{\Phi}_u$
$R = 19.36$ ($N_x \times N_y = 22 \times 22$)	1	25×25 due to $\hat{\Phi}_y$ (Not enough data for estimation)	22×22 due to σ 22×22 due to α 25 due to $\hat{\Phi}_u$
	10	$25 \times 25 \times 10$ due to $\hat{\Phi}_y$	22×22 due to σ 22×22 due to α 25×10 due to $\hat{\Phi}_u$

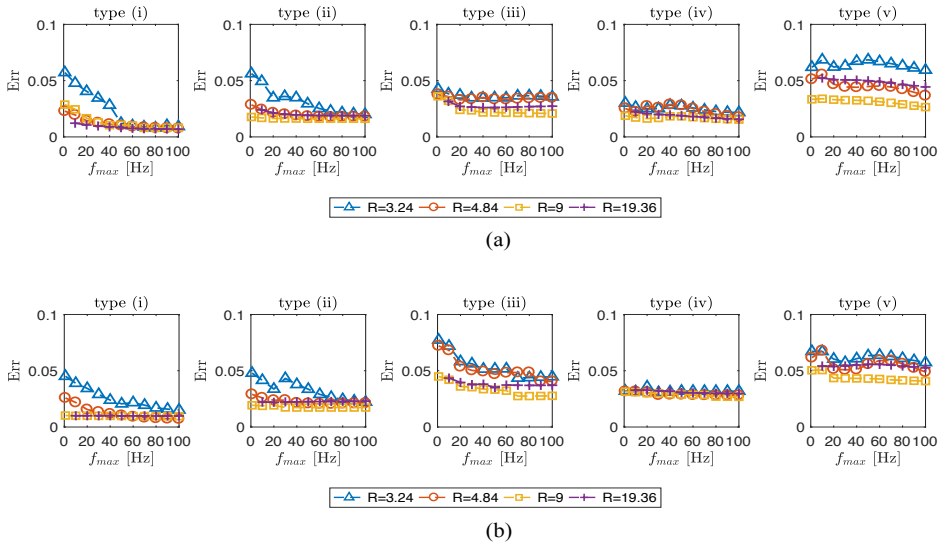


Figure 4.6: Estimation errors of conductivity parameters when $f_{max} = 1, 10, \dots, 100$ for different resolutions for different types of tissue, respectively. (a) The anisotropy ratio α is known. (b) The anisotropy ratio α is unknown and both σ and α are estimated. For the anisotropic tissue examples (iii), (iv), and (v), we calculate the average estimation errors in the longitudinal and the transverse directions and then plot the average values in the figures.

To focus on the conductivity estimation, we start the evaluation with the case where the activation time is known and there is no sensor self noise. Then we evaluate the algorithm having inaccuracies in activation time.

ASSUMING KNOWN ACTIVATION TIME

In this evaluation we first assume the anisotropy ratio is known, and only estimate the conductivity, and next consider the case when both α and σ are unknown and estimated. We use the proposed method to estimate the parameters given different frequency bands. We denote the frequency band for estimation by $[1, f_{max}]$ Hz and calculate the estimation errors when $f_{max} = 1, 10, \dots, 100$ for different resolutions and tissue types, respectively. That is, increasing $|S_f|$ [ref. (4.34)] from 1 to 100. The iterations in the algorithm stops when the change of the objective function is small enough.

Figure 4.6(a) and Figure 4.6(b) show the estimation errors for the estimation where the anisotropy ratio is known and for the situation where the anisotropy ratio is unknown and has to be estimated, respectively. Comparing the Figures 4.6(a) and 4.6(b), we see that the algorithm still works well without knowing the anisotropy ratio, although its performance degrades a little bit. We also see that the curves in Figure 4.6(a) and Figure 4.6(b) show a similar trend. From both figures (a) and (b), we see that for all tissue types the estimation error first decreases and then tends to stabilize with the increase of f_{max} in most cases. When R increases from 3.24 to 9, the resolution increases and the estimation error decreases, because the model-mismatch error gets smaller. In most of the cases, we see the performance degrades when R increases from 9 to 19.36. Although

the model is more accurate when $R = 19.36$, it has more parameters to fit and this estimation problem therefore is more challenging. We also see that the estimation error increases when increasing the number of areas with conduction block, since the underlying structure of the tissue is more inhomogeneous and reducing the resolution of the tissue increases the error in the model. Moreover, when increasing f_{\max} , the estimation error decreases faster for low resolution compared to a high resolution.

Figure 4.7 shows an example of the true simulated conductivity maps and the estimated conductivity maps given different number of frequency components and different resolutions for the five tissue examples (i)-(v) specified earlier in Section 4.4.1. Figure 4.7(a) shows the results for tissue (i), (ii), and (iii), where the tissue areas outside the blocks are isotropic, i.e., $\alpha = \mathbf{1}$. Figure 4.7(b) shows the results for tissue (iv) and (v), where the tissue areas outside the blocks are anisotropic, i.e., $\alpha \neq \mathbf{1}$. The anisotropic ratio is constant in example (iv) and is spatially-varying in example (v). Therefore, we show in Figure 4.7(b) both the longitudinal and transverse conductivity maps. In Figure 4.7, the first column shows the real conductivity maps, the second to the sixth columns show the estimated conductivity maps for the increasing resolution with the assumption of knowing the anisotropy ratio, and the last column shows the conductivity maps estimated without knowing the anisotropy ratio. We can observe from the second to the sixth columns that the performance is obviously improved when increasing the resolution from $R = 3.24$ to a higher resolution and increasing f_{\max} from $f_{\max} = 1$ to $f_{\max} = 100$. We also find that the area of the conduction block is more accurate in the high resolution map. From the estimated conductivity maps of tissue type (iv) in Figure 4.7(b), we find that the algorithm also works well when there is smooth variation in the conductivity maps. However, the estimated conductivity maps seem less accurate for more heterogeneous simulations (iv-v), mainly in case of non-constant anisotropy ratios and when the ratio is unknown. This could be a consequence of the fixed stereotype waveform for all cells.

HAVING INACCURACIES ON THE ACTIVATION TIME

Next, the conductivities are estimated using the activation time estimated from the measured EGMs instead of using the true activation time. They are estimated using the steepest descent approach [33], followed by linear interpolation to obtain a higher resolution activation time map for all modelled cells. We now use the proposed method (fixing $f_{\max} = 100$) to estimate the conductivity and use the CMM method from [19] as a reference. With the CMM method, the activation time of the cells is also estimated by the steepest descent method. Note that the CMM method assumes the anisotropy ratio is known and constant, while this is not required in the proposed SCFA method. We here calculate the estimation error for the CMM method taking known anisotropy ratio into account and calculate the estimation error using the proposed method taking both known and unknown anisotropy ratio into account. We also provide the estimated local conduction velocity (CV) map [38], which is commonly used in the literature for analysis of conduction block in tissue. Note that CV does not measure the conductivity parameters but only provides an estimation of the local velocity of the wave propagation in tissue.

Three tissue examples (iii)-(v) specified in Section 4.4.1 are used to test the estimation performance when there is no sensor self noise and with simulated white Gaussian

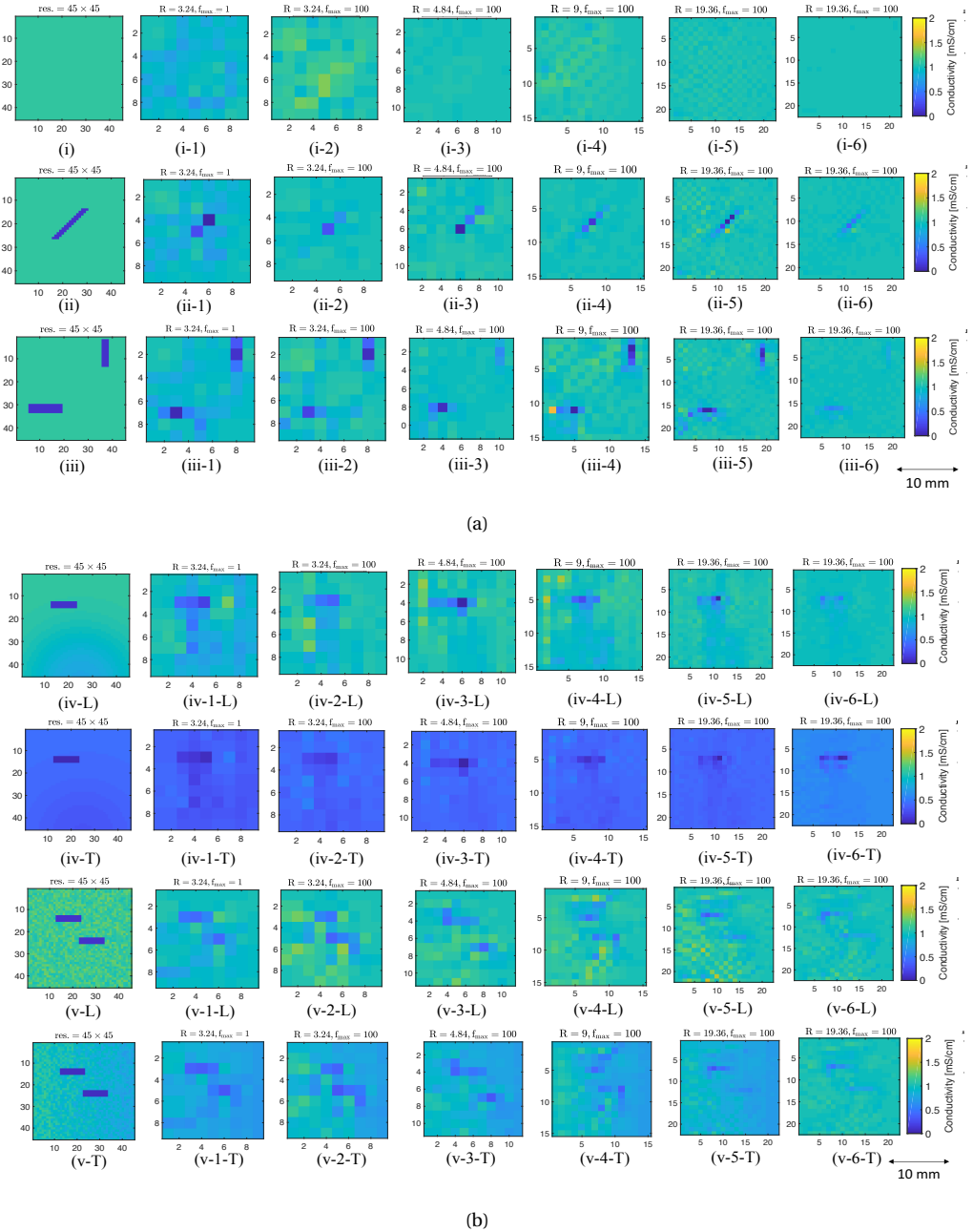


Figure 4.7: The subfigures in each row from the first to the sixth represent the real conductivity map, the estimated conductivity map when $R = 3.24$ with $f_{max} = 1$, $R = 3.24$ with $f_{max} = 100$, $R = 4.84$ with $f_{max} = 100$, $R = 9$ with $f_{max} = 100$, $R = 19.36$ with $f_{max} = 100$ assuming the anisotropy ratio is known, and the last subfigure shows the conductivity map estimated without knowing the anisotropy ratio when $R = 19.36$ with $f_{max} = 100$, respectively. (a) Conductivity maps for tissue types (i)/(ii)/(iii). (b) Longitudinal (L) and transversal (T) conductivity maps for tissue types (iv)/(v).

Table 4.3: Comparison of estimation error with different methods

Tissue type	With/Without noise	CMM (α is known)				SCFA (α is known)				SCFA (α is estimated)			
		R=3.24	R=4.84	R=9	R=19.36	R=3.24	R=4.84	R=9	R=19.36	R=3.24	R=4.84	R=9	R=19.36
type (iii)	without noise	0.0862	0.0710	0.0752	0.0691	0.0402	0.0487	0.0433	0.0452	0.0483	0.0477	0.0336	0.0502
	with noise	0.0862	0.0711	0.0752	0.0691	0.0402	0.0487	0.0435	0.0452	0.0483	0.0477	0.0336	0.0502
type (iv)	without noise	0.0472	0.0461	0.0343	0.0526	0.0303	0.0173	0.0209	0.0175	0.0416	0.0299	0.0274	0.0287
	with noise	0.0472	0.0461	0.0344	0.0526	0.0303	0.0174	0.0209	0.0175	0.0421	0.0300	0.0274	0.0290
type (v)	without noise	0.1322	0.1135	0.1191	0.1172	0.0695	0.0614	0.0661	0.0631	0.1111	0.0824	0.0795	0.0791
	with noise	0.1322	0.1136	0.1192	0.1173	0.0696	0.0614	0.0661	0.0633	0.1115	0.0825	0.0795	0.0791

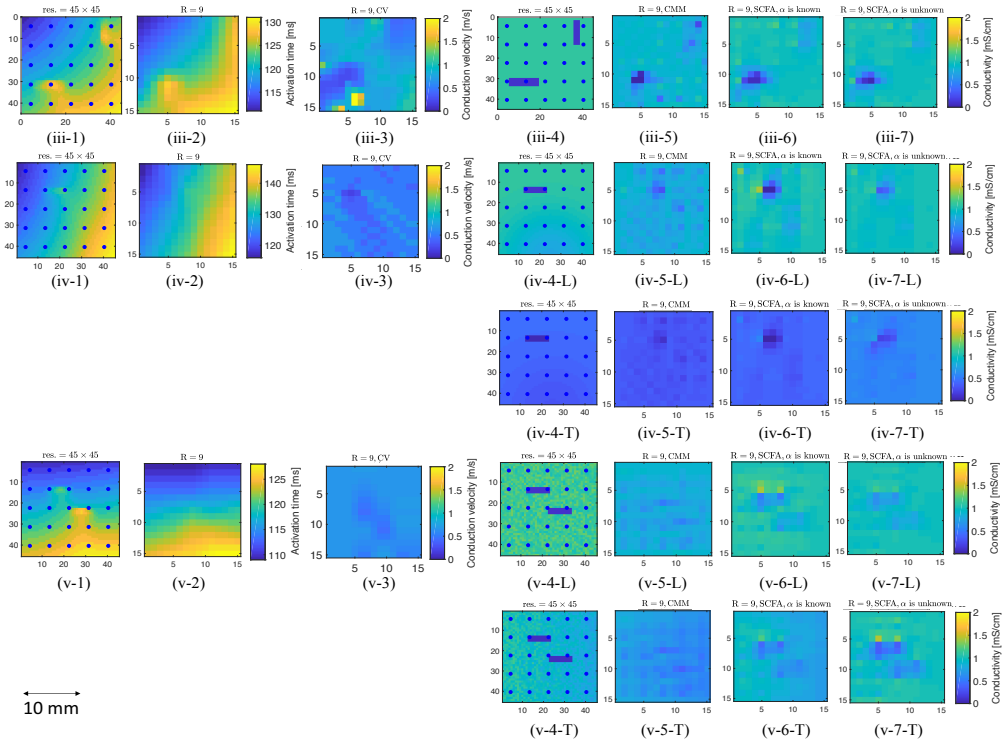


Figure 4.8: Examples of real and estimated activation time maps and conductivity maps. In the first row, the subfigures (iii-1)/(iii-2) show the real estimated activation time maps with original resolution 45×45 and the estimated activation time map with resolution 15×15 using the steepest descent method, respectively; the subfigure (iii-3) shows the estimated conduction velocity (CV) map; the subfigures (iii-4)/(iii-5)/(iii-6)/(iii-7) show the real conductivity map, the estimated conductivity map using the CMM method when the anisotropy ratio α is known, the estimated conductivity map using the proposed SCFA method when α is known, and the estimated conductivity map using the proposed SCFA method when α is unknown for tissue type (iii), respectively. The subfigures (iv-1)/(iv-2) and (v-1)/(v-2) show the real and estimated activation time maps for tissue type (iv) and (v), respectively. The subfigures (iv-3) and (v-3) show the estimated CV maps for tissue type (iv) and (v), respectively. The subfigures (iv-4-L)/(iv-4-T), (iv-5-L)/(iv-5-T), (iv-6-L)/(iv-6-T), and (iv-7-L)/(iv-7-T) are the real and estimated longitudinal/transversal conductivity maps for tissue type (iv), and (v-4-L)/(v-4-T), (v-5-L)/(v-5-T), (v-6-L)/(v-6-T), and (v-7-L)/(v-7-T) are the real and estimated longitudinal/transversal conductivity maps for tissue type (v), respectively.

sensor self noise by setting the SNR at 50 dB. Table 4.3 lists the estimation error for different types of tissue obtained by the proposed SCFA method and the CMM method, respectively. It can be seen that SCFA performs better than CMM in all scenarios even when CMM uses the true α and SCFA estimates α , which implies that using spatial information of the multi-electrode data helps to improve estimation of the conductivity. The performance of the methods degrades a little bit when the EGMs are disturbed by the noise. Figure 4.8 shows the real activation time maps, the estimated activation time maps estimated by the steepest descent approach followed by linear interpolation, the estimated conduction map, the real conductivity maps and the conductivity maps estimated by the CMM method with a known α and estimated by the SCFA method with known and estimated α when there is no noise. Compared to CMM, the proposed method localizes the conduction block more accurate and estimates the conductivities of the tissue regions outside the conduction blocks better. We also find that the higher resolution captures the underlying structure better, which further results in better estimation results. The CV maps only indicate the fast and slow conduction areas, which are not accurate compared to the other two methods and cannot estimate tissue conductivity and infer electropathology in tissue.

4

4.5. EXPERIMENTS ON CLINICAL DATA

In this section we evaluate the performance of the proposed method on clinical data. The data originate from epicardial EGMs measured from human atria during open-heart surgery using a high-resolution mapping approach [17]. The study protocol was approved in February 2010 by the Medical Ethics Committee (2010-054) in the Erasmus Medical Center, Rotterdam, The Netherlands. A mapping array of 8×24 electrodes with an inter-electrode distance of 2 mm is used for data collection. The array measures epicardial EGMs during sinus rhythm and during induced atrial fibrillation at each site. The acquired EGMs are amplified, filtered (bandwidth 0.5-400 Hz), sampled (1 kHz), and analogue to digital converted (16 bits). For more details on the mapping approach and the electrode array we refer to [17]. The far field artefacts and ventricular activities in the EGMs are cancelled using the method in [39].

Before estimating the tissue conductivity, we need to discretize tissue into groups of cells as introduced in Section 4.3.4. More concretely, the tissue under the mapping array is first discretized into $M_x \times M_y = 8 \times 24$ equal square areas of 2 mm by 2 mm each and each area is discretized into $Z_x \times Z_y = 3 \times 3$ cell groups. Then the spatial resolution of the tissue is $N_x \times N_y = 24 \times 72$. Each electrode is assumed to be at the center of the square area. To reduce the computation cost, we took a smaller tissue area with 5×5 electrodes in each estimation and the cell groups to be estimated is $N_x \times N_y = 15 \times 15$.

The activation times of the cells are estimated using the steepest descent approach with interpolation, similar as done in the simulated data. After computing the activation times of the cells, we use the proposed method to estimate the tissue conductivity. Since there is no ground truth of the tissue conductivity, we compare the estimated conductivity parameters to the experimentally determined conductivity values reported in the literature [8, 40]. However, the experimental results in the literature are inconsistent so far. To further demonstrate the performance of the proposed method, we also compare the real EGMs to the EGMs reconstructed using the estimated conductivity. The recon-

Table 4.4: Reconstruction errors of clinical EGMs using different methods

Methods	Patient 1	Patient 2	Patient 3	Patient 4	Patient 5
CMM	2.7848	2.5707	2.8315	2.9595	3.2666
SCFA	2.6517	2.4129	2.7994	2.7911	3.0880

struction error is calculated by

$$\text{Err}_{\text{rec}} = \frac{1}{M} \sum_1^M \|\mathbf{y}_m - \hat{\mathbf{y}}_m\|_2, \quad (4.36)$$

where \mathbf{y}_m and $\hat{\mathbf{y}}_m$ respectively represent the real and the estimated atrial EGM segments during atrial activity, and $\|\cdot\|_2$ represents the l_2 -norm of a vector.

We compare the performance of the proposed method with the CMM method proposed in [19]. Since the anisotropy ratio is unknown and cannot be estimated by the CMM method, we just fix it to one as which has been done in [19]. Table 4.4 shows the reconstructed errors of the EGMs of five patients. We can see that the proposed method achieves better performance than the CMM method. We show an example of the estimation on the clinical data in Figure 4.9. The estimated activation time map is plotted in 4.9 (a). The estimated conductivity map in the longitudinal and the transverse directions which are obtained by the proposed method are plotted in Figure 4.9 (b) and Figure 4.9 (c), respectively. The estimated anisotropy ratio map obtained by the proposed method is plotted Figure 4.9 (d). The estimated conductivity map obtained by the CMM method is plotted in Figure 4.9 (e). Examples of the real and the reconstructed EGMs obtained by the proposed method and the CMM method are shown in Figure 4.9 (f). In Figure 4.9 (b), (c), and (e), the estimated conductivities outside the conduction block vary from 0.84 mS/cm to 1.66 mS/cm, 0.38 mS/cm to 0.95 mS/cm, and 0.48 mS/cm to 0.88 mS/cm, respectively, which are in line with the values reported in the literature [8, 40]. The anisotropy ratio in Figure 4.9 (d) varies from 0.30 to 0.69. From Figure 4.9 (f) we see that the reconstructed EGMs are relatively similar to the original EGMs, in particular when only single deflections are present. Compared to the CMM method, the reconstructed EGMs fit the original EGMs better, which further validates the performance of the proposed method.

4.6. CONCLUSIONS AND DISCUSSIONS

In this work we proposed to estimate the tissue conductivity using the cross power spectrum of the multi-electrode EGMs in combination with the confirmatory factor analysis (CFA). Based on the fact that the conductivity parameters are shared among multiple frequencies, we proposed the simultaneous CFA (SCFA) to estimate the parameters of interest in the cross power spectral density matrix model. With SCFA, we are able to determine the resolution that we can obtain with a given number of electrodes. Compared to traditional CFA, SCFA needs less sensors to obtain the same resolution. Experiments on simulated data and clinical data demonstrate that SCFA obtains good estimation of the tissue conductivity.

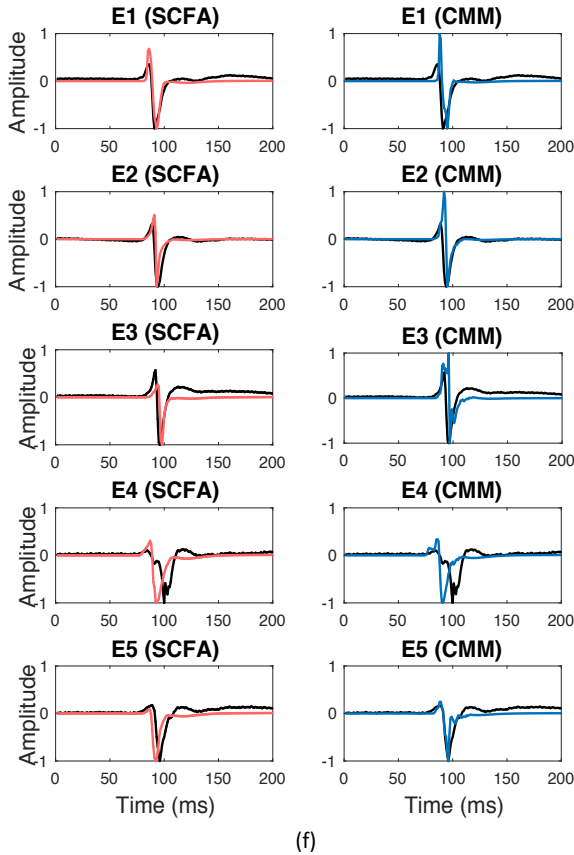
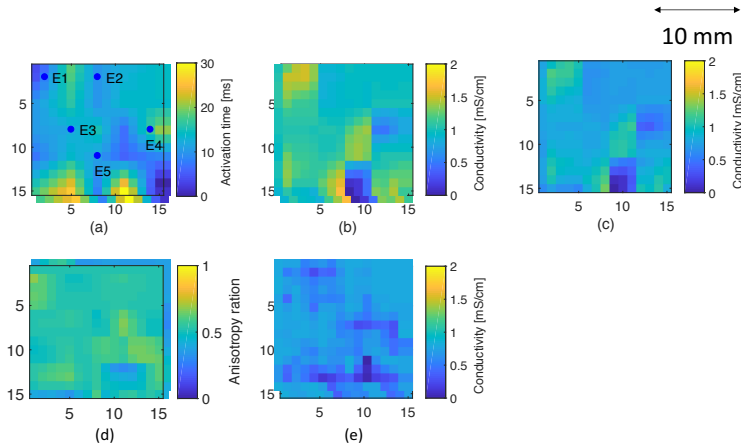


Figure 4.9: An example of the estimation on clinical data. (a) Estimated activation time map. Five blue points represent five electrodes. (b) and (c) Estimated conductivity maps in the longitudinal and the transverse direction by the proposed SCFA method, respectively. (d) Estimated anisotropy ratio map by the proposed SCFA method. The estimated longitudinal conductivity and the anisotropy ratio are used to calculate the transverse conductivity; (e) Estimated conductivity map by the CMM method; (f) Examples of the real (black) and the reconstructed (red/blue) EGMs at the five electrode positions marked in (a).

In this work, several assumptions are made to simplify the problem, which comes with some limitations. For example, we assume a fixed stereotype waveform for all cells although the action potential waveforms are possibly heterogeneous. For example, in the areas of compromised conductivity the upstroke may be slow. Also, we considered two-dimensional tissue which is more appropriate for thin-walled tissues, and assumed the conductivity tensors are aligned along the axes, which cannot model the curved paths of the fibre and the diseased atria with potential dissociation of endo-/epicardial layer. These assumptions reduce the accuracy of the EGM model, but they help to simplify the problem and reduce the computational cost for the estimation. The experiments that account for both isotropic and anisotropic propagation also demonstrate the robustness of the proposed method. We would like to improve the model in the near future, taking into account more realistic conditions, while reducing the computational cost for estimating the parameters.

Previous research has shown that alterations of atrial conduction is related to multiple cardiovascular diseases, such as atrial fibrillation, atrial fibrosis, atrial enlargement, etc. The potential applications of this model can be automated detection of the areas of bad conduction that possibly need to be ablated in an ablation operation to deal with atrial fibrillation, or staging of the abnormalities of the arrhythmias.

REFERENCES

- [1] C. D. Cantwell, C. H. Roney, F. S. Ng, *et al.*, *Techniques for automated local activation time annotation and conduction velocity estimation in cardiac mapping*, *Computers in Biology and Medicine* **65**, 229 (2015).
- [2] M. S. van Schie, A. Heida, Y. J. H. J. Taverne, *et al.*, *Identification of local atrial conduction heterogeneities using high-density conduction velocity estimation*, *Europace*, euab088 (2021).
- [3] N. Mazeh, D. E. Haines, M. W. Kay, and B. J. Roth, *A simplified approach for simultaneous measurements of wavefront velocity and curvature in the heart using activation times*, *Cardiovascular Engineering and Technology* **4**, 520 (2013).
- [4] A. G. Kléber and Y. Rudy, *Basic mechanisms of cardiac impulse propagation and associated arrhythmias*, *Physiological Reviews* (2004).
- [5] F. M. Weber *et al.*, *Conduction velocity restitution of the human atrium -an efficient measurement protocol for clinical electrophysiological studies*, *IEEE Transactions on Biomedical Engineering* **58**, 2648 (2011).
- [6] C. T. January, L. S. Wann, J. S. Alpert, *et al.*, *2014 AHA/ACC/HRS guideline for the management of patients with atrial fibrillation: a report of the American College of Cardiology/American Heart Association Task Force on Practice Guidelines and the Heart Rhythm Society*, *Journal of the American College of Cardiology* **64**, e1 (2014).
- [7] R. Plonsey and R. C. Barr, *Bioelectricity: a quantitative approach* (Springer Science & Business Media, 2007).

- [8] R. H. Clayton, O. Bernus, E. M. Cherry, *et al.*, *Models of cardiac tissue electrophysiology: progress, challenges and open questions*, *Progress in Biophysics and Molecular Biology* **104**, 22 (2011).
- [9] C. S. Henriquez, *A brief history of tissue models for cardiac electrophysiology*, *IEEE Transactions on Bio-medical Engineering* **61**, 1457 (2014).
- [10] B. M. Johnston and P. R. Johnston, *Approaches for determining cardiac bidomain conductivity values: progress and challenges*, *Medical & Biological Engineering & Computing*, 1 (2020).
- [11] M. Bazhenov, P. Lonjers, S. Skorheim, *et al.*, *Non-homogeneous extracellular resistivity affects the current-source density profiles of up-down state oscillations*, *Philosophical Transactions of the Royal Society A: Mathematical, Physical and Engineering Sciences* **369**, 3802 (2011).
- [12] S. Dokos and N. H. Lovell, *Parameter estimation in cardiac ionic models*, *Progress in Biophysics and Molecular Biology* **85**, 407 (2004).
- [13] E. Gilboa, P. S. La Rosa, and A. Nehorai, *Estimating electrical conductivity tensors of biological tissues using microelectrode arrays*, *Annals of Biomedical Engineering* **40**, 2140 (2012).
- [14] C. Bédard and A. Destexhe, *Generalized theory for current-source-density analysis in brain tissue*, *Physical Review E* **84**, 041909 (2011).
- [15] S. Neukom, A. Maccione, Y. Bornat, *et al.*, *Large-scale, high-resolution data acquisition system for extracellular recording of electrophysiological activity*, *IEEE Transactions on Biomedical Engineering* **55**, 2064 (2008).
- [16] L. Berdondini, K. Imfeld, A. Maccione, *et al.*, *Active pixel sensor array for high spatio-temporal resolution electrophysiological recordings from single cell to large scale neuronal networks*, *Lab on a Chip* **9** (2009).
- [17] A. Yaksh, L. J. M. E. van der Does, *et al.*, *A novel intra-operative, high-resolution atrial mapping approach*, *Journal of Interventional Cardiac Electrophysiology* **44**, 221 (2015).
- [18] L. S. Graham and D. Kilpatrick, *Estimation of the bidomain conductivity parameters of cardiac tissue from extracellular potential distributions initiated by point stimulation*, *Annals of Biomedical Engineering* **38**, 3630 (2010).
- [19] B. Abdi, R. C. Hendriks, A.-J. van der Veen, and N. M. de Groot, *A compact matrix model for atrial electrograms for tissue conductivity estimation*, *Computers in Biology and Medicine* **107**, 284 (2019).
- [20] N. Virag, V. Jacquemet, C. S. Henriquez, *et al.*, *Study of atrial arrhythmias in a computer model based on magnetic resonance images of human atria*, *Chaos: An Interdisciplinary Journal of Nonlinear Science* **12**, 754 (2002).

- [21] S. Pezzuto, P. Kal'avský, M. Potse, *et al.*, *Evaluation of a rapid anisotropic model for ecg simulation*, *Frontiers in Physiology* **8** (2017).
- [22] T. A. Brown and M. T. Moore, *Confirmatory factor analysis*, *Handbook of Structural Equation Modeling*, 361 (2012).
- [23] D. N. Lawley and A. E. Maxwell, *Factor analysis as a statistical method*, *Journal of the Royal Statistical Society. Series D (The Statistician)* **12**, 209 (1962).
- [24] K. G. Jöreskog, *A general approach to confirmatory maximum likelihood factor analysis*, *Psychometrika* **34**, 183 (1969).
- [25] K. G. Jöreskog and D. N. Lawley, *New methods in maximum likelihood factor analysis*, *British Journal of Mathematical and Statistical Psychology* **21**, 85 (1968).
- [26] A. I. Koutrouvelis, R. C. Hendriks, R. Heusdens, *et al.*, *Robust joint estimation of multimicrophone signal model parameters*, *IEEE/ACM Transactions on Audio, Speech, and Language Processing* **27**, 1136 (2019).
- [27] B. M. Johnston and P. R. Johnston, *Determining six cardiac conductivities from realistically large datasets*, *Mathematical Biosciences* **266**, 15 (2015).
- [28] M. Potse, B. Dubé, J. Richer, *et al.*, *A comparison of monodomain and bidomain reaction-diffusion models for action potential propagation in the human heart*, *IEEE Transactions in Biomedical Engineering* **53**, 2425 (2006).
- [29] B. F. Nielsen, T. S. Ruud, G. T. Lines, and A. Tveito, *Optimal monodomain approximations of the bidomain equations*, *Applied Mathematics and Computation* **184**, 276 (2007).
- [30] Y. Coudière, Y. Bourgault, and M. Rioux, *Optimal monodomain approximations of the bidomain equations used in cardiac electrophysiology*, *Mathematical Models and Methods in Applied Sciences* **24**, 1115 (2014).
- [31] D. Gabor, *Theory of communication. part 1: The analysis of information*, *Journal of the Institution of Electrical Engineers-Part III: Radio and Communication Engineering* **93**, 429 (1946).
- [32] M. R. Courtemanche, R. J. Ramirez, and S. Nattel, *Ionic mechanisms underlying human atrial action potential properties: insights from a mathematical model*, *American Journal of Physiology-Heart and Circulatory Physiology* **275**, H301 (1998).
- [33] C. D. Cantwell, C. H. Roney, F. S. Ng, J. H. Siggers, S. J. Sherwin, and N. S. Peters, *Techniques for automated local activation time annotation and conduction velocity estimation in cardiac mapping*, *Computers in Biology and Medicine* **65**, 229 (2015).
- [34] C. Gabriel, S. Gabriel, and E. Corthout, *The dielectric properties of biological tissues: I. literature survey*, *Physics in Medicine & Biology* **41**, 2231 (1996).
- [35] R. H. Byrd, M. E. Hribar, and J. Nocedal, *An interior point algorithm for large scale nonlinear programming*, *SIAM Journal on Optimization* **9** (1999).

- [36] R. A. Waltz, J. L. Morales, J. Nocedal, and D. Orban, *An interior algorithm for non-linear optimization that combines line search and trust region steps*, *Mathematical Programming* **107**, 391 (2006).
- [37] R. H. Byrd, J. C. Gilbert, and J. Nocedal, *A trust region method based on interior point techniques for nonlinear programming*, *Mathematical Programming* **89**, 149 (2000).
- [38] G. Salama, A. Kanai, and I. R. Efimov, *Subthreshold simulation of purkinje fibers interrupts ventricular tachycardia in intact hearts*, *Circulation Research* **74**, 604 (1994).
- [39] M. Sun, E. Isufi, N. M. de Groot, and R. C. Hendriks, *Graph-time spectral analysis for atrial fibrillation*, *Biomedical Signal Processing and Control* **59** (2020).
- [40] M. J. Barbara and R. J. Peter, *Approaches for determining cardiac bidomain conductivity values: progress and challenges*, *Medical & Biological Engineering & Computing* **58**, 2919 (2020).

5

JOINT CARDIAC TISSUE CONDUCTIVITY AND ACTIVATION TIME ESTIMATION USING CONFIRMATORY FACTOR ANALYSIS

MATHEMATICAL models of the electrophysiology of cardiac tissue play an important role when studying heart rhythm disorders like atrial fibrillation. Model parameters such as conductivity, activation time, and anisotropy ratio are useful parameters to determine the arrhythmogenic substrate that causes abnormalities in the atrial tissue. Existing methods often estimate the model parameters separately and assume some of the parameters to be known as a priori knowledge. In this work, we propose an efficient method to jointly estimate the parameters of interest from the cross power spectral density matrix (CPSDM) model of the electrograms. By applying confirmatory factor analysis (CFA) to the CPSDMs of multi-electrode electrograms, we can make use of the spatial information of the data and analyze the relationship between the desired resolution and the required amount of data. With the reasonable assumptions that the conductivity parameters and the anisotropy parameters are constant across different frequencies and heart beats, we estimate these parameters using multiple frequencies and multiple heart beats simultaneously to easier satisfy the identifiability conditions in the CFA problem. Results on the simulated data show that using multiple heart beats decreases the estimation errors of the conductivity and the estimated activation time parameters. The experimental results on clinical data show that using multiple heart beats for parameter estimation can reduce the reconstruction errors of the clinical electrograms, which further demonstrates the robustness of the proposed method.

This chapter is based on the paper published as "Joint cardiac tissue conductivity and activation time estimation using confirmatory factor analysis" by M. Sun, N. M. S. de Groot, and R. C. Hendriks, *Computers in Biology and Medicine*, vol. 144, 2022.

5.1. INTRODUCTION

Mathematical modeling of the electrophysiological properties of atrial tissue could play an important role in understanding atrial fibrillation and detecting the underlying arrhythmogenic substrate. Being able to accurately determine the model parameters such as the cell conductivity, the anisotropy ratio of the conductivity and the cell's activation time from measurements is at least as important to be able to investigate the cause of cardiac arrhythmias and localize the arrhythmogenic substrate in the tissue. In Chapter 4, we have proposed the use of an efficient method called confirmatory factor analysis (CFA) to jointly estimate a subset of these parameters, that are the tissue conductivity and the anisotropy ratio from electrograms. By analyzing the identifiability conditions in the formulated CFA problem, we find the relation between the required amount of data and the desired resolution. However, the method presented in Chapter 4 was limited to the use of a single heart beat and could only estimate the conductivity and the anisotropy parameters. In this chapter, we further extend this algorithm to jointly estimate the conductivity, anisotropy ratio, as well as the activation time per cell using multiple heart beats and multiple frequencies by using the proposed method called simultaneous CFA.

CFA has been widely used to test whether the data fits a hypothesized measurement model that captures the variance-covariance structures of the measurements [1]. In Chapter 4, we have applied CFA to the cross-power spectral density (CPSDM) model of the measurements to estimate the conductivity parameters and the anisotropy ratio parameters. In order to easier satisfy the identifiability conditions, we assumed that the conductivity parameters and the anisotropy ratio parameters are constant across several frequencies and proposed SCFA using multiple temporal frequencies of a single heart beat. The activation time parameters were assumed to be known and were in the end estimated by the steepest descent method, as described in [2], before estimating the conductivity.

In this chapter, we propose a more efficient SCFA method to jointly estimate more model parameters from epicardial electrograms. It is based on the fact that the propagation of the electrical wave in the tissue might change its direction slightly from one heart beat to another, even during sinus rhythm (SR). Multiple of these heart beats then "illuminate" the tissue from (slightly) different directions and provide additional and different data that could facilitate the parameter estimation. Taking this into account, we further make use of multiple heartbeats to improve the parameter estimation. Since the conductivity and the anisotropy ratio parameters are roughly constant in different frequencies and different heart beats, we estimate these parameters across multiple frequencies and heart beats to increase the ratio between the number of equations and the number of unknown parameters in the SCFA problem. However, note that the activation time parameters will change across different heart beats and are therefore estimated per heart beat. In order to utilize the spatial structure of the multi-electrode data, the proposed algorithm is based on the CPSDM model. Extra constraints that incorporate prior knowledge on the model parameters are used to reduce the feasibility set of the parameter space and therefore increase the robustness of the algorithm.

Altogether, this chapter makes more efficient use of the data than chapter 4 and further improves the CFA approach for jointly estimating cardiac tissue parameters. More concretely, the contributions of this chapter are: (i) to not only jointly estimate the tissue

conductivity and anisotropy ratio parameters by solving a CFA problem as in Chapter 4, but also to jointly estimate the cell activation time; (ii) estimating the parameters simultaneously in multiple frequencies and multiple heart beats instead of using a single heart beat. This helps to: (1) improve the performance by making use of the information provided by multiple heart beats; (2) update the values of the activation time, the conductivity and the anisotropy ratio parameters simultaneously in the estimation to increase the estimation accuracy of these parameters; (3) increase the ratio of known and unknown parameters such that a higher spatial resolution of parameters can be obtained given the same amount of data. The rest of the chapter is organized as follows. In Section 5.2.1, we briefly review the impulse response model the CPSDM model of EGMs, and the problem formulation for the joint model parameter estimation. In Section 5.3, we review the basic CFA theory and introduce the proposed SCFA algorithm and practical consideration to increase the robustness of the proposed algorithm. In Section 5.4 and Section 5.5, we evaluate the proposed algorithm using simulated data and clinical data, respectively. In Section 5.6, we discuss the advantages and the limitations of this work and draw the conclusions.

5.2. PRELIMINARIES

5.2.1. ELECTROGRAM MODELS

In this section, we review the epicardial electrogram models in the time domain and the frequency domain, respectively. To model the electrical propagation in epicardial tissue, we consider the cable theory and the monodomain approach, which assumes that the anisotropy ratios of the intracellular domain and the extracellular domain are equal. We consider M electrodes that are positioned on an epicardial area of the left/right atrium. The electrodes are indexed by $m \in \{1, 2, \dots, M\}$. To represent the electrograms measured by the electrodes in a computational model, we discretize the tissue into a two-dimensional grid with N regular elements to model N cells. We use $r_{m,n}$ to denote the distance between the m th electrode and the n th cell and let $\mathbf{r}_m = \left[\frac{1}{r_{m,0}}, \frac{1}{r_{m,1}}, \dots, \frac{1}{r_{m,N-1}} \right]^T$. As introduced in Chapter 4, the atrial electrogram recorded by the m th electrode can be modeled as [ref. Eq. (4.13) and Eq. (4.24)]

$$y_m(t) = Q\mathbf{r}_m^T \mathbf{D}_{\sigma,\alpha} \boldsymbol{\delta}_\tau(t) * v_0(t). \quad (5.1)$$

where Q is a constant parameter, $\mathbf{D}_{\sigma,\alpha} \equiv \mathbf{D}_\sigma$ is the double differentiation operator, and $\boldsymbol{\delta}_\tau(t) = [\delta(t - \tau_0), \delta(t - \tau_1), \dots, \delta(t - \tau_{N-1})]^T$ with τ_n the time delay of the n th cell with respect to the reference cell [ref. Eq. (4.13)]. This can be further simplified as

$$y_m(t) = a_m(t) * v_0(t), \quad (5.2)$$

with $a_m(t) = Q\mathbf{r}_m^T \mathbf{D}_{\sigma,\alpha} \boldsymbol{\delta}_\tau(t)$ the impulse response from all cells to the sensor at position m . Denoting the noise received at the m th electrode by $u_m(t)$, the noisy atrial electrogram measured by the m th electrode is given by

$$y_m(t) = a_m(t) * v_0(t) + u_m(t). \quad (5.3)$$

The time domain electrogram model can be written in the frequency domain using the STFT. Let $l = 1, \dots, L$ denote the time-frame index and $k = 1, \dots, K$ denote the

frequency-bin index. In the frequency domain, the electrogram model from (5.3) is then given by

$$\tilde{y}_m(l, k) = \tilde{a}_m(l, k)\tilde{v}_0(l, k) + \tilde{u}_m(l, k) \quad (5.4)$$

where $\tilde{y}_m(l, k)$, $\tilde{a}_m(l, k)$, $\tilde{v}_0(l, k)$, and $\tilde{u}_m(l, k)$ are the STFT coefficients of $y_m(t)$, $a_m(t)$, $v_0(t)$, and $u_m(t)$, respectively. In this chapter, we consider to use multiple frequencies and multiple time frames for parameter estimation. The set of the frequency indices used for estimation is denoted by S_f and the number of the elements in S_f is $|S_f|$. The set of the used time frames is denoted by S_l and the number of the elements in S_l is $|S_l|$. As introduced in Chapter 4, the cross power spectral density matrix (CPSDM) of the electrograms in the l th frame and the k th frequency bin can be expressed as [ref. Eqs. (4.16) - (4.22)]

$$\begin{aligned} \Phi_{\mathbf{y}}(l, k) &= E[\tilde{\mathbf{y}}(l, k)\tilde{\mathbf{y}}(l, k)^H] \\ &= \phi(l, k)\tilde{\mathbf{a}}(l, k)\tilde{\mathbf{a}}(l, k)^H + \Phi_{\mathbf{u}}(l, k), \end{aligned} \quad (5.5)$$

where

$$\tilde{\mathbf{a}}(l, k) = [Q\mathbf{r}_1^T \mathbf{D}_{\sigma, \alpha} \tilde{\boldsymbol{\delta}}(l, k), \dots, Q\mathbf{r}_M^T \mathbf{D}_{\sigma, \alpha} \tilde{\boldsymbol{\delta}}(l, k)]^T \quad (5.6)$$

with

$$\tilde{\boldsymbol{\delta}}_{\tau}(l, k) = [\exp(-j\frac{2\pi f_s k}{K}\tau_0(l)), \dots, \exp(-j\frac{2\pi f_s k}{K}\tau_{N-1}(l))]^T, \quad (5.7)$$

and where $\phi(l, k) = E[\tilde{v}_0^2(l, k)]$ is the power spectral density of the reference cell, and $\Phi_{\mathbf{u}}(l, k) = \text{Diag}([q_1, \dots, q_M]^T)$ with the m th diagonal element $q_m = E[\tilde{u}_m^2(l, k)]$ the power spectral density of the sensor-self noise of the m th sensor, which is assumed to be uncorrelated across sensors, across time and across frequency bins. Since the time delays of the cells vary across heart beats, $\tau_n(l)$ in Eq. (5.7) for the l th time frame is relative to $\tau_0(l)$.

For the CPSDM model, the unknown parameters of interest, i.e., $\boldsymbol{\sigma}$ and $\boldsymbol{\alpha}$ are included in the spatial operator $\mathbf{D}_{\sigma, \alpha}$ in $\tilde{\mathbf{a}}(l, k)$ [ref. Eq. (4.24)], and the activation time parameters τ_n for all $n = 0, \dots, N-1$ are included in $\tilde{\boldsymbol{\delta}}(l, k)$ in $\tilde{\mathbf{a}}(l, k)$.

5.2.2. PROBLEM FORMULATION

The goal of this work now is to jointly estimate the conductivity parameters $\boldsymbol{\sigma}$, the anisotropy ratio parameters $\boldsymbol{\alpha}$, and the activation time parameters τ_n for all $n = 0, \dots, N-1$ from the noisy CPSDM matrices $\Phi_{\mathbf{y}}(l, k)$, estimated from the electrograms of multiple heart beats for all time frames.

In this problem, the number of knowns depends on the number of electrodes used for data measurements and the number of unknowns depends on the number of cells (modeled by the spatial grid elements of the tissue) given a certain number of electrodes. To make the problem solvable, the number of knowns needs to be larger than the number of unknowns. This can be confirmed by analyzing the identifiability conditions of the confirmatory factor analysis (CFA) problem. Next, we will use CFA to analyze the resolution that we can obtain with the given amount of data and estimate the target parameters.

5.3. SIMULTANEOUS CONFIRMATORY FACTOR ANALYSIS FOR JOINT ESTIMATION OF TISSUE PROPERTIES

CFA has been proposed to estimate parameters to fit a hypothesized measurement model based on variance-covariance structures of the data, which can be applied to estimate the parameters in CPSDM models. Interested readers are referred to the studies in [3–6] for more details. Generally, solving the CFA problem is done by minimizing the distance between the estimated CPSDMs of the noisy measurements and the theoretical CPSDMs with respect to some free parameters while keeping the remaining parameters fixed at the given values. In most cases, this implies to solve an optimization problem with constraints to incorporate a priori knowledge of the models and parameters.

Two necessary conditions have been proposed to ensure the parameters of the CPSDM model are uniquely identifiable [6]. The *first identifiability condition* is that the number of equations should be larger than the number of unknown parameters. The number of equations depend on the given amount of data. In this problem, it depends on the number of electrodes M used in the measurement. For guaranteeing unique identifiability, the *first identifiability condition* is not enough and the *second identifiability condition* is needed. This condition states the number of parameters in the CPSDM model that at least need to be fixed to have a unique solution.

5.3.1. SIMULTANEOUS CFA PROBLEM FOR JOINT ESTIMATION IN MULTIPLE FREQUENCIES AND MULTIPLE HEART BEATS

In [7], we have adapted the CFA method to estimate the cardiac tissue conductivity parameters and the anisotropy ratio parameters from the CPSDM model using a single heart beat. We now apply the CFA to estimate parameters of interest in this work, i.e., the conductivity, anisotropy ratio, and activation time parameters from the CPSDM model in (5.5) using multiple heart beats. To increase the robustness of the estimation, we put some constraints on the parameters exploiting some a priori knowledge. The power spectral density of the reference cell ϕ is fixed by a known constant $\hat{\phi}$. The Courtemanche model proposed in [8] is considered here to simulate multiple realizations of the action potential of a atrial cell to estimate ϕ . For the reference cell with index zero, the activation time $\tau_0(l) = 0$ for all heart beats (i.e., for all l). Based on the assumption that the conductivity σ , the anisotropy ratio α and the activation time τ_n in different frequencies are roughly constant, we estimate these parameters simultaneously in multiple frequencies to increase the ratio of known-to-unknown variables when estimating the conductivity parameters using CPSDMs of noisy atrial electrograms.

Moreover, we take into account multiple heart beats, since the conductivity σ and the anisotropy ratio α can also be assumed constant across multiple heart beats. Therefore, by increasing the number of heart beats, the number of unknowns due to σ and α does not increase. The *first identifiability condition* can be easier satisfied, and the estimation error may be further reduced since waves coming from varying directions illuminate the tissue from various viewpoints. Note that the activation time parameters are constant across frequencies but differ across heart beats. Therefore, when increasing the number of heart beats for estimation, the number of unknowns due to τ_n will increase. In addition, the number of unknowns due to $\Phi_{\mathbf{u}}$ will also increase when increasing the number

of heart beats. Taking these analyses into account, the simultaneous CFA (SCFA) problem formulation to jointly estimate the parameters in multiple frequencies and multiple heart beats is given by

$$\begin{aligned}
 & \min_{\substack{\sigma, \alpha, \Phi_{\mathbf{u}}(k, l), \\ \{\tau_n(l), n=0, \dots, N-1\}}} \sum_{\forall k \in S_f, \forall l \in S_l} F(\hat{\Phi}_{\mathbf{y}}(k, l), \Phi_{\mathbf{y}}(k, l)) \\
 \text{s.t. } & \Phi_{\mathbf{y}}(k, l) = \tilde{\mathbf{a}}(k, l)\phi(k, l)\tilde{\mathbf{a}}(k, l)^H + \Phi_{\mathbf{u}}(k, l), \forall k \in S_f, \forall l \in S_l \\
 & \tilde{\mathbf{a}}(k, l) = [Q\mathbf{r}_1^T \mathbf{D}_{\sigma, \alpha} \tilde{\boldsymbol{\delta}}(k, l), \dots, Q\mathbf{r}_M^T \mathbf{D}_{\sigma, \alpha} \tilde{\boldsymbol{\delta}}(k, l)]^T, \forall k \in S_f, \forall l \in S_l \\
 & \mathbf{D}_{\sigma, \alpha} = \mathbf{D}_{x, L} \text{Diag}(\boldsymbol{\sigma}) \mathbf{D}_{x, R} + \mathbf{D}_{y, L} \text{Diag}(\boldsymbol{\alpha}) \text{Diag}(\boldsymbol{\sigma}) \mathbf{D}_{y, R}, \\
 & \tilde{\boldsymbol{\delta}}_{\tau}(k, l) = [\exp(-\frac{j2\pi f_s k}{K} \tau_0(l)), \dots, \exp(-\frac{j2\pi f_s k}{K} \tau_{N-1}(l))], \forall k \in S_f, \forall l \in S_l, \\
 & \Phi_{\mathbf{u}}(k, l) = \text{Diag}[q_1(k, l), q_2(k, l), \dots, q_M(k, l)], \forall k \in S_f, \forall l \in S_l \tag{5.8} \\
 & q_m(k, l) \geq 0, m = 1, 2, \dots, M, \forall k \in S_f, \forall l \in S_l, \\
 & \phi(k, l) = \hat{\phi}(k, l), \forall k \in S_f, \forall l \in S_l, \\
 & \mathbf{0} < \boldsymbol{\alpha} \leq \boldsymbol{\alpha}_{\text{upper}}, \\
 & \mathbf{0} \leq \boldsymbol{\sigma} \leq \boldsymbol{\sigma}_{\text{upper}}, \\
 & \tau_0(l) = 0, \forall l \in S_l, \\
 & \tau_{\text{low}} \leq \tau_n(l) \leq \tau_{\text{upper}}, n = 1, \dots, N-1, \forall l \in S_l,
 \end{aligned}$$

where $F(\hat{\Phi}_{\mathbf{y}}, \Phi_{\mathbf{y}})$ is a cost function such as the maximum likelihood, least square, or generalized least square, and where the constraints are used to incorporate model knowledge, for example the a priori knowledge from (5.5) and incorporating the knowledge that $\Phi_{\mathbf{u}}$ is diagonal and positive definite. Constraints are also put on the target parameters, which are expressed by the last four constraints in (5.8), where $\boldsymbol{\alpha}_{\text{upper}}$ and $\boldsymbol{\sigma}_{\text{upper}}$ are real valued upper bounds on the anisotropy ratio and conductivity parameters which are selected based on the previous research on these parameters of atrial tissue, and τ_{low} and τ_{upper} are respectively the lower and upper bounds of activation time that are set by reasonable values. For the loss function in (5.8), we consider to use the least square cost function, which is given by

$$F(\hat{\Phi}_{\mathbf{y}}, \Phi_{\mathbf{y}}) = \frac{1}{2} \|\hat{\Phi}_{\mathbf{y}} - \Phi_{\mathbf{y}}\|_F^2, \tag{5.9}$$

for $\forall k \in S_f, \forall l \in S_l$. Note that the problem in (5.8) is not convex and may have multiple local minima.

5.3.2. IDENTIFIABILITY CONDITIONS OF THE SCFA PROBLEM

Prior to estimating the target parameters in this CFA problem, we first analyze what resolution we can obtain given M electrodes. This can be achieved by analyzing the two identifiability conditions of the SCFA problem. To analyze whether the *first identifiability condition* is satisfied, we need to calculate the number of knowns and unknowns in (5.8). Since the noisy CPSDM estimated for M electrodes in one frequency band and one heart beat is symmetric, there are M^2 real valued knowns due to $\Phi_{\mathbf{y}}(k, l)$ in total. When considering $|S_f|$ frequency bands and $|S_l|$ heart beats, the number of knowns due

to the noisy CPSDMs of M electrodes in $|S_f|$ frequency bands and $|S_l|$ heart beats is $|S_l||S_f|M^2$. The number of unknowns due to σ in \mathbf{D}_σ is N , due to α in \mathbf{D}_σ is N , due to $\tau_n(l)$ ($n = 1, \dots, N-1$) is $|S_l|(N-1)$, and due to $\Phi_{\mathbf{u}}(l, k)$ is $|S_l||S_f|M$. Therefore, the *first identifiability condition* is

$$|S_l||S_f|M^2 \geq 2N + |S_l|(N-1) + |S_l||S_f|M, \quad (5.10)$$

which means that the number of cells N for which we can estimate the desired parameters is constrained by

$$N \leq \frac{|S_l||S_f|(M^2 - M) + |S_l|}{2 + |S_l|}. \quad (5.11)$$

We can see that using multiple frequencies or/and multiple heart beats, i.e., $|S_l| > 1$ or/and $|S_f| > 1$, the *first identifiability condition* can be satisfied with less sensors.

The *second identifiability condition* requires that at least r^2 parameters in $\tilde{\mathbf{a}}$ and ϕ in the CPSDM model in (5.5) need to be fixed, where r represents the number of sources that trigger the atrial activity in the cardiac tissue [7]. According to the *second identifiability condition*, we need r^2 independent restrictions on $\tilde{\mathbf{a}}$ and $\phi(l, k)$. In this work we consider only a single source, therefore $r^2 = 1$. Since we have fixed the value of ϕ in the constraint, the *second identifiability condition* is always satisfied.

5.3.3. PRACTICAL CONSIDERATION

Due to the large number of cells in the tissue, the *first identifiability condition* cannot be satisfied if we estimate parameters at the finest resolution, that is, estimating the parameters for each cell. To ease this problem we considered groups of cells and used the center cell of the group to represent the group.

Let N denote the number of cell groups and let R represent the resolution scale compared to the number of electrodes M , then $N = RM$. The *first identifiability condition* in (5.11) can be rewritten using R as

$$RM \leq \frac{|S_l||S_f|(M^2 - M) + |S_l|}{2 + |S_l|}. \quad (5.12)$$

which means that the highest resolution scale that can be obtained given M electrodes is

$$R = \frac{|S_l||S_f|(M^2 - M) + |S_l|}{(2 + |S_l|)M}. \quad (5.13)$$

By reducing the resolution scale R at which we estimate the parameters, that is, increasing the number of cells per group, we can reduce the number of unknowns and increase the ratio of the number of equations to the number of unknowns, which then satisfies easier the first identifiability condition. However, note that reducing the resolution scale R will reduce the model accuracy and increase the model-mismatch error compared to using the actual cells.

The parameters are finally obtained by solving the non-convex optimization problem in (5.8). In this work, we used the MATLAB optimization toolbox to solve this problem, which is based on a combination of the methods in [9–11].

5.4. EXPERIMENTS ON SIMULATED DATA

In this section, we evaluate the performance of the proposed methods on simulated data. We first introduce the data generation based on the mathematical model and then evaluate the joint estimation of the conductivity, anisotropy ratio, and activation time using one heart beat and multiple heart beats, respectively. The results of the proposed method are compared with our previously proposed SCFA method from [7], which assumed the activation time parameters were known and in the end were estimated by the steepest descent approach from [2] before conductivity estimation. For convenience, we use SCFA1 to represent the method in [7] and SCFA2 to represent the method proposed in this chapter.

5.4.1. GENERATION OF SIMULATED DATA

MODEL OF ATRIAL CELLS

To generate the atrial electrograms for evaluation, we first model individual cells and then integrated these cells to form the tissue. To generate realistic action potentials, properties and ionic mechanisms in atrial cells need to be considered in the computational cell model. In this work, we use the Courtemanche model proposed in [8] to model the atrial cells.

TYPES OF TISSUE

Two-dimensional tissues with different conductivity settings are considered in the simulations to test the performance, including three types of tissues:

- (i) inhomogeneous tissue with two areas of conduction block and the area outside the conduction block is homogeneous and isotropic with conductivity $\sigma_n = 1.1$ mS/cm for all α_n and $\alpha = 1$;
- (ii) inhomogeneous tissue with one area of conduction block and the area outside the conduction block has a smooth variation in conductivity, varying from 0.77 mS/cm to 1.1;
- (iii) inhomogeneous tissue with two areas of conduction block and the area outside the conduction block has a higher variation in conductivity than (ii) which varies from 0.75 mS/cm to 1.3 mS/cm and its anisotropic ratio α_n changes from 0.7 to 0.5 from left to right.

SIMULATION PROTOCOL

Tissues are discretized into 90×90 regular grid points to model the cells. The cell-to-cell distance is 0.02 cm. At the beginning, all the cells are at their resting status with the initial conditions as set in [8]. Then, a train of stimulus with a basic cycle length of 1000 ms is applied to the source cells in the tissue during 5 s. The stimulus current is $I_{st} = 200$ μA with a duration of 0.5 ms. Once the source cells are activated, they generate and conduct the impulses to their neighbors, causing the spread of excitation through the tissue. The electrical waves in different heart beats are assumed to be originating from slightly different directions, which is implemented by applying the stimulus at different positions of the tissue.

Table 5.1: Summary of parameters used in the experiments

Parameters	Definition	Value
T	time-frame length	1000 samples
ov_T	overlapping of time-frame	20%
K	FFT length	1000
f_s	sampling frequency	1 kHz
C	membrane capacity	$1 \mu\text{F}/\text{cm}^2$
S_v	cellular surface to volume ratio	$0.24 \mu\text{m}^{-1}$
σ_{upper}	maximum conductivity of a cell	2 mS/cm

CALCULATION OF ACTION POTENTIALS AND ELECTROGRAMS

The basic equation to calculate the transmembrane potentials of the cells is

$$C \frac{\partial v_n(t)}{\partial t} = I_{\text{tm},n}(t) + I_{\text{st},n}(t) - I_{\text{ion},n}(t, v_n(t)) \quad (5.14)$$

where $v_n(t)$ is the transmembrane potential of the n th cell, C is the membrane capacitance, $I_{\text{st},n}(t)$ is the stimulus current, $I_{\text{ion},n}(t, v(t))$ is the ionic current, and $I_{\text{tm},n}(t)$ is the cell-to-cell transmembrane current per unit area that accounts for the spatial evolution of the action potential. Since the electrical wave should not propagate further than the tissue boundaries, the no-flux boundary conditions is considered. After solving (5.14) using forward Euler's method with a time step of 0.05 ms, we obtain the action potential at every grid point of the tissue. The moment when the action potential of a cell reaches the threshold of -40 mV is considered as the cell's activation time. After calculating the action potentials of all cells, the electrograms are generated using the mathematical model in (4.5). The noisy electrograms are then generated by adding Gaussian noise to the clean electrograms to simulate sensor self noise. The signal-to-noise ratio (SNR) is set at 50 dB. In the experiments, we assume the fiber is aligned along the x-axis and choose $\alpha_{\text{upper}} = \mathbf{1}$. The values of other parameters used for the experiments are summarized in Table 5.1.

Figure 5.1 shows an example of the experimental setup, the generated electrograms and the activation time maps of the heart beats. Figure 5.1(a) shows tissue as having the two areas of conduction block with a 5×5 electrode array placed on the center of the tissue. The two blue lines represent the two areas of conduction block. The cells outside the areas of conduction block have a conductivity of 1.1 mS/cm. The nine red points numbered from one to nine represent the simulated source positions of the nine heart beats, respectively, where an external stimulus current of $I_{\text{st}} = 200 \mu\text{A}$ is applied to trigger the electrical activity in the tissue. Note that for each heart beat there is only one source to drive the propagation of the wave. Figure 5.1(b) plots the generated electrograms of the nine heart beats measured by the electrode array in Figure 5.1(a). We can see the small differences between these heart beats. Figure 5.1(c) and 5.1(d) plot the activation time maps of the tissue area with 45×45 cells in the central part of the tissue boxed in Figure 5.1(a) when applying the stimulus at position '1' and position '3' in (a), respectively.

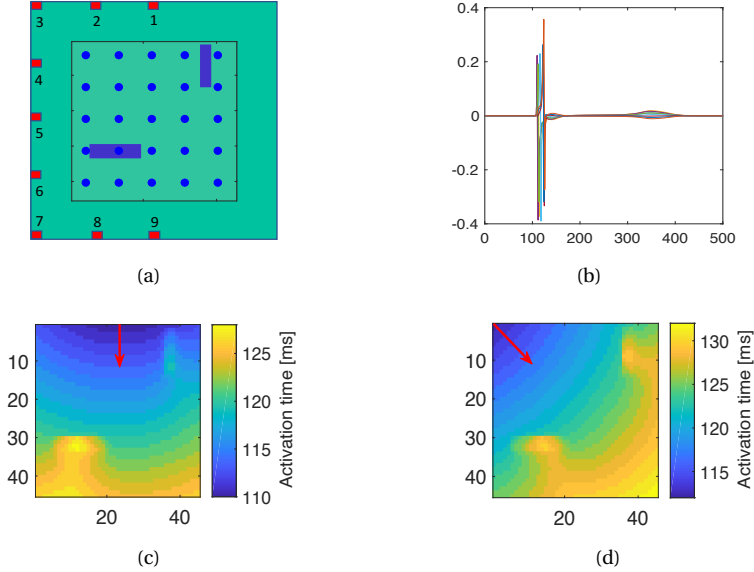


Figure 5.1: An example of the tissue, the generated electrograms and activation time maps. (a) Tissue with two areas of block. The 5×5 blue points represent the 5×5 electrodes and the two blue lines represent the two areas of block. (b) electrograms of nine heart beats; (c) activation time map of the heart beat when applying the stimulus at position '1' in (a); (d) activation time map of the heart beat when applying the stimulus at position '3' in (a).

5.4.2. EVALUATION

To quantify the estimation performance, we calculate the MSE of the conductivity parameters and the MSE of the activation time parameters. The conductivity parameters in the y -direction (the transverse direction) σ_{yy} can be obtained after estimating the conductivity parameters in x -direction (the longitudinal direction) σ_{xx} and the anisotropy ratio α . The longitudinal conductivity at the location of the n th cell, i.e., $\sigma_{yy,n}$, is equal to $\sigma_{xx,n} \cdot \alpha_n$, where $\sigma_{yy,n}$, $\sigma_{xx,n}$ and α_n are the n th elements of the vector σ_{yy} , σ_{xx} and α_n . Then we calculate the MSE for the estimation of the conductivity parameters by

$$\text{Err}_c = \frac{\|\sigma_{xx} - \hat{\sigma}_{xx}\|^2 + \|\sigma_{yy} - \hat{\sigma}_{yy}\|^2}{2N}, \quad (5.15)$$

where N represents the number of cell groups, σ_{xx} and σ_{yy} represents the real longitudinal and transverse conductivity parameters, and $\hat{\sigma}_{xx}$ and $\hat{\sigma}_{yy}$ represents their estimates, respectively.

The MSE of the estimated activation time parameters for the l th time frame (heart beat) is calculated by

$$\text{Err}_a(l) = \frac{1}{N} \sum_{n=0}^{N-1} (\tau_n(l) - \hat{\tau}_n(l))^2, \quad (5.16)$$

where τ_n and $\hat{\tau}_n$ represent the real and estimated activation time parameters in ms, respectively.

Table 5.2: Comparison of estimation errors with different methods

Heart beats	Tissue Type (i)				Tissue Type (ii)				Tissue Type (iii)			
	Err _c (SCFA1)	Err _c (SCFA2)	Err _a (SCFA1)	Err _a (SCFA2)	Err _c (SCFA1)	Err _c (SCFA2)	Err _a (SCFA1)	Err _a (SCFA2)	Err _c (SCFA1)	Err _c (SCFA2)	Err _a (SCFA1)	Err _a (SCFA2)
1	0.0435	0.0384	1.0318	1.0198	0.0322	0.0273	1.0752	1.0502	0.0866	0.0861	1.5108	1.3719
2	0.0441	0.0360	0.6643	0.6480	0.0276	0.0236	1.0460	1.0142	0.0706	0.0672	1.1976	1.0890
3	0.0399	0.0337	0.6748	0.6674	0.0301	0.0233	1.4008	1.3470	0.0558	0.0579	1.6209	1.5945
4	0.0397	0.0342	0.8785	0.8598	0.0322	0.0212	0.6459	0.6262	0.0506	0.0462	0.9196	0.8440
5	0.0386	0.0334	0.9985	0.9783	0.0299	0.0215	0.4763	0.4470	0.0509	0.0477	1.5565	1.5558
6	0.0385	0.0343	0.7177	0.7010	0.0284	0.0216	0.6137	0.6030	0.0533	0.0480	0.5640	0.5601
7	0.0381	0.0360	1.2966	1.2925	0.0272	0.0216	1.7445	1.7356	0.0480	0.0482	1.2185	1.1977
8	0.0442	0.0386	0.7007	0.6944	0.0272	0.0273	1.5225	1.5130	0.0555	0.0504	2.0798	2.0526
9	0.0455	0.0388	0.7837	0.7798	0.0329	0.0294	2.4660	2.4561	0.0539	0.0518	0.9106	0.9103
Avg.	0.0413	0.0359	0.8607	0.8490	0.0297	0.0241	1.2212	1.1991	0.0585	0.0560	1.2865	1.2422

We first compare the parameters estimated by SCFA1 and SCFA2 using a single heart beat. Table 5.2 shows the estimation errors for different heart beats. It can be seen that for all the tissue examples the estimation errors of the conductivity and the activation time parameters both decrease when using the joint estimation method SCFA2 proposed in this work. Moreover, it is clear that the estimation performance varies with the source position. This is due to the interplay between the origin of the wave (i.e., the source position) and the local conductivity. Compared with SCFA1, the average MSE of conductivity parameter per cell obtained by SCFA2 decreases from 0.0413 mS/cm to 0.0359 mS/cm for tissue type (i), from 0.0297 mS/cm to 0.0241 mS/cm for tissue type (ii), and from 0.0585 mS/cm to 0.0560 mS/cm for tissue type (iii).

The estimation of the activation time is also improved by using the joint estimation method. The electrical wave propagates fast across the tissue. The SCFA1 method uses the steepest descent method to estimate the activation time parameters of the 45×45 cells per tissue. The MSE of the activation time parameter per cell is 0.8607 ms², 1.2212 ms², and 1.2865 ms² for tissue type (i), type (ii), and type (iii), respectively. Unlike SCFA1, the SCFA2 method jointly estimates all the parameters and the MSE of the activation time parameter per cell decreases to 0.8490 ms², 1.1991 ms², and 1.2422 ms² for tissue type (i), type (ii), and type (iii), respectively. Although the MSE decrease for per cell is small, at the high speed of wave propagation in tissue this difference can be significant.

We then study the use of multiple heart beats to estimate the parameters. We start from using two heart beats and test different combinations of two heart beats, for example, combining heart beat '1' with each of the heart beats '2', '3', ..., '9', respectively, i.e., heart beats '1'&'2', '1'&'3', ..., '1'&'9'. We here compare the estimation performance us-

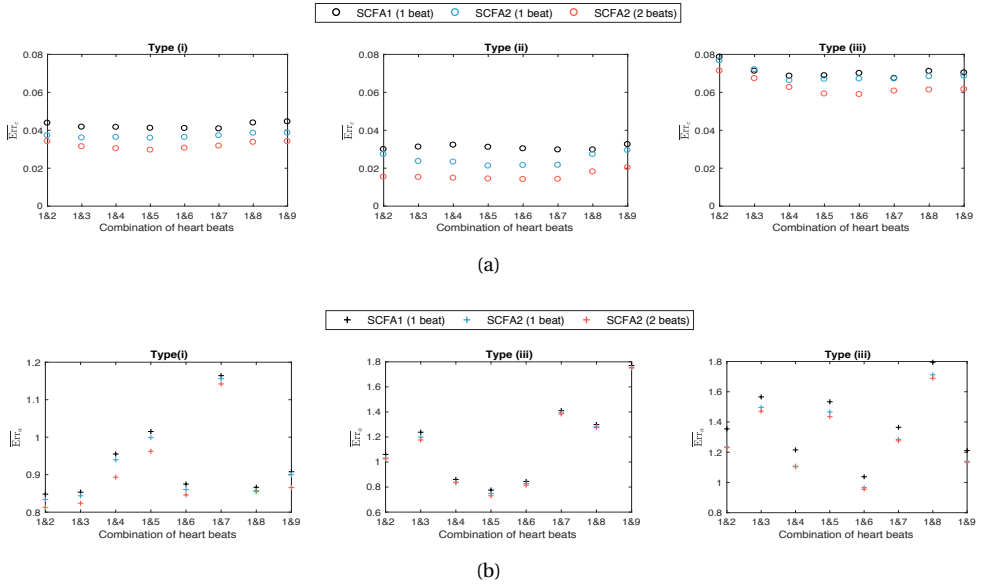


Figure 5.2: conductivity parameters (a) and activation time parameters (b). The SCFA2 method achieves better performance than the SCFA1 method and the estimation errors of the parameters are further reduced by combining two different heart beats and jointly estimating the parameters.

ing three different methods, that are: 1) SCFA1 using one heart beat, 2) SCFA2 using one heart beat, and 3) SCFA2 using two heart beats. Figure 5.2 shows the resulting estimation errors of the conductivity parameters and activation time parameters. The estimation errors of the first two methods are obtained by calculating the errors for the conductivity and activation time per heart beat and averaging these across the two heart beats. The estimation errors of SCFA2 using two heart beats are calculated directly. Figure 5.2(a) and 5.2(b) respectively show the estimation errors of the conductivity parameters and the activation time parameters on the three tissue examples using different methods. We here use $\overline{\text{Err}}_c$ and $\overline{\text{Err}}_a$ to denote the estimation errors of the conductivity parameters and the activation time parameters, respectively. We can see that for all tissue examples, SCFA2 achieves better performance than SCFA1 and the estimation errors of the parameters are reduced by combining two different heart beats and estimating the parameters jointly. These results support our hypothesis that the electrical waves in different heart beats can "illuminate" the tissue from different directions and provide useful information for the tissue parameter estimation.

We then increase the number of heart beats for estimation using SCFA2. Figure 5.3(a) and Figure 5.3(b) respectively plot the estimation errors of the conductivity parameters and the activation time parameters on the three tissue types from using one heart beat up to nine heart beats. From Figure 5.3(a), we see that for all the tissue examples the estimation error of the conductivity parameters first decreases and then tends to stabilize with the increase of the number of heart beats. We also observe from Figure 5.3(a) that using two heart beats gives an improvement, but using more than three heart beats is

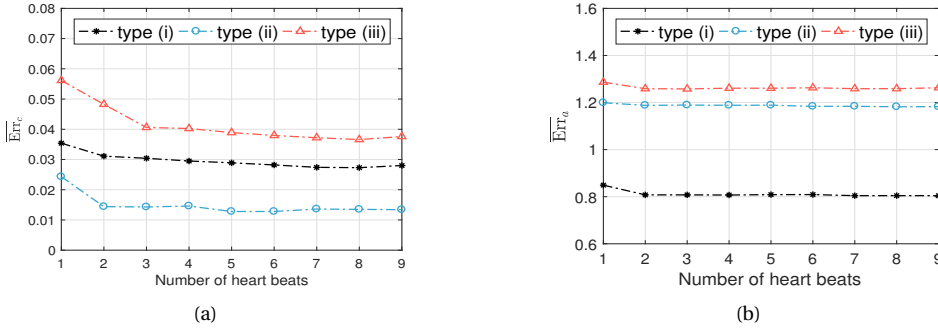


Figure 5.3: Estimation errors of conductivity parameters (a) and activation time parameters (b) obtained by SCFA2 using different number of heart beats.

hardly helpful. We can also find that tissue type (iii) needs more heart beats to achieve good results since it has a more complicated underlying structure. However, we also see that it has the largest relative decrease in estimation error when going from one to multiple heart beats. This can also be explained by the more complex structure, where a larger benefit is obtained by combining heart beats originating from different directions. From Figure 5.3 (b), we find that using multiple heart beats helps to improve the estimation of the activation time parameters, and always performs better than the steepest decent method. However, the improvement of the activation time estimation due to the increase of heart beats is less obvious compared to the conductivity estimation in Figure 5.3 (a). This is because the activation time parameters change across different heart beats, while the conductivity parameters are shared across different heart beats. In addition, the increase of the unknown parameters due to the increase of the number of heart beats makes it more challenging to find the optimal solution in the non-convex optimization problem.

In Figure 5.4, we show examples of the real and estimated conductivity maps obtained with SCFA1 using one heart beat, SCFA2 using one heart beat, two heart beats, and three heart beats. Since the longitudinal conductivity is equal to the transverse conductivity for tissue type (i) and the estimation results are similar in the two directions, we only show here the conductivity maps in the longitudinal direction for tissue type (i). For tissue types (ii) and (iii), we show the conductivity maps in both the longitudinal and transverse directions. Comparing the results of SCFA1 and SCFA2 using one heart beat, we can see that SCFA2 achieves better estimation than SCFA1, which implies that improving the estimation of activation time helps to improve the estimation of the conductivity. Comparing the results of using one heart beat to the results of using two heart beats by SCFA2, we see that combining multiple heart beats obviously improves the estimation. From the estimated conductivity maps of tissue type (ii) in Figure 5.4, we find that the algorithm also works well when there is a smooth variation in the conductivity maps. However, the estimated conductivity maps seem less accurate for more heterogeneous examples (iii), mainly in case of non-constant anisotropy ratios. This could be a consequence of the fixed stereotype waveform for all cells.

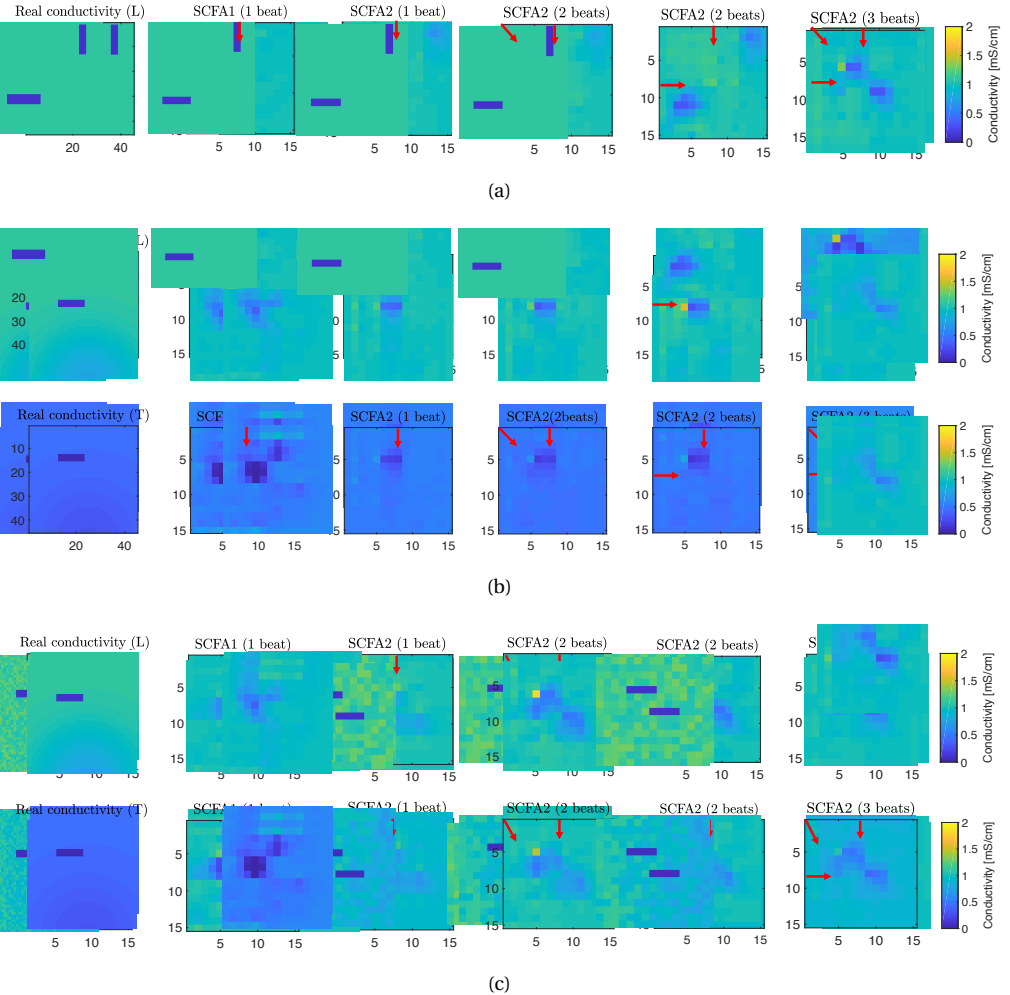


Figure 5.4: Examples of the real conductivity maps and the estimated conductivity maps. The subfigures in the first column show the real conductivity maps and the subfigures in other columns show the estimated conductivity maps, which are obtained using different methods, including SCFA1 using one heart beat, SCFA2 using one heart beat, two heart beats, and three heart beats. The red arrow on the map represents the propagation direction of the wave in the heart beat. The number of arrows indicates the number of heart beats used in the estimation. (a) Longitudinal (L) conductivity maps for tissue types (i); (b) Longitudinal (L) and transverse (T) conductivity maps for tissue types (ii); (c) Longitudinal (L) and transverse (T) conductivity maps for tissue types (iii).

From the simulation results, we here have some interesting findings on the conductivity estimation. For all tissue examples, we find that the combination of the waves from top and top left achieve a different conductivity map compared to the combination of the waves from top and left, which suggests that the propagation direction of the wave affects the estimation results. From the visualized examples in Figure 5.4, we can see that using the wave from the left helps to estimate the longitudinal conduction block as the time delay at the position of the block is more obvious when the wave is propagating from the left. Similarly, using the wave from the top is good for estimating the transverse conduction block. In addition, the readers may find that in tissue example (i), the conduction block in the transverse direction is better estimated than the longitudinal direction. This is because the electrode is exactly positioned on the conduction block in the transverse direction, while this is not the case for the conduction block in the longitudinal direction and the cells close to the electrode have a bigger impact on the electrograms.

Based on these analyses, we find that the conductivity estimation is affected by many factors such as the estimation of the activation time parameters, the propagation direction of the electrical wave in a heart beat, the positions of the electrodes, and the underlying structure of the tissue. Since the underlying structure of the tissue is unknown and the relative positions of the electrodes to the cells are random, we cannot control these two factors in practice. To improve estimation of the conductivity parameters, it thus obviously helps to combine multiple heart beats to get more useful information and try to improve the estimation of the activation time parameters.

5.5. EXPERIMENTS ON CLINICAL DATA

In this section, we evaluate the proposed method with clinical data. These data are human atrial epicardial electrograms measured from patients during open heart surgery. The study protocol was approved in February 2010 by the Medical Ethics Committee (2010-054) in the Erasmus Medical Center, Rotterdam, The Netherlands. High resolution mapping arrays with 192 electrodes are used to measure the unipolar electrograms from different atrial epicardial sites. The distance between the neighboring electrodes is 2 mm. Five seconds of sinus rhythm and ten seconds of atrial fibrillation are recorded at every mapping site and all recordings are sampled at 1 kHz. In this work we use recordings measured from Bachmann's bundle during sinus rhythm. Readers can find more details on the mapping approach and the electrode array in [12]. The ventricular activities in the measurements are canceled by the method in [13] before doing the parameter estimation.

The tissue is discretized into 192 equal square areas of $2\text{ mm} \times 2\text{ mm}$ and each area is assumed to have an electrode positioned on top of it. Each small area is then discretized into 3×3 cell groups and each cell group is regarded as a cell to reduce the number of unknowns for practical consideration. In each estimation, we take a smaller tissue area measured by 5×5 electrodes instead of the whole tissue area to reduce the computation cost, then the spatial resolution to be obtained is 15×15 , with resolution scale thus $R = 3$.

Before estimating the parameters, we first segmented the recording in heartbeats. The segment size is selected to include most of the information in one heart cycle. Given the sampling rate of 1 kHz, each heart beat segment consists of 800 samples. Figure 5.5

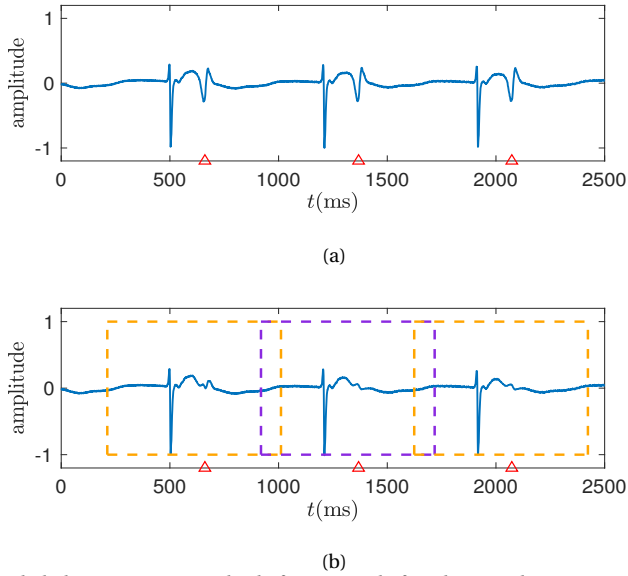


Figure 5.5: Epicardial electrogram examples before (a) and after (b) canceling ventricular activity and heart beat segmentation example. The red triangle marks the presence of ventricular activity. The orange and purple boxes mark the heart beat segments.

shows an example of the heart beat segmentation of an electrogram. We can see that the waveform shape varies among different heart beats, which motivates us to utilize different heart beats to increase the information for robust parameter estimation.

We used five consecutive heart beats from each recording and test the performance of the proposed algorithm when using one, two, three, four, and five heart beats, respectively. Since there is no ground truth of the real parameters, we evaluate the performance of the proposed method by comparing the real electrograms to the reconstructed electrograms obtained using the parameters estimated by the proposed method. Note that the conductivity parameters and the anisotropy ratio parameters are assumed to be similar for different heart beats while the activation time parameters differ across heart beats. We quantify the reconstruction errors of the electrograms by the reconstruction error

$$\text{Err}_{\text{rec}} = \frac{1}{M} \sum_1^M \|\mathbf{y}_m - \hat{\mathbf{y}}_m\|_2, \quad (5.17)$$

where \mathbf{y}_m and $\hat{\mathbf{y}}_m$ respectively represent the real and the estimated EGM segments during atrial activity, and $\|\cdot\|_2$ represents the l_2 -norm of a vector.

Figure 5.6 shows the reconstruction errors of the electrograms from eight patients obtained by the proposed method when increasing the used number of heart beats from one to five. We see that in most cases the reconstruction error first decreases then tends to stabilize when increasing the number of heart beats for estimation, which demonstrates the added value of using multiple heart beats. For patient 1 and patient 3, the improvement obtained by increasing the number of heart beats for parameter estimation is small, which is possibly because the electrical waves in different heart beats of

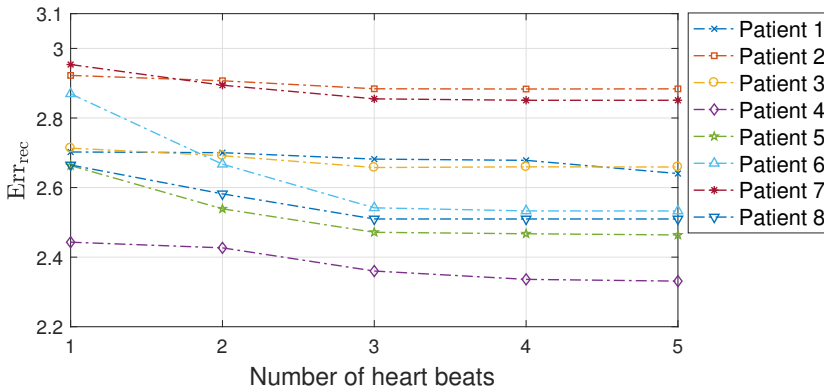
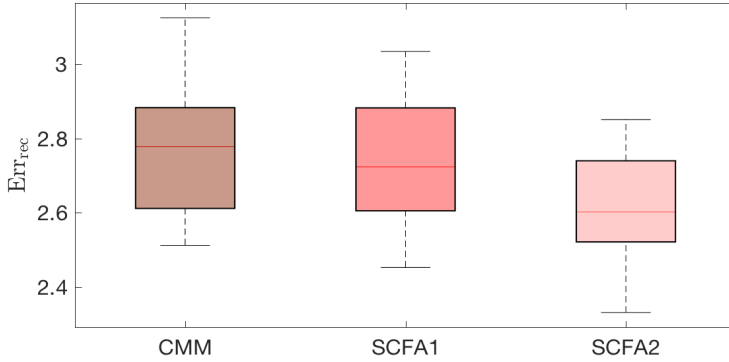


Figure 5.6: Reconstruction errors of electrograms from eight patients using different number of heart beats for parameter estimation.

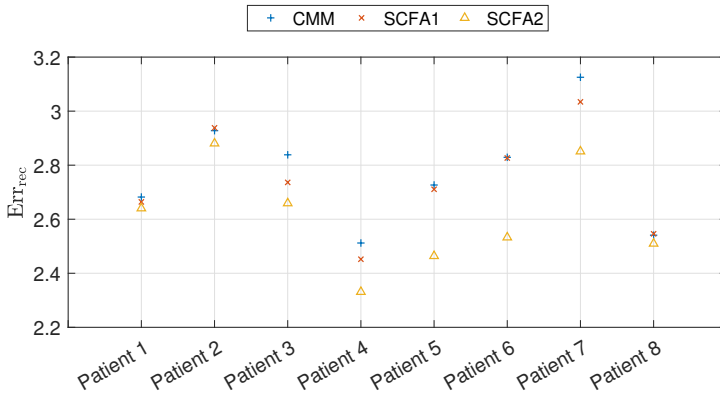
these patients have a very similar propagation pattern.

We further compare the proposed method with the CMM method proposed in [14] and the SCFA1 method in [7]. Figure 5.7(a) shows the box plots of the reconstruction errors of the electrograms from eight patients using different methods. Overall, the reconstruction errors obtained by the SCFA2 method proposed in this work achieves better performance, and SCFA1 performs on average slightly better than CMM in most of cases. Figure 5.7(b) further shows the reconstruction errors of the electrograms of each patient. We see that the SCFA2 always achieves the best performance, as it combines the information of multiple heart beats. The obvious improvement obtained by SCFA2 can be found from Patient 3 to Patient 7, while the smaller improvements are obtained from Patient 1, Patient 2, and Patient 8. This is possibly because the heart beats are similar in these patients and adding additional heart beats does not give much additional information for parameter estimation in SCFA2. For Patient 1, Patient 2, and Patient 8, the performance of the three methods are close, although SCFA1 and SCFA2 consider more realistic conditions and use less assumption to simplify the problem compared to CMM. This might be because the number of unknown parameters with SCFA1 and SCFA2 is larger than with CMM. This means it is more challenging to find the optimal solution when solving the non-convex optimization problem.

The plots in Figure 5.8 and Figure 5.9 give two examples of the estimated activation time maps, the conductivity maps, and the real and the reconstructed electrograms of two patients obtained using five heart beat segments for parameter estimation. Figure 5.8 (a) and 5.9 (a) show the estimated activation time maps obtained by the steepest descent method and Figure 5.8 (b) and Figure 5.9 (b) show the estimated activation time maps obtained by the proposed method, from which we can see some differences between the estimated activation time obtained by the two methods. Subfigures (c) and (d) in Figures 5.8 and 5.9 show estimated conductivity maps in the longitudinal direction and the transverse direction obtained by the SCFA2 method, respectively. Figure



(a)



(b)

Figure 5.7: Reconstruction errors of the electrograms from eight patients using CMM, SCFA1, and SCFA2 for parameter estimation. (a) Box plots of the reconstruction errors of the eight patients. (b) The reconstruction error of the electrograms for each patient.

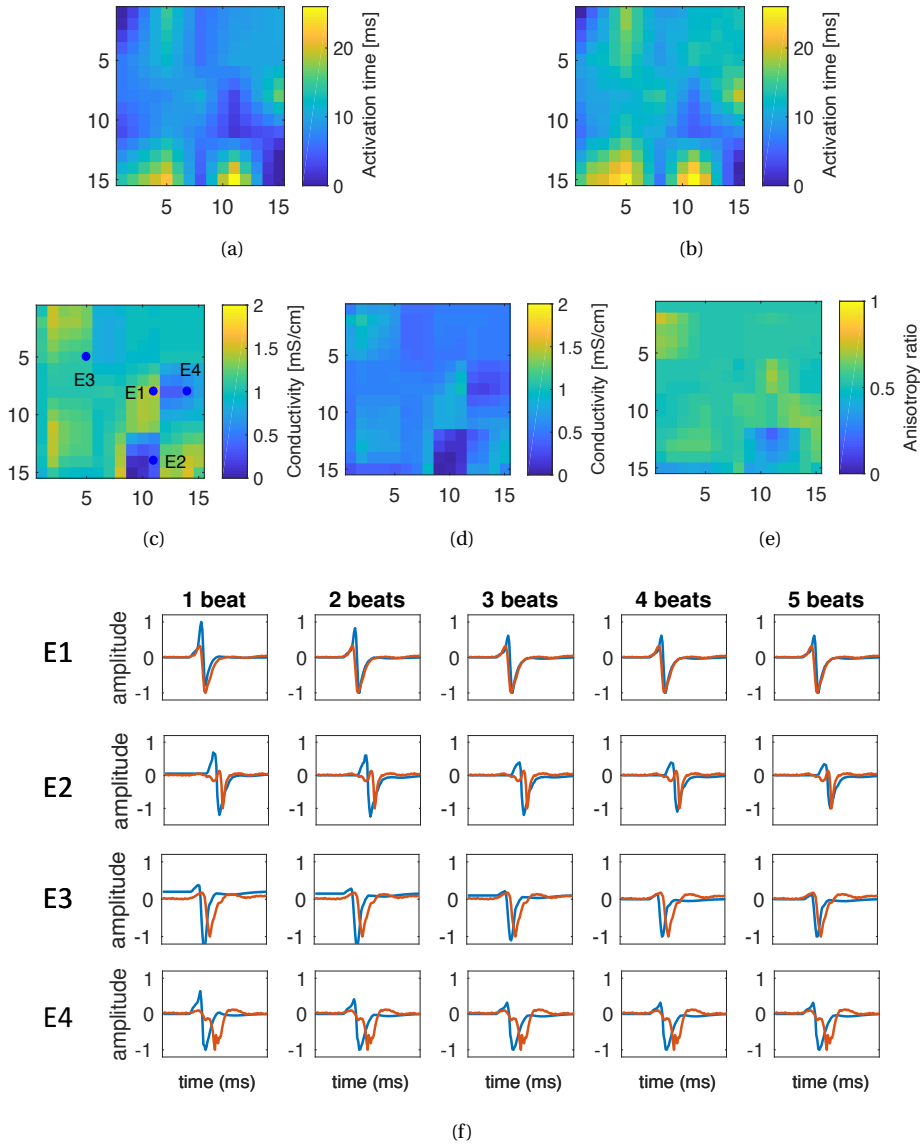


Figure 5.8: Example of the estimated conductivity maps, the real epicardial electrogram (EGM) and the reconstructed EGM obtained with the parameters estimated by the proposed method using different number of heart beats of patient 5. (a) and (b) show the estimated activation time maps for obtained by the steepest descent method and the SCFA2 method, respectively. (c) and (d) show estimated conductivity maps in the longitudinal direction and the transverse direction obtained by the SCFA2 method, respectively. (e) shows the anisotropy ratio map obtained by the SCFA2 method. (f) shows the real EGMs (red) and the reconstructed EGMs (blue) measured at the electrode positions (marked by the blue points) in (c), respectively.

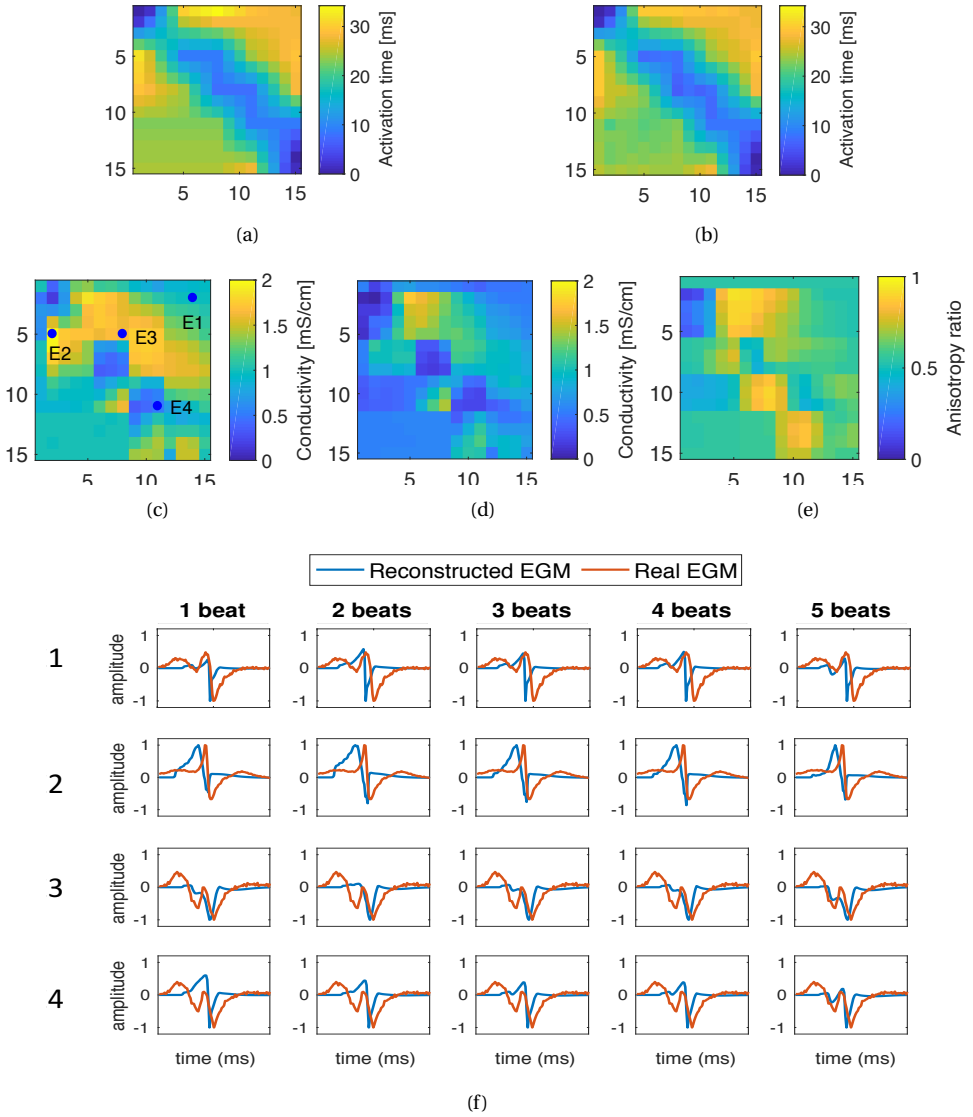


Figure 5.9: Example of the estimated conductivity maps, the real epicardial electrogram (EGM) and the reconstructed EGM obtained with the parameters estimated by the proposed method using different number of heart beats of patient 6. (a) and (b) show the estimated activation time maps obtained by the steepest descent method and the SCFA2 method, respectively. (c) and (d) show estimated conductivity maps in the longitudinal direction and the transverse direction obtained by the SCFA2 method, respectively. (e) shows the anisotropy ratio map obtained by the SCFA2 method. (f) shows the real EGMs (red) and the reconstructed EGMs (blue) measured at the electrode positions (marked by the blue points) in (c), respectively.

5.8 (e) and Figure 5.9 (e) show the anisotropy ratio maps obtained by the SCFA2 method with the value varying from 0.30 to 0.69 in Figure 5.8 (e) and with the value varying from 0.11 to 0.93 in Figure 5.9 (e), respectively. Figure 5.8 (f) and Figure 5.9 (f) show examples of the real epicardial electrograms and the reconstructed epicardial electrograms obtained with the parameters estimated by the proposed method using different number of heart beats, respectively. We observe from Figure 5.8 (f) that the reconstructed electrograms match a bit better the real electrograms when increasing the number of heart beats in most cases and the the electrogram segments with a single deflection can be better reconstructed compared to the electrograms with multiple deflections. The reconstruction in Figure 5.9 (f) is less good compared to the reconstruction in Figure 5.8 (f). From the EGM examples measured at the electrode positions 'E3' and 'E4' in Figure 5.9 (f), we see that using multiple heart beats helps to reconstruct the electrograms having double potentials. However, at the electrode position 'E1' in Figure 5.9 (f), increasing the number of heart beats does not obviously improve the reconstruction. This may be, because the EGM segments of different heart beats are too similar.

5.6. CONCLUSIONS AND DISCUSSIONS

In this work, we proposed a novel algorithm to jointly estimate tissue properties using the cross power spectrum model of microelectrode array data in combination with confirmatory factor analysis (CFA). Based on the reasonable assumption that the conductivity and anisotropy ratio parameters are similar among multiple heart beats and frequencies, we proposed to estimate these parameters using multiple heart beats and frequencies with the simultaneous CFA (SCFA). The activation time of cells are also estimated jointly with these parameters but will be different across heart beats. With the SCFA algorithm, we are able to determine the resolution that can be obtained with a given amount of data. Compared to the previously published SCFA for conductivity estimation in [7], the proposed SCFA in this work makes use of multiple heart beats which "illuminate" the tissue from different directions and can therefore better estimate the tissue properties. Experiments on simulated data and clinical data demonstrate that the proposed SCFA method obtains good estimation of the tissue conductivity and reconstructs realistic electrograms that match the clinical data well.

This work provides an efficient tool to estimate the hidden parameters of diseased tissue, which is helpful in the understanding and diagnosis of the disease. Intended applications of this work can be automated detection of the atrial areas of bad conduction and finding the relation between the alternations of atrial conduction and the initiation and perpetuation of cardiac arrhythmias in order to guide therapy methods like cardiac ablation.

Although conduction velocity, which looks at the propagation of the action potential, has been commonly used to determine the areas of conduction block, the findings are realization dependent, since the abnormalities are determined based on the output realizations of the system, i.e., on the wave propagation. Moreover, looking at (pairs of) electrodes, not all spatial correlations between the different measurements are taken into account. This is unlike the proposed method, which considers the heart as the system, where each cell or area of cells has certain properties that are important to understand the arrhythmias like atrial fibrillation. With the proposed method, we can determine the

parameters that describe the underlying system such as the conductivity, anisotropy ratio, etc. Knowing the system (or its parameters) that can generate the realisations that we measure as electrograms is the ultimate goal. Examples that compare the confirmatory factor analysis method with conduction velocity for conduction block detection can be found in [7].

Although the proposed method has its advantages on jointly estimating the parameters of cardiac tissue, it can still be improved by taking into account more realistic electrophysiological conditions in atrial tissue. For example, the assumption of a common stereotype action potential waveform for all cells reduces the computational cost for estimation, but ignores the heterogeneities in atrial tissue and reduces the accuracy of the model. The assumption that conductivity tensors are aligned along the axes ignores the heterogeneous tissue micro-structure and the two dimensional assumption of tissue makes the application limited to only thin-walled tissues. In the near future, we would like to take into account more realistic conditions, such as multi-layers of tissue, orientations of the fibers, etc, to improve the model. To do so, there are more parameters needed to describe the structure of the tissue, which will in turn increase the computational complexity of estimating the model parameters and also increase the variance on the estimated parameters. However, a critical issue in this area is reducing complexity of the model to make it possible to solve complicated inverse problems for tissue parameter estimation. Therefore, we will take into account both the accuracy of the model and the computational complexity of parameter estimation in future work.

REFERENCES

- [1] T. A. Brown and M. T. Moore, *Confirmatory factor analysis*, Handbook of Structural Equation Modeling, 361 (2012).
- [2] C. D. Cantwell, C. H. Roney, F. S. Ng, J. H. Siggers, S. J. Sherwin, and N. S. Peters, *Techniques for automated local activation time annotation and conduction velocity estimation in cardiac mapping*. Computers in Biology and Medicine **65**, 229 (2015).
- [3] D. N. Lawley and A. E. Maxwell, *Factor analysis as a statistical method*, Journal of the Royal Statistical Society. Series D (The Statistician) **12**, 209 (1962).
- [4] K. G. Jöreskog, *A general approach to confirmatory maximum likelihood factor analysis*, Psychometrika **34**, 183 (1969).
- [5] K. G. Jöreskog and D. N. Lawley, *New methods in maximum likelihood factor analysis*, British Journal of Mathematical and Statistical Psychology **21**, 85 (1968).
- [6] A. I. Koutrouvelis, R. C. Hendriks, R. Heusdens, *et al.*, *Robust joint estimation of multicrophone signal model parameters*, IEEE/ACM Transactions on Audio, Speech, and Language Processing **27**, 1136 (2019).
- [7] M. Sun, N. M. de Groot, and R. C. Hendriks, *Cardiac tissue conductivity estimation using confirmatory factor analysis*, Computers in Biology and Medicine **135** (2021).

- [8] M. R. Courtemanche, R. J. Ramirez, and S. Nattel, *Ionic mechanisms underlying human atrial action potential properties: insights from a mathematical model*, American Journal of Physiology-Heart and Circulatory Physiology **275**, H301 (1998).
- [9] R. H. Byrd, M. E. Hribar, and J. Nocedal, *An interior point algorithm for large scale nonlinear programming*, SIAM Journal on Optimization **9** (1999).
- [10] R. H. Byrd, J. C. Gilbert, and J. Nocedal, *A trust region method based on interior point techniques for nonlinear programming*, Mathematical Programming **89**, 149 (2000).
- [11] R. A. Waltz, J. L. Morales, J. Nocedal, and D. Orban, *An interior algorithm for nonlinear optimization that combines line search and trust region steps*, Mathematical Programming **107**, 391 (2006).
- [12] A. Yaksh, L. J. M. E. van der Does, *et al.*, *A novel intra-operative, high-resolution atrial mapping approach*, Journal of Interventional Cardiac Electrophysiology **44**, 221 (2015).
- [13] M. Sun, E. Isufi, N. M. de Groot, and R. C. Hendriks, *Graph-time spectral analysis for atrial fibrillation*, Biomedical Signal Processing and Control **59** (2020).
- [14] B. Abdi, R. C. Hendriks, A.-J. van der Veen, and N. M. de Groot, *A compact matrix model for atrial electrograms for tissue conductivity estimation*, Computers in Biology and Medicine **107**, 284 (2019).

6

CONCLUSIONS AND FUTURE WORK

IN this chapter, we revisit the research questions in Chapter 1 and provide our findings in response to these questions in Section 6.1. Then we discuss several open research questions that are worth investigation for future research in Section 6.2.

6.1. CONCLUDING REMARKS

In order to answer the research questions that we proposed in Chapter 1, we studied the EGMs using two different strategies: In Chapter 3 using graph signal processing techniques to study the electrograms from a higher abstraction level and in Chapter 4 and 5 using confirmatory factor analysis to study the electrograms based on a more detailed electrophysiological model. In this section we provide the concluding remarks on these two strategies and the answers to the research questions specialized in Chapter 1.

6.1.1. GRAPH SIGNAL PROCESSING FOR AF STUDYING

Given the high resolution epicardial electrograms from AF and non-AF patients, we first carried out a graph spectral analysis on this data to learn the behavior of the electrograms during the normal sinus rhythm (SR) and atrial fibrillation (AF) in Chapter 3. Since the data is high dimensional and shows high irregularity, we considered to use graph signal processing techniques that are good at analyzing such data. To the best of our knowledge, it is the first study to apply this advanced technique to analyze the epicardial electrograms and we therefore started from the following research questions:

***Q1.1.** Since a good and representative graph structure will be important to the spectral analysis of graphs signals, how can we construct a graph to model the EGM data?*

A1.1. We showed in Chapter 3 that we can construct an undirected graph based on the physical property of the electrodes to represent the spatial relationship of the multi-electrode electrograms. We took the electrodes of the mapping array as the nodes of the graph and then built the edges of the graph. Generally there are two ways to build the

edges, either by considering the data structure or based on the physical properties of the nodes. In order to compare the electrograms during different heart rhythms, i.e., SR and AF, we considered to use the same graph structure for both situations. Based on the assumption that neighboring electrodes record a similar signal, we connected each node to its eight nearest neighbors. This is the natural choice of the connection when there is little prior knowledge on the signals. It has been shown in Chapter 3 that based on this structure we are able to analyze the spectral difference of the electrograms between SR and AF using graph signal processing tools. However, since we have a very structured electrode array, the graph built based on the physical property of the electrodes is very regular. Although the graph captures the similarity property of neighbored electrodes, it did not directly capture the irregular property of the data. This also limits the graph-time spectral analysis on AF data in Chapter 3. Finding a more meaningful structure through graph learning techniques might bring more insights on AF, which will be further discussed in Section 6.2.1 in this chapter.

Q1.2. *Can we use graph-time signal processing to analyze time-varying EGMs to find differences between normal sinus rhythm (SR) and atrial fibrillation (AF) in the joint space, time, and frequency domain?*

A1.2. Following the graph structure considered in Q1.1, we explored the application of graph signal processing on studying the epicardial electrograms in Chapter 3. Using graph signal processing, the variation of graph signals over the graph can be explored to formulate a spectral analysis for graph signals in the graph frequency domain via the graph Fourier transform. For the time-varying electrograms, we would like to consider their variation not only on the graph domain but also on the temporal dimension. Since the graph Fourier transform is limited in its ability to analyze the graph signal at a fixed time instant and ignores the correlation across time, we proposed the joint short-time Fourier transform and graph Fourier transform to quantify the graph spatial variations of the electrogram temporal frequencies. Finally, we conducted the graph-time spectral analysis on the time-varying EGMs during SR and AF and observed the difference between SR and AF in the spatial-temporal and spectral aspects. However, comparing the studies in Chapter 3 to Chapter 4 and 5, we conclude that given the epicardial electrograms, the graph-time spectral analysis framework proposed in Chapter 3 is better for exploring the behaviour of heart activities from the tissue-level rather than from the cellular level.

Q1.3. *Since EGMs consist of both atrial and ventricular components and for this study the atrial components are of interest, can we propose a graph-time signal processing technique to analyze the spectral difference between atrial activity and ventricular activity? If yes, can we further separate the two activities based on the findings to get more reliable atrial EGMs for AF research?*

A1.3. The answer of this question was given in Chapter 3. From the spectral analysis of the electrograms, we also found that the ventricular activity has less variation over the graph compared to the atrial activity. This finding further motivated us to design

a novel graph-based atrial activity extraction algorithm that leverages the smoothness prior to extract the atrial activity from the noisy measurements. This algorithm captures the morphology characteristics of the heart activities and does not require the uncorrelated or independence assumption between leads to separate the atrial and the ventricular activities. It further corroborates the potential of the graph-time spectral analysis for AF study.

6.1.2. ELECTROPHYSIOLOGICAL EGM MODELS AND PARAMETER ESTIMATION

In this dissertation, we also investigated in Chapter 4 and Chapter 5 the more detailed electrophysiological models of cardiac tissue. These models involve useful parameters that are directly connected to tissue properties. In order to reduce the complexity of the electrophysiological model and efficiently estimate the tissue parameters from the model, we proposed the following research questions:

Q2.1. *Can we find a simplified, but accurate electrophysiological model which can capture the spatial-temporal information of EGM data?*

A2.1. As shown in Chapter 4, we developed a cross-power spectral density matrix (CPSDM) model for the multi-electrode electrograms, which can capture the spatial correlation of the data. It was built based on the time-domain impulse response model of the atrial electrograms, which simplifies the calculation of all cell action potentials by assuming all cells generate the same stereotype action potential once activated. The initial study that proposed the impulse response model used the assumption that the anisotropy ratio is known and is fixed everywhere in the tissue [1]. In Chapter 4 we considered the more realistic condition that the anisotropy ratio is unknown and can change in 2D and 3D tissue. The impulse response model was then improved taking into account the variability of the anisotropy ratio. To further make use of the spatial information of the data, the impulse response model was transformed into the frequency domain by the short-time Fourier transform and finally led to the CPSDM model for the multi-electrode electrograms.

Q2.2. *How can we efficiently estimate tissue parameters using multiple frequencies and multiple heart beats in SR or AF?*

A2.2. This question was answered in Chapter 4 and Chapter 5. Since confirmatory factor analysis (CFA) is usually confined to analyze variance-covariance structures like cross-power spectral density matrix, and the parameters in the CFA model are estimated to reproduce the input variance-covariance matrix, we can utilize this tool to estimate the parameters of interest from the CPSDM model of the electrograms. As shown in Chapter 4 and Chapter 5, we formulated a CFA problem to estimate the tissue parameters, i.e., the conductivity, the anisotropy ratio, and the activation time parameters, from the CPSDM model. To reduce the feasibility set of the parameter space when solving the optimization problem, we added non-linear constraints with the prior knowledge of the parameters and also constraints related to the mathematical properties of the problem

at hand, e.g., positive semidefinite property of the CPSDMs. These constraints further improved the robustness of the parameter estimation using CFA.

Based on the fact that the conductivity and the anisotropy ratio parameters are shared among multiple frequencies, we proposed the simultaneous CFA that can estimate the parameters in multiple temporal frequencies simultaneously. This was shown and discussed in Chapter 4. Since the conductivity and the anisotropy ratio parameters are also shared among multiple heart beats, we further made use of multiple heart beats in the estimation to increase the ratio between the number of equations and the number of unknown parameters. This was introduced in Chapter 5.

The proposed electrogram model and the parameter estimation algorithm can be applied to both SR and AF conditions. Yet the evaluations were only conducted in the SR condition in Chapter 4 and Chapter 5. More work is needed to evaluate the performance in AF. Even though there may be multiple waves propagating simultaneously in the tissue during AF, action potentials of all cells can still be modeled as delayed versions of a single template action potential in the impulse response model. However, there are some practical problems that need to be considered when applying the model and the estimation algorithm to such AF conditions, such as the selection of the template action potential and the proper length of a time frame. In Chapter 4 and Chapter 5, the template action potential is chosen based on the normal heart rhythm and we considered only one activation for each atrial cell in a time frame. Since the action potential duration of atrial cell gets shorter and the atria beat much faster across time during AF [2, 3], the template action potential for SR is not suitable for AF, and a time frame that includes only one beat of the atria can be very short. This might increase the CPSDM estimation errors and further degrade the performance of the tissue parameter estimation. These practical problems are worth investigation in the future to improve the modelling of action potential propagation and the parameter estimation in AF, which are recommended in Section 6.2.2 in this Chapter.

Q2.3. *Given the spatial resolution of the measurements, can we determine the maximum resolution for which we can reliably estimate the parameters?*

A2.3. As introduced in Chapter 4 and Chapter 5, CFA comes with two identifiability conditions that need to be satisfied to solve the optimization problem. To solve the problem, the number of knowns should be larger than the number of unknowns. The number of knowns depends on the number of electrodes for data measurements. When there is no sensor self noise, the number of unknowns depends only on the spatial resolution for which we consider to estimate the parameters. In this situation, the unknowns are the conductivity, the anisotropy ratio, and the activation time parameters. The number of parameters depends on the number of cell groups, i.e., on the spatial resolution. However, when there is also sensor self noise, the unknown parameters also include the PSDs of the sensor self noises, which depends on the number of electrodes. Therefore, in this situation, the number of unknowns depends on both the spatial resolution and the number of electrodes. By analyzing the number of knowns and unknowns in the optimization problem, we can find the relationship between the desired resolution and the required amount of data.

Parameters that are shared across frequencies or across heart beats can be estimated simultaneously in multiple frequencies or multiple heart beats, which requires less sensors to obtain the same spatial resolution and therefore can easier satisfy the identifiability conditions in the CFA problem. With the reasonable assumptions that the conductivity parameters and the anisotropy parameters are constant across different frequencies, we proposed the simultaneous CFA (SCFA) to jointly estimate these parameters using multiple frequencies in Chapter 4, which enables us to make efficient use of the data. Chapter 5 further improves the SCFA approach for jointly estimating cardiac tissue parameters, which is not only able to jointly estimate the tissue conductivity and anisotropy ratio parameters by solving a CFA problem as in Chapter 4, but also able to jointly estimate the cell activation time. In Chapter 5, the estimation performance is further improved by making use of the information provided by multiple heart beats. By assuming that the conductivity parameters and the anisotropy parameters are constant across different heart beats, the ratio of known and unknown parameters is increased such that a higher spatial resolution of parameters can be obtained given the same amount of data. However, the assumption that the conductivity tensor is aligned along the axes is less realistic. The box constraint that has been applied on the anisotropy ratio, i.e., $0 < \alpha \leq 1$ is limited. This box constraint assumes that we can recognize the longitudinal and the transverse propagating directions and α always represents the longitudinal conductivities, while we do not know the fiber direction in practice. To address the problem, we can try to recognize the propagating direction based on the activation time map (that may be roughly estimated by the steepest descent method) before doing the estimation or we can use a less tight box constraint on α .

6.2. FUTURE RESEARCH QUESTIONS

This dissertation introduced new approaches to model and analyze the epicardial electrograms that help to investigate the mechanisms of AF. In this section we recommend some research questions that are worth studying in the future.

6.2.1. GRAPH SIGNAL PROCESSING FOR AF RESEARCH

In Chapter 3 we proposed an approach based on graph signal processing to study AF. This method combines the graph Fourier transform with the short-time Fourier transform to analyze multi-electrode EGMs in the joint space, time, and frequency domain. By working with a higher-level graph model, we have overcome the difficulties of analyzing the arrhythmia through complicated physical models. However, this approach has some limitations that leads to the following future research directions.

1) Graph construction: As this is the first research that applies graph signal processing to model and analyze EGMs to study AF, an initial difficulty we faced is how to construct the most representative graph. While we relied on a Euclidean-based nearest neighbor approach, it remains still an open question whether it is possible to find a more meaningful structure through graph learning techniques [4]. The graph is, in fact, crucial since it gives the Fourier basis to capture the spatial variability. It remains unanswered whether directed graphs and other graph representation matrices (e.g., normalized or random walk Laplacian) can yield different insights on atrial fibrillation. As

directed graphs may help to indicate the complicated wave propagation directions, it is worth investing these types of graphs to build a more meaningful graph that can capture the hidden dependencies between nodes. The different Fourier basis derived from such a graph might further help to recognize the spectral characteristics of electrograms that can be used for diagnosing the stages of AF.

2) GSP for identification of focal sources: One of the classical mechanisms of AF is about focal sources, which trigger the abnormal activation of cells that causes irregular beating of the atria. Identification of the focal sources in the atria tissue is therefore interesting in the study of AF that might be useful for the guidance of the ablation process. Graph signal processing has been applied for tracing back the diffusion sources in the progression of Alzheimer's disease [5]. More recent work in [6] also proposed a blind deconvolution method to identify the input signal of the diffusion process supported on graphs. These works also inspire us to propose the use of graph signal processing techniques to identify the focal sources that drive AF.

3) Improved atrial activity extraction: It did not escape our notice that the graph-based extraction algorithm imposes a tradeoff between the preservation of the atrial activity and the reduction of the ventricular activity. The latter is heavily influenced by the smoothness upper-bound in the algorithm. This parameter, along with the Lagrange penalty term, has been selected using a grid search. However, it deserves further investigation to check if constant values for different patients are a good choice or whether we need to adjust the values for each case separately.

4) Spectral analysis on larger tissue areas: In Chapter 3 we conducted the spectral analysis of the EGMs measured from the Bachmann's bundle area. It is also interesting to look at other areas of the atria and explore the interaction between the different areas of the atria using the proposed graph-time spectral analysis framework. With the graph we can easily involve more electrodes that reside on a complex three dimensional shape like the human atria and then apply graph signal processing techniques to analyze the spatial association of the multi-electrode data. We believe that examining the whole atria will provide additional spatial insights on cardiac arrhythmias. However, this requires that the data are measured simultaneously from different regions, which is not yet available for our dataset.

5) Evaluation on a larger dataset: Another direction worth taking in the near future is to corroborate our findings on a larger dataset, with induced and spontaneous AF, and to characterize the graph-time spectral behavior of the arrhythmia at various levels of AF burden. In this direction, we also aim to adopt graph-based techniques to detect AF drivers from epicardial electrograms.

6.2.2. ELECTROPHYSIOLOGICAL MODELS OF CARDIAC TISSUE AND MODEL PARAMETER ESTIMATION

In Chapter 4 and Chapter 5 we modeled the atrial electrograms from the electrophysiological view and extracted the model parameters that help to identify abnormal areas of the atrial tissue. Despite the fact that electrophysiological models of cardiac tissue are being used in studies on cardiac arrhythmias, there are some important issues that are not fully resolved and that we recommend for future research.

1) Modelling of atrial electrograms and parameter estimation for AF: As discussed

in Section 6.1.2, there are some practical problems that need to be considered when applying the atrial electrogram model and the estimation algorithm proposed in Chapter 4 and Chapter 5 to the AF condition. One of the problems is the selection of the time-frame length. During SR, a cell is activated only once in an RR interval (the time interval between two successive R waves of the QRS signal on the electrocardiogram). However, during AF the atria beat faster and a cell can be activated more than once in an RR interval. Since the atria beat much faster during AF, a time frame that includes only one beat of the atria can be very short, resulting in less accurate estimation of the CPSDMs of the measurements, which might further degrade the parameter estimation performance. To better model the atrial electrograms during AF, a possible strategy is to take the RR interval as the frame length and take into account multiple activations in an RR interval. Then the current electrogram model needs to be revised.

Note that during AF, the cell activation pattern can vary from cell-to-cell. Since cells can be triggered for multiple times in an RR interval during AF and the number of activation can be different for different cells, we use J_n to denote the number of activations for the cell with index n ($n \in \{0, 1, \dots, N-1\}$) during an RR interval in AF. Let $v'_0(t)$ be the reference cell action potential generated by only one activation in AF and let $\tau_{n,j}$ denote the activation time of the n th cell in its j th activation with respect to the reference cell. Based on the modelling of the atrial electrogram in Chapter 4 and Chapter 5, the atrial electrogram model during AF can be expressed by

$$y_m(t) = Q\mathbf{r}_m^T \mathbf{D}_{\sigma,\alpha} \boldsymbol{\delta}'(t) * v'_0(t), \quad (6.1)$$

with

$$\boldsymbol{\delta}'(t) = \left[\sum_{j=1}^{J_0} \delta(t - \tau_{0,j}), \sum_{j=1}^{J_1} \delta(t - \tau_{1,j}), \dots, \sum_{j=1}^{J_{N-1}} \delta(t - \tau_{N-1,j}) \right]^T. \quad (6.2)$$

This model can then be applied to extract the tissue parameters during AF. The parameters J_n also need to be estimated in this problem. Let J_{\max} be the maximum number of activations of all cells. If we know the duration of the refractory period of the reference cell, which is denoted as T_0 , then we can obtain J_{\max} in the RR interval that has the duration of T_{RR} as $J_{\max} = T_{\text{RR}} / T_0$. Then we can put a box constraint on J_n as $0 \leq J_n \leq J_{\max}$ in the optimization problem for parameter estimation. However, if we consider the situation that v_0 is unknown and varies slowly over time, and the situation that cells can have different stereotype of action potentials, the problem gets more complicated and more work is needed to investigate. To improve the estimation, extra prior knowledge like the activation time or the fact that the conductivity of neighboring cells are relatively smaller to each other can be further incorporated as regularization terms in the optimization problem [1].

2) Heterogeneity of action potential: In Chapter 4 and 5 we used an impulse response model that requires the assumption that all cells generate the same stereotype action potential once activated, which we adopted from [1]. Although it reduces the computational cost in the problem, it neglects the heterogeneity of the action potential in cardiac tissue. Cardiac arrhythmias can obviously alter the action potential of cardiac cells. For example, the action potential duration during AF is obviously reduced compared to that during SR [2, 3]. In this dissertation, it still remains the question how much

the variability of cell action potential affects the model accuracy and the parameter estimation, which is worth studying in future work.

3) Sensitivity of model parameters: An accurate electrophysiological model of cardiac tissue always involves many parameters to represent the behaviour of a propagating action potential. In addition to the parameters to be estimated, it is necessary to understand how the other model parameters affect the accuracy of the models. Therefore, more work is needed to understand how sensitive the algorithms proposed in Chapter 4 and 5 are to the variability of these parameters.

4) Representing more detailed tissue micro-structures: Cardiac tissue consists of complex composite materials that are full of heterogeneities. In this dissertation we simplified the tissue as being two dimensional, which is more appropriate for thin-walled tissues, but less suitable when modelling the diseased atria with potential dissociation of the endo-/epicardial layer [7–11]. Multi-layer models still need to be investigated to link the electrical activities in different layers of the tissue. In addition, we assumed in the current model that the conductivity tensors are aligned along the axes to reduce the complexity of the problem. However, the curved paths of the fibre in the tissue cannot be represented well in this way. In order to investigate the role of fibrous structure in the propagation of normal and abnormal activation in cardiac tissue, parameters like fibre orientation need to be further involved in the model. Although the model accuracy can be further improved when taking into account a more detailed tissue micro-structure, it requires more parameters to present the structure that will in turn bring more difficulties in solving the inverse problems.

REFERENCES

- [1] B. Abdi, R. C. Hendriks, A.-J. van der Veen, and N. M. de Groot, *A compact matrix model for atrial electrograms for tissue conductivity estimation*, *Computers in Biology and Medicine* **107**, 284 (2019).
- [2] M. R. Courtemanche, R. J. Ramirez, and S. Nattel, *Ionic mechanisms underlying human atrial action potential properties: insights from a mathematical model*, *American Journal of Physiology-Heart and Circulatory Physiology* **275**, H301 (1998).
- [3] D. R. V. Wagoner, *Electrophysiological remodeling in human atrial fibrillation*, *Pacing and Clinical Electrophysiology* **26**, 1572 (2003).
- [4] G. Mateos, S. Segarra, A. G. Marques, and A. Ribeiro, *Connecting the dots: identifying network structure via graph signal processing*, *IEEE Signal Processing Magazine* **36**, 16 (2019).
- [5] C. Hu, X. Hua, J. Ying, P. M. Thompson, *et al.*, *Localizing sources of brain disease progression with network diffusion model*, *IEEE journal of selected topics in signal processing* **10**, 1214 (2016).
- [6] D. Ramírez, A. G. Marques, and S. Segarra, *Graph-signal reconstruction and blind deconvolution for structured inputs*, *Signal Processing*, 108180 (2021).

- [7] S. Verheule, J. Eckstein, D. Linz, *et al.*, *Role of endo-epicardial dissociation of electrical activity and transmural conduction in the development of persistent atrial fibrillation*, *Progress in Biophysics and Molecular Biology* **115**, 173 (2014).
- [8] N. M. S. de Groot, L. van der Does, A. Yaksh, *et al.*, *Direct proof of endo-epicardial asynchrony of the atrial wall during atrial fibrillation in humans*, *Circulation: Arrhythmia and Electrophysiology* **9**, e003648 (2016).
- [9] R. K. Kharbanda, P. Knops, L. J. M. E. van der Does, *et al.*, *Simultaneous endo-epicardial mapping of the human right atrium: Unraveling atrial excitation*, *Journal of the American Heart Association* **9**, e017069 (2020).
- [10] L. J. M. E. van der Does, C. Kik, A. J. Bogers, *et al.*, *Dynamics of endo-and epicardial focal fibrillation waves at the right atrium in a patient with advanced atrial remodeling*, *Canadian Journal of Cardiology* **32**, 1260 (2016).
- [11] R. K. Kharbanda, F. J. Wesselius, M. S. van Schie, *et al.*, *Endo-epicardial mapping of in vivo human sinoatrial node activity*, *JACC: Clinical Electrophysiology* (2021).

ACKNOWLEDGEMENTS

The circuits and systems group in TU Delft is a fantastic place to do research and I have had a great time. When I look back, I feel very lucky to have done the Ph.D. journey here. There are many people who I would like to acknowledge for their help and support during this journey.

First of all, I would like to express my sincere gratitude to my promotors for their valuable advice, continuous support, and patience during my Ph.d. study. I am very thankful to my promotor and daily supervisor Dr. Richard C. Hendriks. You always supported me whenever I faced the difficulties in my research. I will always be grateful to you for your guidance, patience, suggestions, and trust in my work. I am also very thankful to my promotor Prof. Alle-Jan van der Veen for giving me the freedom to choose the research direction of my Ph.D. and providing valuable suggestions in my research and to each of my presentations. Your enthusiasm and critical thinking on scientific research have deeply impressed me and inspired me to keep improving on my research skills. I would like to extend my sincere thanks to Prof. N.M.S. de Groot, thank you very much for giving me very professional suggestions from the clinical aspect and thank you for all of your suggestions and support in my Ph.D project. It was very nice and helpful to have all the discussions with you about the project at TU Delft and at the Erasmus Medical Center.

I am also very thankful to my collaborator Elvin Isufi, who gave me valuable suggestions during the first steps of my Ph.D. Thank you so much for sharing your research experience in the graph signal processing area with me and encouraging me to solve challenging problems. I would also like to thank my colleague Bahareh Abdi for sharing her experience in related work, which was helpful for me at the starting point of my Ph.D. I really enjoyed the time with you in our office. I also thank my colleague Jie Zhang who provided me a lot of help in my research journey since I was a Master student and encouraged me to continue doing research as a Ph.D. student. Thank you and your wife for your kindness for me during my living in the Netherlands. It made me feel like at home in a foreign country. There is a long list of people in this group to who I would like to express my thankfulness: Irma Zomerdijk, Mario Coutino, Tarik Kazaz, Aydin Rajabzadeh, Andreas Loukas, Jamal Amini, Jiani Liu, Hanie Moghaddasi, and the remaining members of the circuits and systems group. I will remember the good memories we have made together.

I am also very grateful to my Chinese friend Xin Ren. Thank you very much, my dear friend! It was in the PhD-startup course that we first met each other. I am so lucky to have you to be my roommate for about two years. You were always there for me, supporting me whenever needed and sharing your life experience with me. Also thank Xin An for bringing so much fun and support in my life during my Ph.D.

Finally, I want to express my thankfulness to my parents and my brother for their understanding, continuous support, and encouragement all these years. It would not

have been possible for me to achieve the Ph.D. degree without your support and love.

CURRICULUM VITÆ



Miao Sun was born in Guangdong Province, China, in 1991. She received the B.Sc. degree in Computer Science and Technology from South China Normal University, China, in 2014 and the M.Sc. degree from the School of Electronics and Computer Engineering, Peking University, Beijing, China, in 2017. She started as a Ph.D. student in the Circuits and Systems (CAS) Group at the Faculty of Electrical Engineering, Mathematics, and Computer Science in Delft University of Technology in November 2017. Her PhD research is funded by the Guangzhou Elites Scholarship Council, China. During her PhD, she

focused on developing cardiac signal processing algorithms for modelling and analyzing the electrical activity of human atria for atrial fibrillation research. Her general research interests include biomedical signal processing, mathematical modelling, graph signal processing, and machine learning.